POLITECNICO DI TORINO

Master's Degree in Energy and Nuclear Engineering

Master's Degree Thesis

DSMC analysis of a Loss-of-Coolant Accident from a He-cooled blanket in the EU DEMO Vacuum Vessel

Supervisors

Dr. Antonio FROIO

Dr. Giuseppe Francesco NALLO

Dr. Andrea ZAPPATORE

Candidate

Matteo AGATI

March 2025

Abstract

Safety is a crucial aspect to deal with when designing a nuclear reactor. Among all of the possible accidental transients considered in the section Design-Basis Accidents (DBAs) of the Probabilistic Risk Assessments (PRAs), the in-vessel Loss of Coolant Accident (LOCA) is definitely one of the most critical, because of its significant damages caused to the components inside the Vacuum Vessel (VV).

In this field, proper system-level codes already exist. Due to their intrinsic lumped nature, these tools show good performances when studying the behavior of the entire system, but they are completely incapable of predicting in advance localized quantities (e.g. if the temperature and pressure peaks are kept below prescribed thresholds) that are instead fundamental to assess the integrity of the VV in the most conservative way as possible. As a consequence, it is necessary to take into account 2D or 3D transient models.

The main objective of this thesis is to critically analyze the helium flow inside the VV following a LOCA in the helium cooled blanket of the EU DEMO by means of a 2D Direct Simulation Monte Carlo (DSMC) transient analysis of the hypersonic flow ($Ma >> 1$) developed during the accidental scenario.
Similar simulations were already performed in [1] and [2] for the Helium-Cooled Pebble Beds (HCPB) design of DEMO, while for the Water-Cooled Lithium-Lead (WCLL) it is remarkable the contribution of [3].

In the initial phase of the transient, the expanding gas is highly rarefied, meaning that the continuum assumption adopted by the above mentioned articles is not applicable at the first instants of transitory after the accident occurrence. As a consequence, conventional Computational Fluid Dynamics (CFD) codes cannot be applied in the first phases of the transient. In order to correctly simulate the physics of the problem, a kinetic model represents the best option.

The reference parameter in this field is the Knudsen number Kn, a dimensionless value defined as the ratio between the mean free path of a particle and a characteristic length of the system (in this case assumed as the distance between the inlet and the wall in front of it, $L = 3\ m$).
Because of its good performances in the evaluation of the solution of the kinetic Boltzmann equation for mediums into a wide range of values of Kn number, a successful fluid simulation tool in this field is represented by OpenFOAM (Open-source Field Operation And Manipulation) [4].

In this thesis, the transient evolution in the VV (initially at high vacuum conditions, $p_{vacuum} = 1\ mPa$) of helium entering at a pressure $p_{in} = 1\ kPa$ and at a temperature $T_{in} = 683.15\ K$ was carried out until the level of collisionalities is such that usual CFD models can be applied.

An underexpanded jet grew inside the plasma chamber during the accident.
Because of the significant computational effort into performing a DSMC analysis for the entire VV domain, the simulation was carried out until $t = 160\ \mu s$. At that time, the solution was interpolated into a smaller domain (whose height was approximately 1/3 of the original and whose inlet was shifted right after the one of the first simulation), in order to neglect those regions where the Kn number had already reached values in the continuum range.
The front evolution was monitored by means of progressive manual mesh refinements and mappings of the solution when switching from a mesh to a new one. The cell values were defined in accordance with the pressure and temperature magnitudes measured in each specific region of the domain.

It was estimated into approximately $t_{contact} = 1\ ms$ the contact between the helium entering in the VV and the wall facing the front of the jet, while the transient was carried out up to $t_{end} = 20\ ms$, time step required to approach steady-state conditions for the flow completely filling the domain of interest.

Acknowledgements

This thesis is dedicated to my parents and my little cat Noah, for the continuous support you gave me, for the constant mentoring you act on myself during this important phase of my growth and for always believing in me, sometimes even more than I did myself.

Special thanks go to Dr. A. Froio, Dr. G.F. Nallo, Dr. A. Zappatore and the PhD student M. Sprò for the extraordinary opportunity offered me to touch by hand the most advanced fields of research in the nuclear fusion simulation technologies. Up to a few years ago I did not think a day I will travel through a wonder path like Energy and Nuclear Engineering, but, as I recently wrote, I am conscious that:

"La vita è un viaggio, fatto di rallentamenti ed improvvise accelerazioni. A volte ci sorprende con cambiamenti inaspettati. In realtà siamo noi ad aver, in un istante, cambiato prospettiva, ad aver cambiato il nostro modo di vedere le cose e le cose stesse sono cambiate".

Thank you all,
Matteo

Table of Contents

List of Tables

List of Figures

Acronyms

ACB

Advanced Ceramic Breeder

AMR

Automatic Mesh Refinement

BB

Breeding Blanket

BD

Burst Disk

BoP

Balance of Plant

BWR

Boiling Water Reactor

BZ

Breeding Zone

CANDU

CANadian Deuterium Uranium

CASPER

Cluster Appliance for Scientific Parallel Execution and Rendering

CFD

Computational Fluid Dynamics

CS

Central Solenoid

D

Deuterium

DBA

Design Basis Accident

DEGB

Double-Ended Guillotine Break

DNS

Direct Numerical Simulation

DSMC

Direct Simulation Monte Carlo

ELM

Edge Localized Modes

EU DEMO

EUropean DEMOnstration

FD

Finite Differences

FV

Finite Volumes

FW

First Wall

HCPB

Helium-Cooled Pebble-Beds

HTGR

High Temperature Gas Reactor

HPC

High-Performance Computing

iDoF

internal Degree of Freedom

IHTS

Intermediate Heat Transfer System

ITER

International Thermonuclear Experimental Reactor

KIK

Karlsruhe Institute of Technology

LES

Large Eddy Simulation

LOCA

Loss-Of-Coolant Accident

LoD

Level of Detail

MD

Molecular Dynamics

MTD

Minimum Temperature Distance

MHD

Magneto Hydro Dynamics

NMM

Neutron Multiplier Material

NPC

Number of DSMC particles per cell

NS

Navier-Stokes

OB

Outboard

OpenFOAM

Open-source Field Operation And Manipulation

PCS

Power Conversion System

PDEs

Partial Differential Equations

PF

Poloidal Field

PFS

Plasma Facing Surface

PHTS

Primary Heat Transfer System

PM

Molecular weight

PRA

Probabilistic Risk Assessment

PSS

Pressure Suppression System

PWR

Pressurized Water Reactor

RAFM

Reduced Activation Ferritic/Martensitic

RANS

Reynolds-Averaged Navier-Stokes

RE

Runaway Electrons

RST

Reynolds Stress Transport

ST

Suppression Tank

T

Tritium

TCR

Tokamak Cooling Room

TF

Toroidal Field

VDE

Vertical Displacement Event

VTK

Visualization ToolKit

VV

Vacuum Vessel

WCLL

Water-Cooled Lithium-Lead

Symbols

a	Tokamak minor radius
c	Speed of light
D	Diameter
E	Energy
f	Scaling factor
h	Planck constant
k	Kinetic energy
Kn	Knudsen number
L	Characteristic length
m	Mass
Ma	Mach number
n	Number of moles
p	Pressure
q	Edge safety factor
R	Universal gas constant
r	Radius
Re	Reynolds number
T	Temperature
t	Time

V	Volume
v	Specific volume
δ	Cell size
Δt	Time step
Δx	Length interval
δ_{min}	Minimum cell size
γ	Ratio of the specific heats
λ	Molecular mean free path
μ	Dynamic viscosity
μ_t	Turbulent eddy viscosity
ω	Viscosity index
ρ	Density
σ	Particle diameter
τ	Mean collision time
υ	Average velocity
c_s	Speed of sound
c_{mean}	Mean molecular speed
f_{max}	Maximum scaling factor
$f_{suitable}$	Suitable scaling factor
k_B	Boltzmann constant
l_{char}	Characteristic grid length
m_{ref}	Molecular mass
n_{eq}	Equilibrium density
p_s	Static Pressure
p_t	Total Pressure

p_{avg}	Average pressure
T_s	Static temperature
T_t	Total temperature
Φ	Toroidal angle
θ	Poloidal angle
B_Φ	Toroidal field
B_θ	Poloidal field
R_0	Tokamak major radius

Chapter 1

Introduction

1.1 Nuclear fusion

Nuclear fusion is the nuclear reaction that powers the stars. Differently from nuclear fission (a natural reaction consisting in the splitting of heavy nuclei into smaller ones which are more stable, with the consequent release of particles and/or radiations), nuclear fusion involves two light nuclei that fuse together to produce a new atom, releasing in the meanwhile a significant amount of energy in the form of heat. The amount of energy released is measured in relativistic terms according to the Einstein's formula (1.1):

$$E = \Delta m c^2 \tag{1.1}$$

where Δm is the mass defect (the difference between the mass of the reagents and that of the products, corresponding to the amount of mass converted into energy during the reaction) and c is the speed of light.

The element cross section is strongly linked to the energy barrier that must be overcome in order to guarantee the happening of the reaction. It is recommended to deal with light atoms, since they require less energy to be fused instead of bigger atoms. With the current technology, the best choice seems to combine two isotopes of hydrogen: Deuterium (D) and Tritium (T). The first one represents 0.0156 % of all the naturally occurring hydrogen in the oceans, while the latter is present in a very small amount in the Earth, being radioactive. T undergoes the β^- reaction reported in 1.2:

$$^3_1T \rightarrow ^3_2 He + e^- + \bar{\nu_e} + 18.6\ keV \tag{1.2}$$

with an half-life of 12.3 y.
Because of the difficulty of finding a sufficient amount of T to power fusion reactors, it arises the need of producing (breeding) the fuel onsite by implementing a Breeding Blanket (BB). DEMO reactor will be the first fusion reactor adopting this kind of technology. In Figure 1.1 is reported the cross section of several fusion reactions as

a function of the input energy required for the happening of the process.
Among all of the reaction plotted, the one showing the lowest amount of input energy is the D-T reaction (1.3):

$$D + T \rightarrow^4 He + n + 17.6MeV \tag{1.3}$$

Of the total amount of energy released, approximately 1/5 (3.5 MeV) is associated to the He (that heats the plasma), while the remaining 4/5 (14.1 MeV) is carried by the neutron (that heats the blanket and activates the materials).

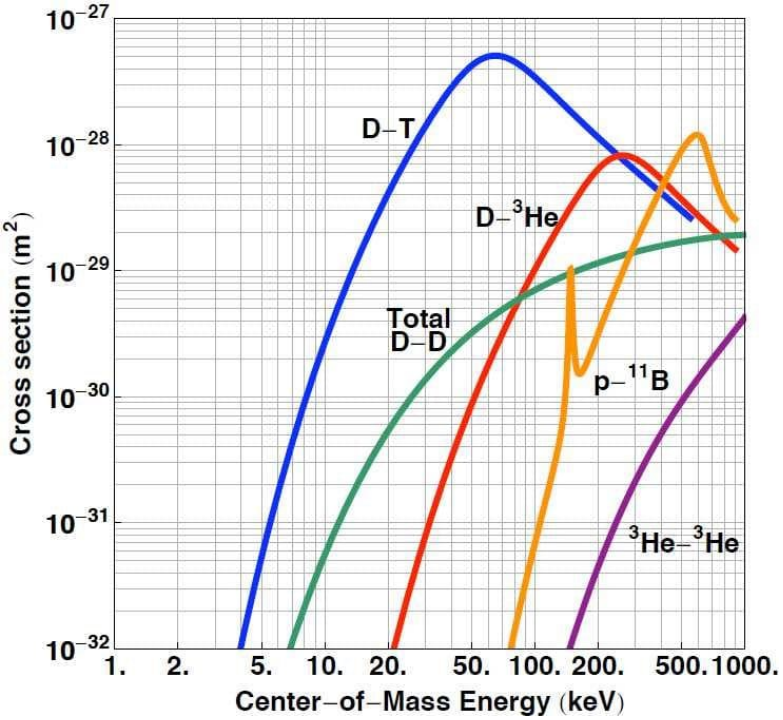

Figure 1.1: Cross section of different fusion reactions as a function of the total energy of the system, taken from [5].

When 1 g of D undergoes a fusion reaction, it releases the same amount of energy produced from $30 \cdot 10^3$ Kg of carbon [6].
Due to the fact that the reaction involves two positive nuclei, it must win the repulsion Coulomb force that tends to move away these particles. The required amount of energy can be obtained on Earth by heating the D-T mixture at very high temperatures (in the order of hundreds of millions of degrees) and in semi-vacuum conditions (in the order of μPa).
Under these extreme situations, the matter is found in the form of plasma. Because of the high temperatures necessary for the happening of fusion reactions, the

electrons are completely stripped away from the nuclei, meaning that the plasma is an ionized gas, constituted by free ions and electrons.
In general, the higher the temperature, the more energy the particles will get with a consequent higher probability of hitting each other and fusing. Moreover, the denser the fuel, the higher the probability the particles meet and experience the reaction [7].

The gain factor Q is defined as the ratio between the power produced by fusion to the power required to maintain the reaction. Obviously, if $Q < 1$, the fusion reaction would be useless, since it consumes more energy than it produces.
When the total fusion power is equal to the heating power ($Q = 1$), a particular state arises, the break-even condition. $Q >> 1$ is the only acceptable condition, because it means that the excess of energy from fusion plants can be converted to electricity and sent to the grid.
In particular, the ignition ($Q \to \infty$) represents the state such that the energy generated by fusion reactions is sufficient to heat the plasma [8]. In other words, the amount of energy produced and kept within the plasma is the same as that which leaves the plasma [9].
The energy released by fusion reactions is absorbed as heat in the walls of the vessel. Several conversion processes typical of industrial plants follows, where this heat is used to produce steam and then electricity by means of turbines and generators.

1.2 Three Challenges of fusion reactors

Nuclear fusion is definitely a multi-physics problem, involving at the same time different physical phenomena (thermal, mechanical, structural, electrical and magnetic) and different components. Critical analysis must be taken in the choices of materials and their arrangements, because some options performing singularly in a good way a given application in a specific physical field, may not be compatible with other components when the entire reactor is working.
Professor R. Zanino from "Politecnico di Torino" [10] tried to classify all the different aspects concerning the design of a fusion reactor inside three challenges. As expected, each bullet is strongly linked with the other twos.

1. **Challenge A**: Managing the power (and particle) exhaust from the plasma, while controlling impurities;

2. **Challenge B**: Extracting the power deposited in the blanket by the neutrons, while breeding the tritium fuel (and shielding);

3. **Challenge C**: Confining a 10^8 K plasma using powerful superconducting magnets, while keeping them at 4.5 K.

Moreover, the author of [10] provided a schematic classification for the different fields of research in nuclear fusion field, reported in Figure 1.2.

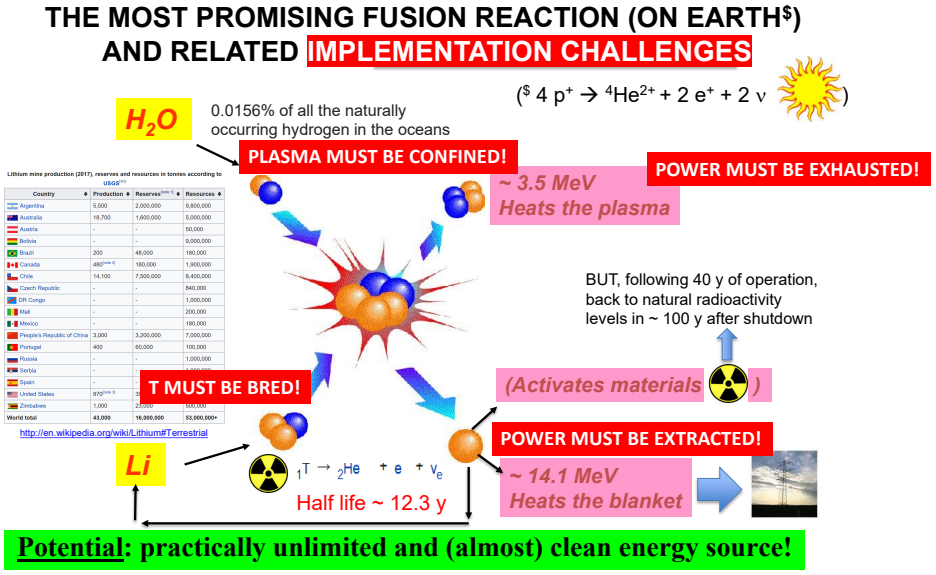

Figure 1.2: Challenges of fusion, courtesy of R. Zanino [10].

1.3 Tokamak magnetic confinement configuration

The shape of fusion reactors is a direct consequence of the need of confining a 10^8 K plasma. Among all of the different worldwide proposals, the magnetic confinement technology Tokamak represents the main stream of research in Europe. It requires the adoption of powerful superconducting magnets, while keeping them at 4.5 K. The word Tokamak comes from the Russian acronym *toroidal'naya kamera s magnitnymi katushkami* ("toroidal chamber with magnetic coils"). A Schematic view of a vertical section of this machine is reported in Figure 1.3.

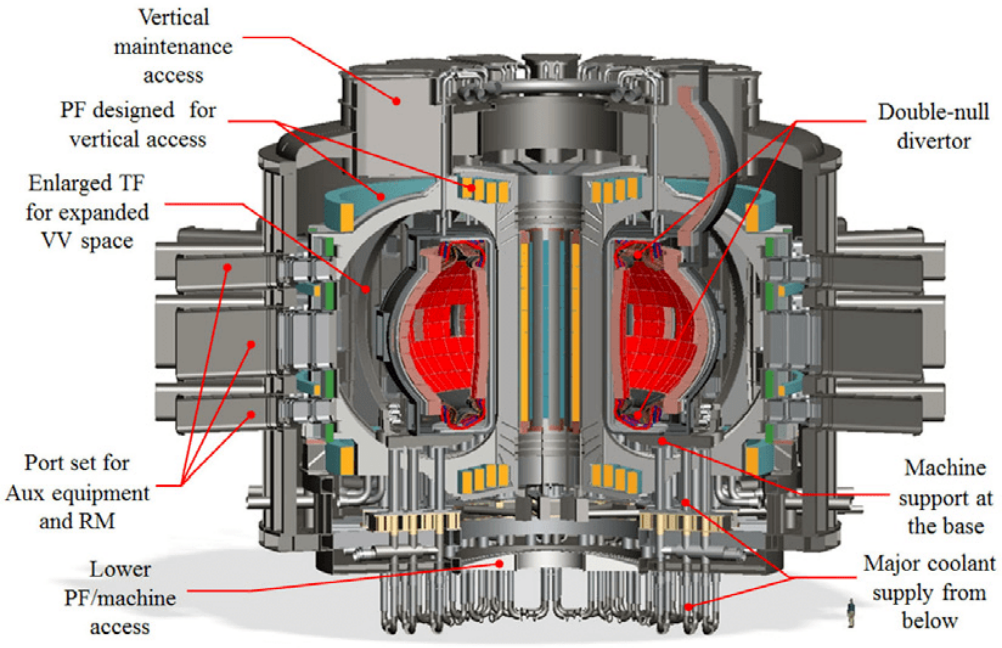

Figure 1.3: Scheme of a vertical section of a Tokamak, reproduced from [11].

The first phase of the start up concerns the evacuation from the vacuum chamber of air and impurities. Then, it follows the charging of the magnet systems and the introduction of the gaseous fuel [12].

Superconducting magnets are adopted, in order to keep the plasma as far as possible from the walls of the machine, because nowadays there is no material able to survive at the contact with the such high temperature D-T mixture.
As it can be observed in Figure 1.4, the plasma is confined by an overposition of three magnetic fields:

1. Toroidal Field (TF) produced by a set of toroidal coils spaced around the torus and directed along it;

2. Poloidal Field (PF) due to the current circulating in the plasma which is generated by the Central Solenoid (CS) and directed around the torus;

3. Despite the previous two systems are sufficient in order to confine the plasma (with a resultant helical magnetic field), a Vertical Field is adopted to provide the plasma a certain shape, fixing its position.

The manufacture of the CS (a coil located in the central hole of the torus) represents an opened engineering challenge. It should be viewed as the primary of a giant transformer, while the plasma is considered as the secondary coil.
Thanks to the driving electric current through the CS, the plasma will be forced to

flow around the torus, creating a current, which will generate another magnetic field that, in the next step, will pinch the plasma current towards the center, keeping it away from the walls.

The most important superconducting material for the CS and the TF coils is niobium tin Nb_3Sn, while the niobium titanium NbTi is used for the PF coils and the correction coils. These materials become superconducting when cooled with supercritical helium in a range of 4.5 K.

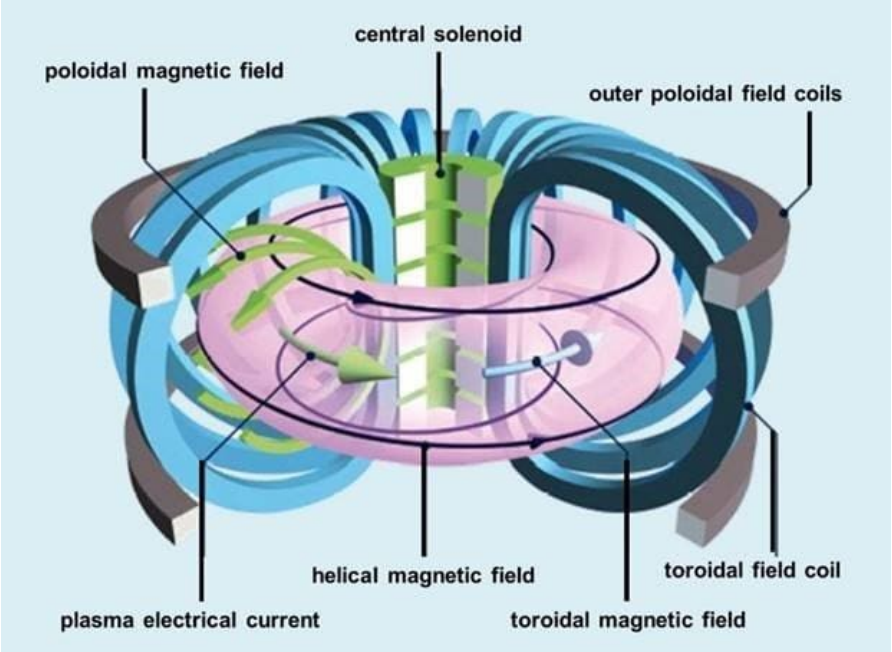

Figure 1.4: Magnetic fields proper of a Tokamak, courtesy of EUROfusion [13].

The D-T mixture is injected in the plasma chamber (Figure 1.5), where it is heated until it reaches the state of plasma, remaining confined by the magnetic fields. 80 % of the plasma chamber is occupied by the blanket-coolant and the structural materials, while the remaining 20 % is devoted to the Divertor and the plasma heating devices.

The Vacuum Vessel (VV) is a hollow steel donut where the plasma is kept isolated from the walls. Due to the fact that there is no material able to withstand temperatures in the order of 10^8 K, the magnetic fields guarantee that the plasma is hold sufficiently far from the solid surfaces that the vessel walls have to cope with "only" several hundred degrees.
Moreover, the VV satisfies the condition of high-vacuum environment for the plasma, improves the radiation shielding and plasma stability, represents the primary confinement barrier for radioactivity and supports other in-vessel components, like the Breeding Blanket (BB) and the Divertor [14].

The First Wall (FW) represents the inner side of the VV. Before ITER (International Thermonuclear Experimental Reactor), the FW was designed to be the wall of the vacuum chamber, but for the future generations of nuclear fusion reactors, the FW will be devoted to the plasma-facing wall of the BB.
The FW is made by replaceable tiles made of Carbon, Tungsten or Beryllium that, being components directly facing the plasma, they are exposed to the highest thermal load. Their most significant features are related to the high melting point, the cohesion and the absorption of other atoms [15].

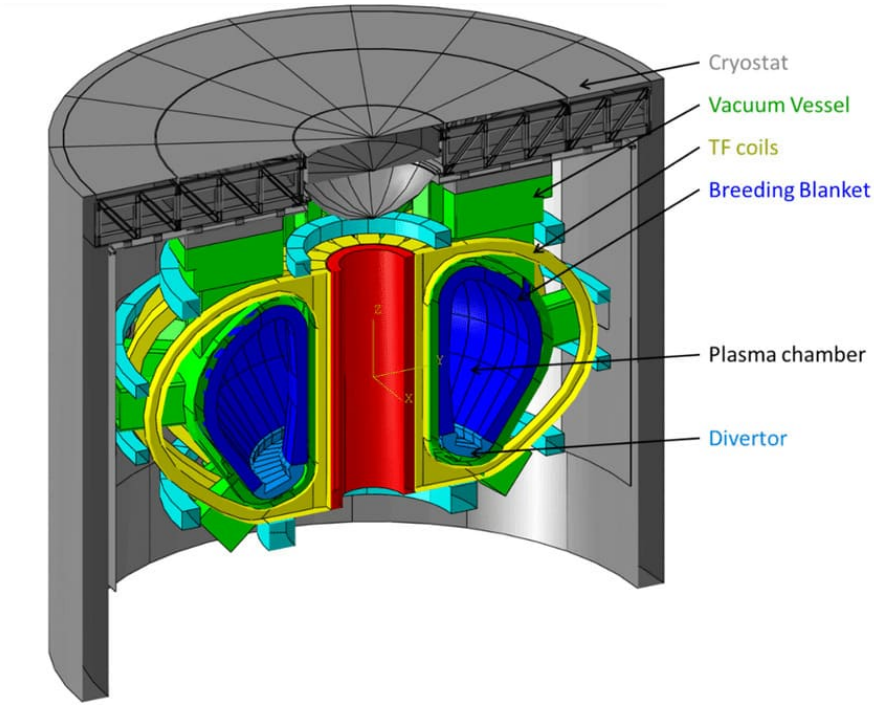

Figure 1.5: CAD of the EU DEMO tokamak, reproduced from [16].

The BB is a layer surrounding the VV in a fusion plant [17]. It is the first component looking at the plasma and it has to perform at the same time three different functions:

1. Extracting the power deposited by the neutrons produced inside the plasma (a coolant is needed, attached with a proper cooling system). The boiling from heat exchangers is used to drive a steam turbine and produce electricity [17]. The loop system is schematized in Figure 1.6;

2. Extracting the T fuel (unburned) and breeding it (from Lithium) by using the high energy neutrons obtained as a product of the D-T reaction (a breeder/ multiplier is needed);

3. Shielding by means of VV the magnets and beyond from γ-rays and neutrons coming from the plasma.

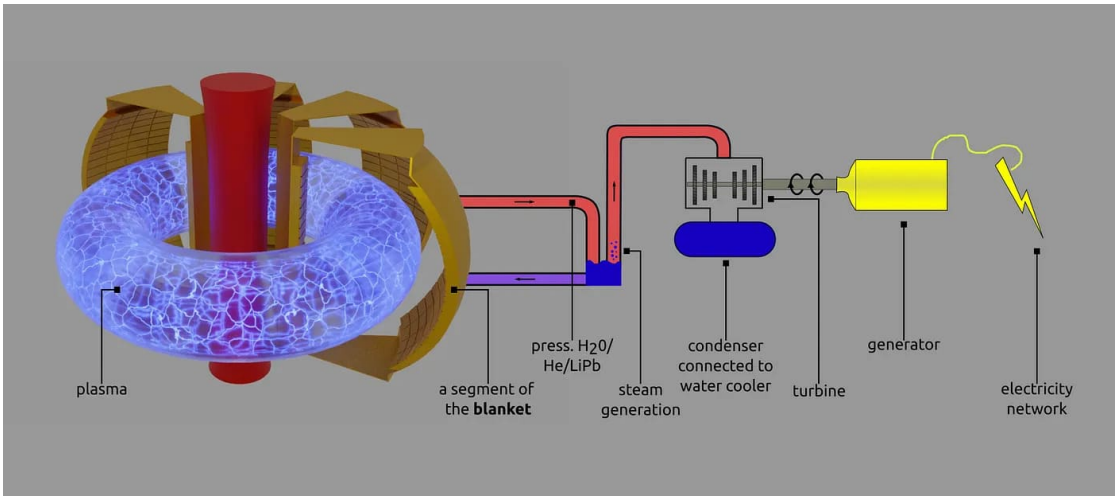

Figure 1.6: Scheme of the loop system, reproduced from [18].

Natural T occurs in negligible amount as product of cosmic rays (1.4) or as a waste of D_2O fission reactors, like CANDU (CANadian Deuterium Uranium) (1.5):

$$^{14}N + n \rightarrow ^{12}C + ^{3}T \tag{1.4}$$

$$D + n \rightarrow T \tag{1.5}$$

However, these contributions are not sufficient to support fusion reactors during all their lifetime. In DEMO will be required about 300 g of T for day to produce 800 MW of electrical power [19]. ITER, with an expected operation period around 20 y, will consume all the global inventory of T, meaning that all the successive reactors, starting with DEMO, must need a proper tritium breeding system.
The best alternative is to breed the T from Lithium (an alkali metal abundantly available in the Earth's crust). In particular, two different isotopes are taken into account, ^{6}Li (1.6) and ^{7}Li (1.7). In both cases, it is produced an α particle.

$$^{6}Li + n \rightarrow T + ^{4}He + 4.8\ MeV \tag{1.6}$$

$$^{7}Li + n \rightarrow T + ^{4}He + n - 2.466\ MeV \tag{1.7}$$

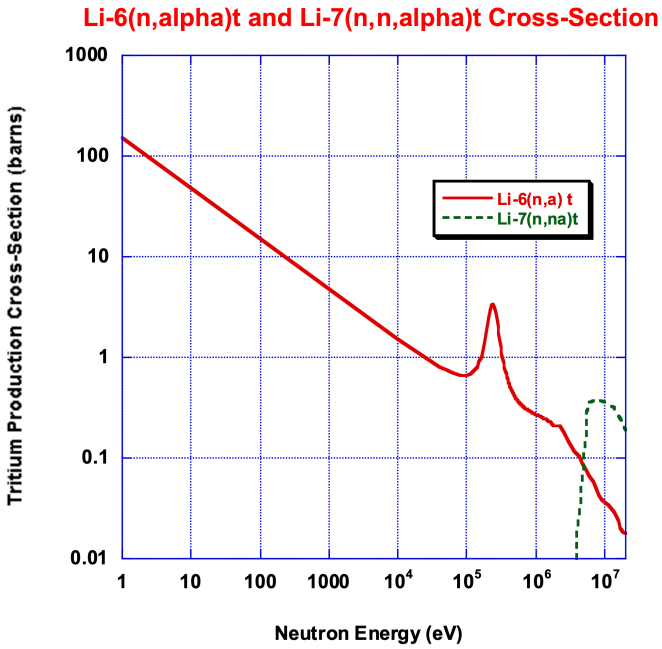

Figure 1.7: T production cross-section [barns] as a function of the neutron energy [MeV], courtesy of A. Froio [20].

Looking at Figure 1.7, ^{6}Li reaction is exothermic and shows an high cross section for low-energy regions, while ^{7}Li is endothermic and remains confined in the region of high energy neutrons. The latter has the advantage of emitting an additional neutron at lower energy that can be implemented for starting a successive reaction. In order to guarantee an electric power production from a fusion plant, the blanket thermal power must be removed at a high enough temperature that is capable of moving the selected power conversion cycle. In particular, the outlet coolant temperature of the BB should be greater than 400 ^{o}C [21].

Many designs of the BB were tested worldwide. For DEMO reactor, two different proposals are currently studied: the Helium-Cooled Pebble Bed (HCPB) and the Water-Cooled Lithium-Lead (WCLL). This thesis is focused on the HCPB configuration, which implies helium as a coolant.

The VV is an hermetically sealed steel container, which works as a first safety barrier for the plasma inside it, belonging in the condition of high-vacuum. Taking into account Figure 1.5, it is evident that the VV contains both the BB and the plasma chamber and it is encapsulated inside the Cryostat, a high volume stainless steel pressure chamber. It provides at the same time high vacuum and the extreme cooling required by the superconducting magnets and the VV [3].

1.4 The HCPB Breeding Blanket

Originally proposed by the German Karlsruhe Institute of Technology (KIK) since 1980s, the HCPB blanket concept uses pressurized helium gas (at 8 MPa) as coolant, Li ceramic as T-breeder and Be composites as Neutron Multiplier material (NMM), the Reduced Activation Ferritic/Martensitic (RAFM) Steel EUROFER-97 as structural material and the W as armor of the FW [22].
In Figure 1.8 is reported a schematic design of the HCPB breeding (1.6) and multiplying functions for DEMO reactor.

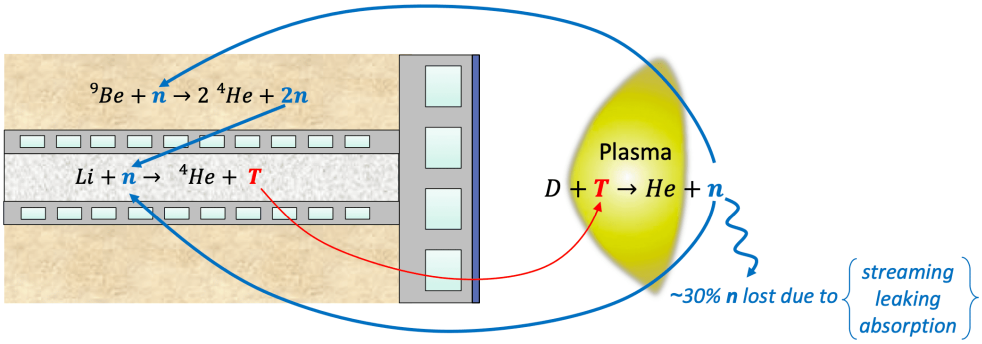

Figure 1.8: HCPB breeding and the multiplying, courtesy of EUROfusion [23].

The main features of this technology can be summarized as follows:

- ^6Li reaction (1.6) is chosen because of the high Li density (implying compactness and low ^6Li enrichment) and the need of avoiding Magneto Hydro Dynamics (MHD), reactivity and corrosion. Moreover, it guarantees a significant separation of T from purge gas and an easier T extraction from the breeder;

- The Be or its alloys are used at the same time as NMM (1.8) and moderator, guaranteeing, in the meanwhile, the best T breeding in compact space:

$$^9Be + n \rightarrow 2^4He + 2n \tag{1.8}$$

- As structural material is adopted the EUROFER-97 that represents a good compromise in terms of thermal and mechanical properties (with a temperature window estimated in the range $350 - 550\ ^oC$). It belongs to the RAFM steel family. It shows a very much reduced irradiation inducing swelling and susceptibility to the production of He under neutron bombardment and it can be treated with chemical compositions in order to achieve reduced activation and waste. However, it undergoes embrittlement due to $Pb_{16}Li$ for temperatures above $450\ ^oC$;

- After many years of experience from High Temperature Gas Reactors (HTGR), the helium gas is here devoted to heat extraction. Being neutronically transparent, it avoids issues related to material activation. It is a 1-phase fluid and it is chemically inert. Moreover, it shows an high range of compatibility with EUROFER-97 and it can also be implemented as functional material.

For fusion reactors, the choice of using solid breeders in pebble bed forms (look at Figure 1.9) is due to both technical issues (relaxation of thermal stresses and enhancement of T removal) safety & reliability purposes (high melting point, high thermal conductivity, good mechanical properties, low activation and low reactivity). The gas atmosphere has a strong influence on the pebble bed effective conductivity. Packing is recommended because the thermal conductivity increases with temperature and compression strain [20].

[M. H. H. Kolb, 2014]

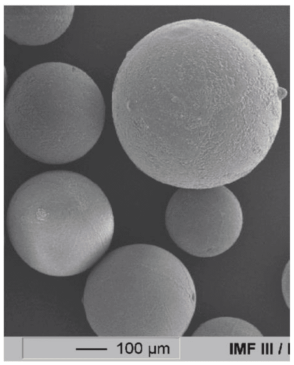

Li_4SiO_4

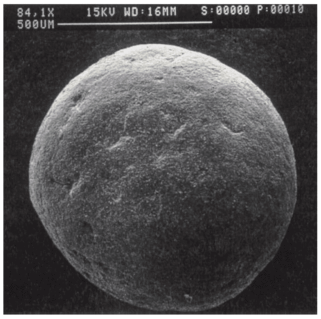

Li_2TiO_3

Figure 1.9: Examples of *Li*-composite pebble beds, courtesy of A. Froio [20].

The blanket box (look at Figure 1.10) is made by structures continuously cooled by external plates or tubes for heat extraction in solid materials. The low pressure gas flow favors the T extraction from the breeder. The T permeation from the breeding beds to the coolant is due to the large thin walls between two chambers.

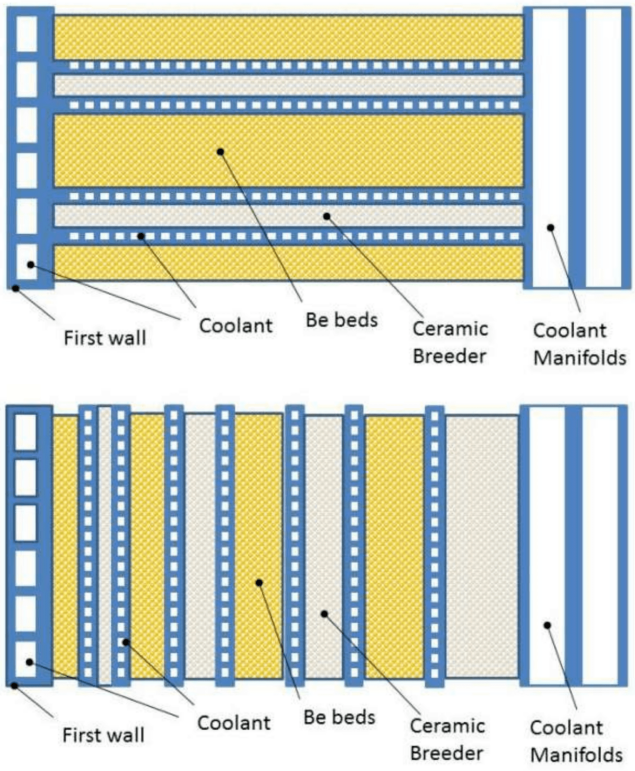

Figure 1.10: Mechanism of T permeation in the pebble bed breeder form, courtesy of A. Froio [20].

The BB interfaces are a crucial aspect to deal with when designing the Balance of Plant. This region of the reactor includes the Primary Heat Transfer System (PHTS), the Intermediate Heat Transfer System (IHTS) and the Power Conversion System (PCS).
The first BB architecture (schematized in Figure 1.11) for EU DEMO will opt for keeping the breeder and the coolant in two separate circuits with separate functions:

1. The *coolant loop* removes the heat flowing from the PHTS to the PCS;
2. By using a T carrier, the *breeder loop* pushes the T outside the VV, where it arrives in molecular form, being ready to be delivered to the Fuel Cycle.

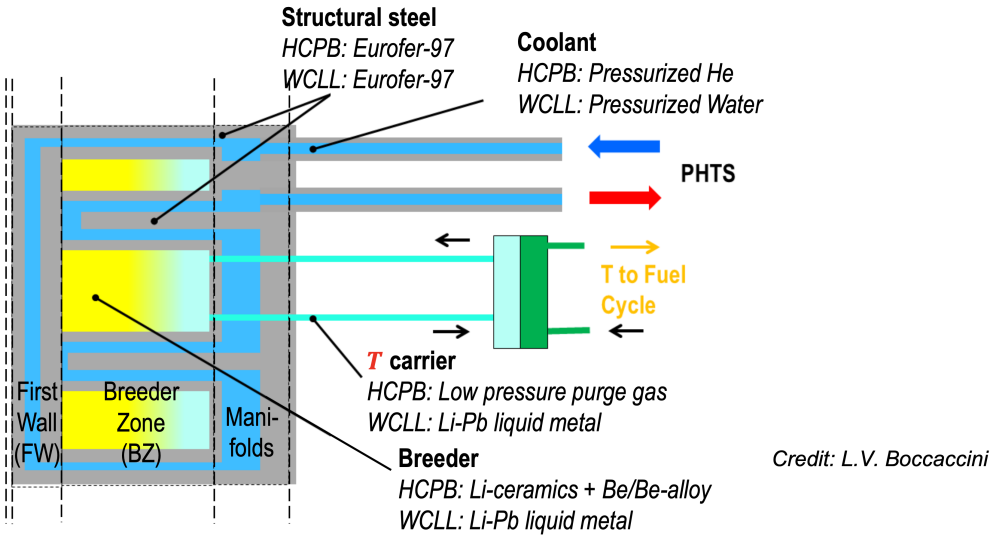

Figure 1.11: Schematic representation of the separated Breeding/Cooling functions, courtesy of EUROfusion [23].

In the HCPB thermal-hydraulic design of DEMO, the FW and the Breeding Zone (BZ) are placed in series. The BZ operational parameters ($8\ MPa,\ 300 - 520\ ^oC$) guarantee a better temperature control, while the heat transfer promoters in the FW regions are able to deal with heat fluxes (HF) up to 1.4 MW/m^2. Heat transfer augmentation structures are needed in both the FW and the fuel pins.
In Figure 1.12, Figure 1.13 and Figure 1.14 are reported different prospective views of the HCPB BB design of DEMO. As it can be observed, the T breeder material is put inside fuel-breeder pins. These components are then placed inside prismatic blocks of neutron multiplier with hexagonal shape.
There are two concentric tubes forming the cladding of the Advanced Ceramic Breeder (ACB) pebbles in Figure 1.12. From one side, the two tubes are linked by a reversed tunnel, filled by the ACB pebbles. The coolant first flows through the inner cladding tube, moving through the reversed tunnel and turning back into the annular channel (counter-current flow). The concentric tubes are externally surrounded by a larger concentric pressure tube, offering an annular cooling channel together with the cladding [22].
The heat transfer between the prismatic box and the fuel breeder pin is limited through the presence of a helium gas gap, adopting a similar technology to the one already seen between the fuel pellets and the cladding of fission power plants.

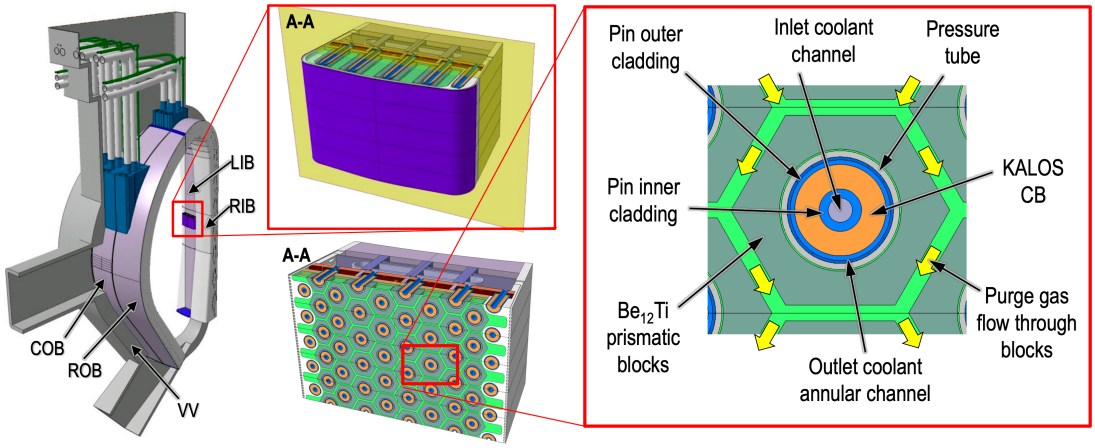

Figure 1.12: Schematic representation of the HCPB "fuel breeder pin" design ($BL2017$) - Section orthogonal to the fuel pins, courtesy of EUROfusion [23].

From CFD studies, it was determined that the most critical parameters in the flow stabilization are represented by the distance between the nozzle exit and the solid surface in the tunnel region. For achieving an homogeneous flow, one end of the fuel-breeder pin was reduced to a ballpoint pen (Figure 1.13).

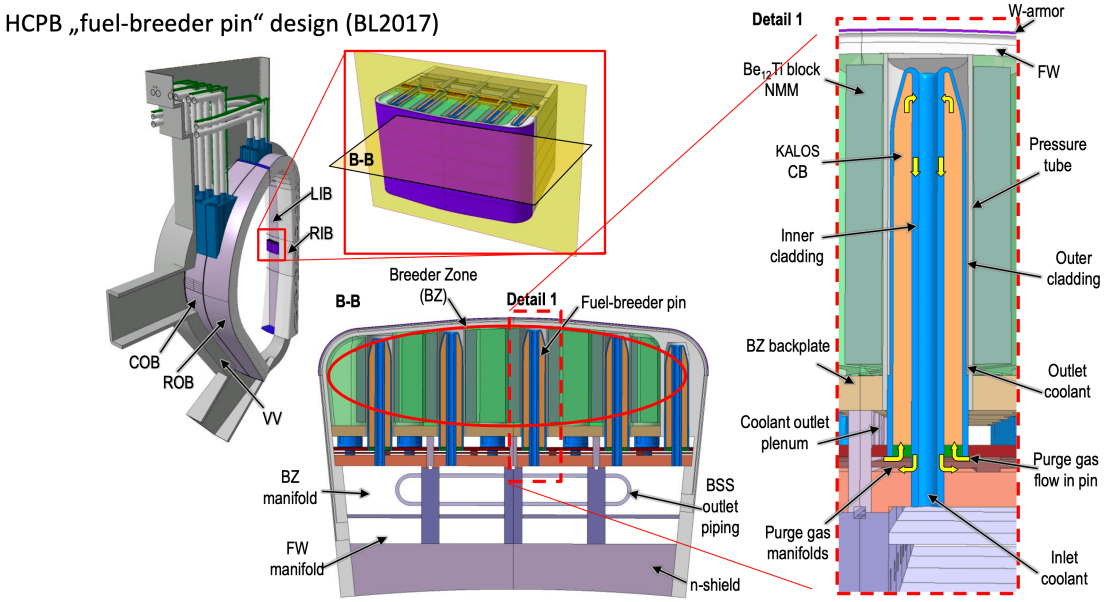

Figure 1.13: Schematic representation of the HCPB "fuel breeder pin" design ($BL2017$) - Section parallel to the fuel pins, courtesy of EUROfusion [23].

The coolant feeding and purge gas pipes are connected to the segment chimneys and routed in and out through the Upper Port of the VV, where the blanket segments are attached by properly designed structures (Figure 1.14).
With a thickness of 20 mm of U-shaped and actively cooled plates, the FW is coated with 2 mm thick of W and EUROFER-97, to contrast the erosion by fast particles coming from the plasma.

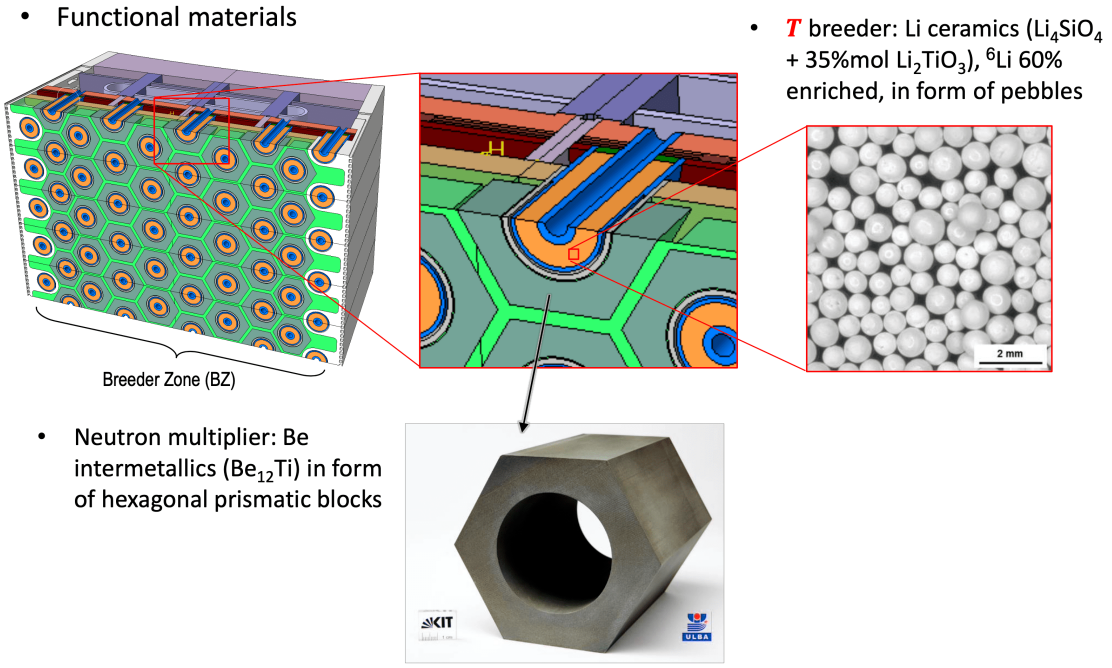

Figure 1.14: Schematic representation of the HCPB "fuel breeder pin" design ($BL2017$) - Zoom of the section orthogonal to the fuel pins, courtesy of EUROfusion [23].

In the end, the most important challenges related to the HCPB design belong into the neutron shielding, thermal control and thermo-mechanics of functional materials, production costs, pressure drops and the complex system of the PHTS layout and piping [23].

1.5 EU DEMO

Presented in 1995 by EUROfusion as the natural successor of ITER, DEMO (DEMOnstration Power Plant) will be the last research fusion reactor to start operation around 2050, before the capillary diffusion of the new commercial cheaper reactors in the second half of XXI century [24].

Differently from ITER, DEMO (artistically represented in Figure 1.15) will demonstrate the capability of keeping the stability of plasma for an unlimited time, in order to guarantee the possibility of generating electric power output from fusion reactions. Being the power density of nuclear fusion smaller than the fission and fossil competitors, the adoption of expensive and bigger structures will be necessary.

In the conceptual design of DEMO, the large radius of the plasma cross-section ranges from 6 m to 10 m, while the one of ITER is of 6.2 m and the one of JET is approximately one half of that.
In ITER, the high energy neutrons obtained from fusion reactions produce heat by hitting the VV wall. In future reactors, this phenomenon will be used for two main energy production purposes: preparation of nuclear fuel for conventional fission reactors (by interaction with heavy elements, like Thorium or depleted Uranium) or to "break down" nuclear waste [25].

DEMO will contribute into the grid with 500 MW_e. The initial goal, fixed at 2000 MW_{TH} from fusion power, will be increased up to 2400 MW_{TH} of thermal power (taking into account the neutron multiplication in the BB and the plasma heating). In the end, will be delivered 900 MW_e of electrical power, of which 400 MW_e will be put again in the system in order to keep it working [26].

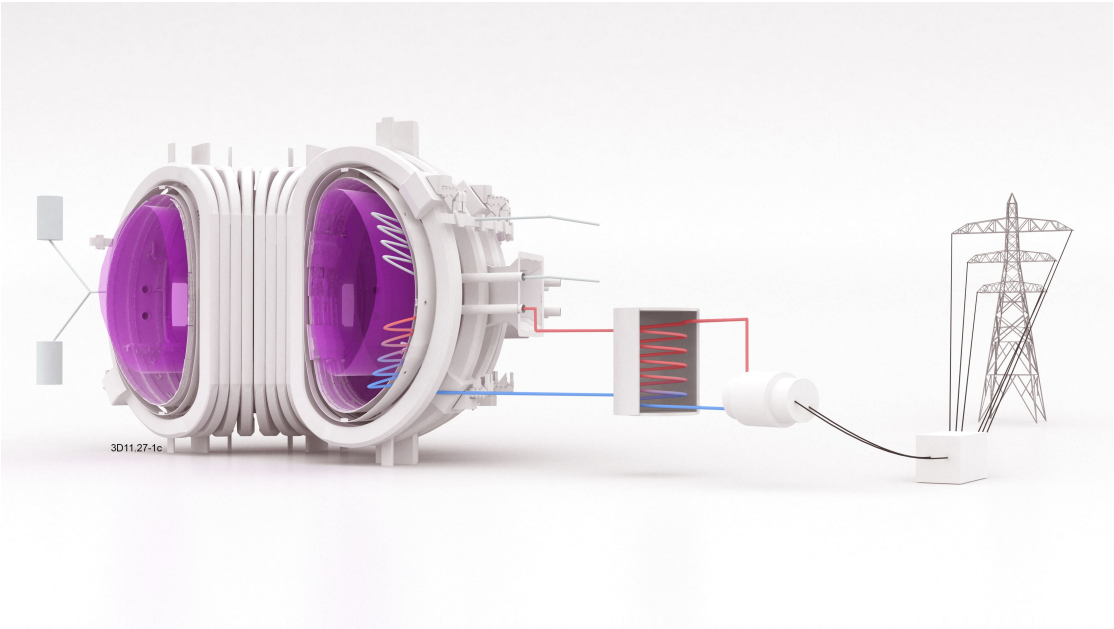

Figure 1.15: Artist's concept of DEMO connected to the power grid, reproduced from [27]

In Table 1.1 is reported a numerical comparison between the main research European Tokamaks already completed or under development. It is clearly visible that EU-DEMO will have the most advanced features. Despite the nominal steam turbine value is 790 MW_{TH}, a 5% reduction has to be taken into account because of the coupling from the turbine to the synchronous generator. This phenomenon diminishes the nominal value for the electrical power output to around 750 MW_e.

PARAMETER	**JET (1997)**	**JET (2021)**	**ITER**	**EU-DEMO**
Plasma radius	2.96 m	2.96 m	6.2 m	9 m
Plasma volume	83 m^3	79 m^3	840 m^3	2519 m^3
$\boldsymbol{\Delta t_{max}}$ **plasma**	30 s	30 s	1000 s	2 h
Magnetic field	3.45 T	3.45 T	5.3 T	5.9 T
Fusion power	16 MW_{TH}	10-15 MW_{TH}	500 MW_{TH}	2000 MW_{TH}
$\boldsymbol{Q_{ext}}$ **plasma**	24 MW_{TH}	40 MW_{TH}	50 MW_{TH}	50 MW_{TH}
Gain Factor	0.65	0.25	10	40
$\boldsymbol{E_{production}}$	No	No	No	Yes
First plasma	1983	–	Dec 2025	~2055
First T plasma	1991	–	Dec 2035	~2055

Table 1.1: Features of the main European Tokamaks, reproduced from [26].

Among all the challenges for DEMO, the following ones will be devoted to the foundation of a robust conceptual design:

- Solution of technical issues related to fueling, exhausting, confining, extracting and separating of T will be fixed;

- Additional appropriate systems respect to the actual ones in order to capture and convert fusion power in electricity will be needed [28];

- Strong reduction of the plasma pulse duration and the consequent mix of plasma heating systems (the lifetime of materials and the stability of plasma will be much greater in DEMO respect to ITER);
- Allowable remote maintenance by means of manipulators;
- Nuclear safety systems intrinsic of the reactor design from the very early phases [29];
- The reliability of plasma control has to be stronger in DEMO respect to ITER and this can be possible by adopting additional sets of diagnostics and actuators [30].

Safety is a crucial aspect in nuclear reactors since the pre-conceptual phases. Among all the possible Design Basis Accidents (DBAs), the analysis of the Loss-Of-Coolant Accident (LOCA) is the one carried out in this thesis.

1.6 Classification of LOCAs in fusion reactors

The consequences of a LOCA event into a fusion reactor are strongly correlated to the location where this accident happens, because different positions lead to different scenarios. In any case, a LOCA occurs when one of the pipes breaks, causing a significant release of the coolant into the external environment. As a first attempt, it is needed to distinguish between the two main components taking part in the accident: the Breeding Blanket and the Superconducting Magnets:

- Breeding Blanket:
  (a) **In-box LOCA**
  Due to the presence of high energy neutron irradiation, high thermal load and great pressure gradient, it is higly probable that the rupture of the pipe occurs in the breeding zone of the BB [31].
  (b) **In-vessel LOCA**
  In this case, the accident is originated on the plasma-facing surface of the BB because of an unprotected plasma transient event that causes the breakage of a portion of the FW, leading to the large release of pressurized coolant inside the plasma chamber [32].
  (c) **Ex-vessel LOCA**
  This kind of accident is the most studied one, since it evolves in similar way to a typical fission Pressurized Water Reactor (PWR). For example, in [33] it is assumed that this accident appears like a Double-Ended Guillotine Break (DEGB) of the main pipe in an outboard (OB) loop of

the PHTS, leading to the helium blow down into the Tokamak Cooling Room (TCR).

- Superconducting Magnets:

  (a) **In-cryostat LOCA**
  This topology of accident is due to the release of helium coolant from one of the magnets into the cryostat, with consequent permanent damage of the superconducting magnets [3].

In this thesis, it is analyzed an in-vessel LOCA (also indicated as in-VV LOCA), starting from the time zero of the accident occurrence and by adopting an hybrid CFD-DSMC method for the HCPB design of DEMO reactor.

1.6.1 Characterization of the in-VV LOCA

When an in-VV LOCA occurs in the HCPB design, the high-pressure helium gas flows into the VV. It causes a highly underexpanded jet that hits the radioactive dusts located in the bottom of the VV, leading to their subsequent resuspension and migration. The reactor operation is compromised and the release of radioactive materials may occur [34].

At the time when the helium starts flowing inside the VV, a Mach disk structure is formed near the break. The rapid pressure increase inside can approach the limit of the VV Pressure Suppression System (VVPSS). In order to avoid the rupture of the VV, the VVPSS has the aim of removing the coolant from the VV, preserving its integrity and safety by storing the coolant and the radioactive products inside it [35].
According to the simulation performed on [34], as the in-VV LOCA proceeds, the Mach disks move toward the equatorial break of the VV, with a shape continuing to shrink and the number of structures gradually increase.

Differently from fission reactors, where the failure criterion depends on a global parameter, in fusion reactors the VV failure is strongly influenced by the pressure on a specific surface. It means that system level codes, like RELAP [36, 37], GETTHEM [35, 38] or MELCOR [36, 39], being lumped model, provide a poor description of the accidental scenario (e.g., they cannot estimate the localized quantities, essential in order to determine the cause of failure) [3].

1.6.2 Physical description of underexpanded jets

Due to the large diffusion of hydrogen as energy carrier, the high-pressure hydrogen process and storage systems will be develop by side. An underexpanded jet is usually a consequence of its accidental release [40]. It is a phenomenon that occurs

when a fluid is discharged from a device at a pressure greater than the ambient one. This situation is the one typical of convergent and convergent/divergent nozzles. The evolution of the jet is linked to the pressure ratio (1.9) [41] :

$$\eta = \frac{p_{crit}}{p_{amb}} \tag{1.9}$$

Where p_{crit} represents the critical jet exit pressure p_e. The underexpanded jet is considered to start at $\eta > 1.9$ for the hydrogen. The level of underexpansion can be estimated from 1.9, allowing the definition of three different regimes [41]:

1. moderately underexpanded jets, for $\eta <\sim 3$
2. highly underexpanded jets, for $2 < \eta < 4$
3. very highly underexpanded jets, for $\eta > 4$

From a physical viewpoint, it is possible to classify two different situations: weakly (or regular) underexpanded jet from one side and strongly (or irregular) underexpanded jet from the other one [42]:

1. **Regular underexpanded jet**
   At the exit section, Prandtl-Meyer isoentropic expansion mechanism cause the flow close to the center to move forward, while the one in the range of nozzle edge turns outward [3]. The process is detailed in Figure 1.16. The Prandtl-Meyer expansion waves reflect from the constant pressure boundary, switching to compression waves that, then, coalesce giving rise to interception shock. The latter reflects at the centerline producing reflected shock [42].

2. **Irregular underexpanded jet**
   In this case, along the centerline the pressure decreases because of the expansion waves and somewhere may happen that $p_e < p_{amb}$. The reflected waves give origins to a compression fan, merging into an oblique shock [43]. An adverse pressure gradient is required to move p_e to p_{amb}. For highly underexpanded jets, the reflection of the oblique shock wave is a consequence of the intersection at the triple point with a normal shock, indicating as Mach disk [44]. This structure is generated wherever the pressure gradient is large over a certain distance.

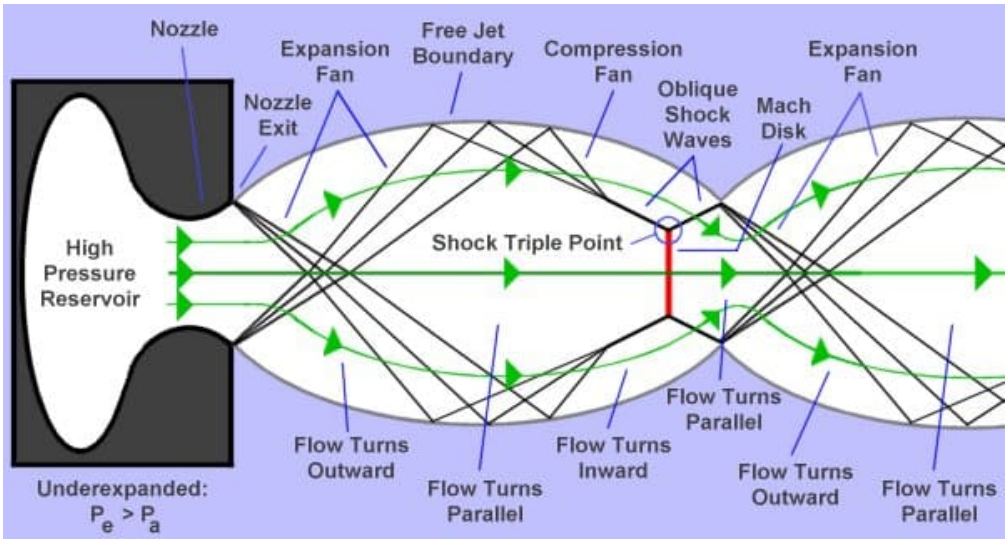

Figure 1.16: Prandtl-Meyer underexpanded jet process, reproduced from [45]

The barrel shaped expansion region of jets ends with a normal shock wave and a Mach disk. This last physical phenomenon develps at the boundary of supersonic and subsonic flow, indicating the point where the jet pressure returns to the ambient one. For highly underexpanded jets, both the barrel shock and the Mach disk structure can be repeated several times moving downstream from the nozzle [40]. It possible to distinguish three zones inside the jet:

1. **Nearfield zone**
   It can be split into the core region and the mixing layer region. In the first one, the compressible effects are predominant and the flow is isolated from the ambient fluid; in the latter, it is remarkable the switching between the ejected fluid and the surrounding one because of turbulence effects [41].

2. **Transition zone**
   It is characterized by negligible changes in the flow variables. This phenomenon guarantees the development of a more uniform pressure field due to the mixing of the ejected and the ambient fluids [41].

3. **Farfield zone**
   In this region, at perfect jet expansion, can be seen the development of the flow having similar values of thermal-hydraulics parameters (mean pressure, velocity and temperature). Despite the high velocity (decaying farther downstream), the jet is in pressure equilibrium with the ambient fluid [41].

The large-scale eddies are contained in large amount in the mixing layer region. Interacting with the various shock waves, they influence the spreading rate and the

associated decay of a jet. Flow instabilities are mostly due to viscous effects, with strong consequences in the width of the mixing layer and on the diameter of the jet [41].

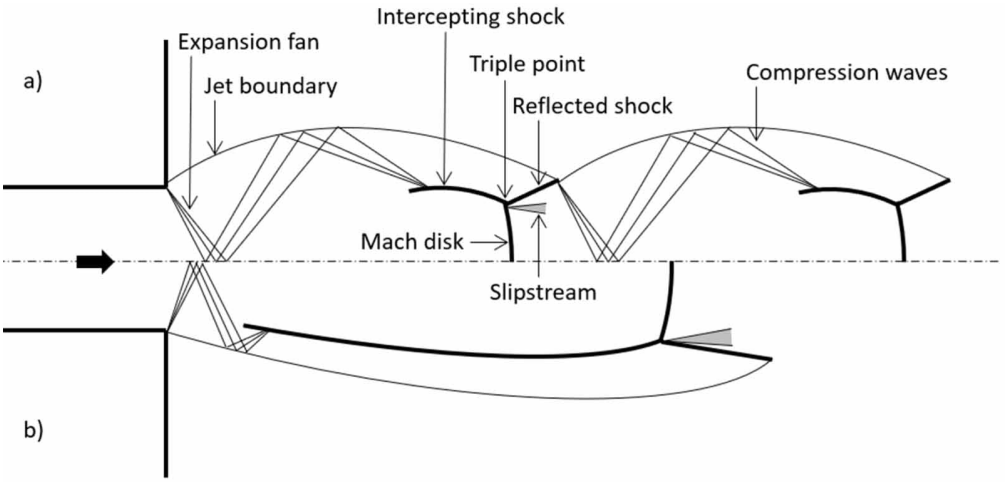

Figure 1.17: Structure of a moderately (a) and very highly (b) underexpanded jet, courtesy of [1]

The highly underexpanded jets are characterized by a singular reflection. Moving from a regular reflection to a singular one, it is possible to notice the presence of a Mach disk. The preparation of a flow for entraining a subsonic regime is attached to the detachment of the shock waves [41].
As it can be observed from Figure 1.17, for very highly underexpanded jets ($\eta >> 4$), the Mach disk becomes curved because of the presence of only one shock cell.
Both the Prandtl-Meyer angle (dependent on the ambient Mach number and the exit Mach number and, therefore, on the pressure ratio) and the nozzle angle affect the angle taken by the jet [41].

1.6.3 Modeling approach for the LOCA transient

The LOCA transient must be modeled starting from the instant where the break occurs. As the fluid starts exiting from the pipe, the first shock (*Leading shock* or *Leading edge*) cause the formation of a planar front [3].
The oblique shock intercepts a second shock coming from the leading edge (gradually dissipating because of the prosecution of expansion in a quiescent medium). The shock propagation may cause the development of a Mach disk that becomes stronger because of the accumulation on it of compression waves consequent to the expansion. The jet evolution is limited by the facing wall, whose energy content is reduced due to the increase in the average pressure inside the VV (and the reduction of the

pressure ratio η) [3].

The computational approach for transition and scattering regimes for a highly underexpanded jet outflow is represented by the DSMC method (based on the kinetic gas models) and, from a certain point on, by the NS equations. There is an high degree of accuracy when dealing with empirical expressions of the characteristic dimensions of the shock wave structure in the transition regime. When the flow regime is hydrodynamic, both the DSMC method and the NS equations provide comparable results in the nozzle region [46].

In the mixing region, the Kn number proper of flow regime shows a transitional behavior. In some positions, the jet flow calculations become a critical issue because of the non-equilibrium effects. It is needed to switch from the traditional NS equations to the DSMC method.

One issue is certainly due to the simulation of a dense flow in the nozzle. Bigger computational domains are required both in the axial and radial directions of a jet expansion region for $\eta >> 1$ [40].

Luckily enough, the use of powerful supercomputers allows the implementation of hybrid approaches, able to combine the solution of the NS equations for a hydrodynamic region with the kinetic approach for a rarefied region [40].

Chapter 2

DSMC method

2.1 Gas flow description levels

A gas flow can be analyzed at two different levels: the macroscopic and the microscopic ones. The macroscopic model looks at a gas like a continuous medium and can be mathematically approached by Navier-Stokes (NS) equations. This set of Partial Differential Equations (PDEs) provides a description in terms of the spatial and temporal variations (independent variables) of the classical flow properties (dependent variables, e.g. velocity, density, pressure and temperature) [47].

The microscopic (molecular) model deals with a discrete representation of a gas flow and, in principle, it should be able to give information about the position, velocity and state of each molecule at all times. In this case, the reference model is represented by the Boltzmann equation. This formulation cannot show an analytical counterpart for non-trivial problems, with a consequent increasing difficulty when it is approached by the common numerical methods. Nevertheless, the particulate structure of the gas at molecular level allows a direct implementation of the physics of the problem, instead of dealing with such complicated mathematical tools. The noticeable advantage of this model is the substantial absence of numerical instabilities, while its significant drawback is related to the increasing order of computing resources.

2.1.1 Microscopic description requirements

The NS equations, typical of a continuous gas dynamics, break when the gradients of macroscopic variables become so steep that their scale length seems to be comparable with the average distance travelled by the molecules between collisions, the well-known *mean free path* [47].

In the NS formulation, the shear stresses, heat fluxes and diffusion velocities are linear functions of the gradients in velocity, temperature and species concentration.

The dimensionless parameter proper of this field, able to measure the degree of rarefaction of a gas, is represented by the Knudsen number (Kn), defined as the ratio of the mean free path λ to the characteristic dimension L (2.1):

$$Kn = \lambda / L \tag{2.1}$$

The NS equations provide good results for $Kn < 0.1$, while they do not show right performances in the transition region (for $0.1 < Kn < 0.2$). Then, from $Kn > 0.2$, the microscopic model can be correctly applied. The switching of NS equations to Euler equations happens for $Kn \sim 0$, where transport terms can be neglected (Figure 2.1).

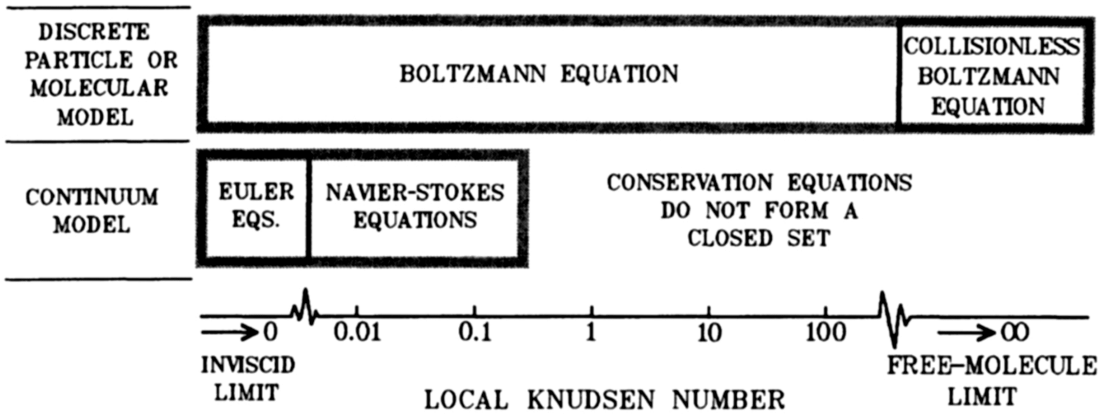

Figure 2.1: The Knudsen limits on the mathematical models, reproduced from [47].

The independence of the Kn number from the density (when dealing with the waves) establishes the validity of the NS equations only in terms of shock Ma number, which has to be smaller than two. For low densities, Kn number increases significantly. In this situation, typical of shock waves and/or boundary layers, as the flow becomes rarefied, the amount of viscous flow increases.
When the pressure tensor reaches a sufficient anisotropicity, the continuum model leaves place to the molecular model, indicated by Bird [47] in terms of *breakdown parameter* (2.2):

$$P = \frac{1}{\nu} \left| \frac{\mathrm{D}}{\mathrm{D}t} (ln\rho) \right| \tag{2.2}$$

The internal structure of shock waves needs to take into account the molecular model at all densities. The presence of the forces acting on a very small particle suspended (or moving through the atmosphere) or the propagation of sound at extremely high frequencies require the adoption of a molecular approach [47].

2.1.2 The simple dilute gas theory

According to this theory, the *simple gas* is constituted by molecules having the same structure and coming from a single chemical species.
Avogadro's law states that the volume occupied by one mole of any gas at a particular temperature and pressure is the same for all gases [47]. It is possible to demonstrate that the mean molecular spacing δ is linked to the *number density* n by 2.3:

$$\delta = n^{-1/3} \tag{2.3}$$

This expression shows that as the density decreases, the molecular spacing δ becomes larger, when compared with the effective molecular diameter d.

If two molecules can be seen as two hard elastic spheres of diameter d, the collision occurs when their trajectories are such that the distance between their centres decreases to d. As a consequence, the *total collision cross-section* can be estimated according to 2.4:

$$\sigma_T = \pi d^2 \tag{2.4}$$

However, the molecular size is not so easy to define, meaning that it is necessary to qualify the results from the elementary kinetic theory, based on the molecular "diameter" [47].
Moreover, the collision cross-section typical of realistic models depends on the relative speed between the molecules.
When only a small portion of space is occupied by molecules and the mutual influence can be neglected, it is possible to talk about *binary collisions*. This particular condition provides a definition of *dilute gas* (2.5):

$$\delta >> d \tag{2.5}$$

At these space scales, the statistical fluctuations seems to have a such low influence that there are no gradients in the macroscopic properties with either distance or time [47].

The time occurring between two successive collisions is called *mean collision time* and it is used to define the time-scale of the macroscopic process. The inverse of this value is the well known *collision rate* (or *collision frequency*) ν per molecule. The *isentropic flow* at the macroscopic (or continuum) level has a microscopic counterpart represented by *local thermodynamic equilibrium*.

2.1.3 Macroscopic properties in a simple gas

The necessary condition to define a macroscopic quantity (2.6) is a result of the averaging over the molecules in a small element of volume (considering as a characteristic dimension $V^{1/3}$):

$$V^{1/3} >> \delta \tag{2.6}$$

Normally, the macroscopic properties based on the molecules in the element will depend on the size of the element. For a 3D flow with gradients in all directions (and with scale length L), the requirement is $V^{1/3} << L$.
A good practice is to apply a proper *time average* that allows to describe any steady flow in terms of macroscopic properties. It is obtained by summing the characteristic properties of the molecules in the volume element over an extended time interval.
On the other hand, the *ensemble average* is a result of an instantaneous averaging taken over the molecules in corresponding volume elements in an indefinitely large number of similar systems [47].
When both descriptions provide the same outputs, the molecular motion is *ergodic*.

2.1.4 Collisions in gas mixtures

A gas mixture can be assumed to be formed by a total of s separate chemical species. Considering the collision between two of them, one of type p and another one of type q (with correspondent effective diameters d_p and d_q), the collision occurs when the distance between their centres decreases to $(d_p + d_q)/2$.
Therefore, the total collision cross-section is defined according to 2.7:

$$\sigma_{T_{pq}} = \pi(d_p + d_q)^2/4 = \pi d_{pq}^2 \tag{2.7}$$

where $d_{pq} = (d_p + d_q)/2$.

For a gas mixture, $\mathbf{c}_0$ represents the *mass average velocity*, a quantity such that for a simple gas $\rho\mathbf{c}_0$ is defined as the flux vector for the molecular mass. It is assumed that all the molecules move with $\mathbf{c}_0$, the value appearing in the momentum conservation equations. In particular, a collision is said elastic if there is no interchange of translational and internal energy.

2.1.5 Molecular magnitudes

Due to the fact that the intermolecular force declines as the inverse power of the distance at the moderate to high separation distances, a new issue appears in the estimation of the molecular diameter and the mean free path.
At the molecular level, changes in the cross-section are typically linked to the variation of the coefficient of viscosity with temperature at continuum level. For

each molecular model of the classic kinetic theory there is no chance to place the cross-section value inside a specific range, nor the precision in the representation of the viscosity-temperature variation of a real gas [47]. In both the analytical and numerical molecular models of gas flows it is remarkable the dependence from the changes in the effective cross-section.

To sum up, it is true that the continuum breakdown limit always ranges between the dilute gas limit and high fluctuations limit. As a consequence, the NS equations become meaningless below the level of significant statistical fluctuations. In the meanwhile, in a dilute gas the density and/or the characteristic dimension decrease. The range between these two limits becomes wider when the gas is more rarefied, while in the region where NS equations should be valid, it may occur a significant level of fluctuation if the gas is dense. The explanation for this last case is that, although the molecules are closely packed, when the density increases, the number of molecules that are involved in typical flows actually decreases [47].

2.1.6 Real gas behavior

Up to now, it was assumed the validity of Newtonian physics and it was excluded the possibility for the molecules to change in their nature as a result of collisions. In reality, for a real gas model both the chemical reactions and the absorption and emission of radiation have to be taken into account.
According to quantum mechanics, the Heisenburg uncertainty principle states that the product of the uncertainty $|\Delta r|$ in position and $|\Delta mc|$ in momentum is in the order of Planck's constant (2.8) [47]:

$$|\Delta r||\Delta mc| \sim h \tag{2.8}$$

For the general molecular model, the quantum description must be applied when dealing with light particles (e.g., hydrogen or helium) at extremely low temperature. Moreover, the classical model can be implemented when the number of available quantum states should be very large when compared with the number of molecules.

If the gas is not neutrally charged, the long range Coulomb interactions occur between the electrons (with magnitude lighter than the other particles) and the positively charged ions. In presence of an high degree of ionization, the field of study switches from kinetic theory and gas dynamics to plasma physics.
In principle, the force of interaction between real molecules is strongly repulsive at short distances, while it is weakly attractive at the larger ones. This last situation is often neglected in the simplest acceptable models. The degree of acceptability is typically measured in terms of sufficiently accurate correlations between theory and experiments.

For a gas, the condition of equilibrium implies that the thermodynamic coordinates and hence their functions do not change in time. In a non equilibrium

situation these quantities will change with time. The time occurring for a gas to move from the non equilibrium to equilibrium condition is called *relaxation time*. During this time, a gas element can travel through a certain distance (the *relaxation distance*).

In general, it is established a proportionality between the relaxation time and the mean collision time from one side and the relaxation distances and the mean free path from the other one. If the Kn number increases, for a typical gas flow the non-equilibrium regions become wider. In particular, in presence of an high degree of gas rarefaction, the entire flowfield is kept very far from equilibrium.
From a thermodynamic viewpoint, the kinetic temperature (defined in terms of velocity components in the flow direction) for a strong normal shock wave is twice the kinetic temperature based on the velocity components normal to the flow direction [47].

2.2 Statistical approach

The number of molecules in a real gas flow is so large that the description in terms of position, velocity and internal state of each molecule at a given time instant is not possible. Consequently, it is needed to switch to a statistical distribution, based on probability distributions [47].

2.2.1 Single particle distribution function in velocity space

Considering a sample of gas that is homogeneous in physical space and containing N identical molecules. Each of them can be described in terms of its velocity $\mathbf{c}$ (having components u, v and w in the direction of Cartesian axes) and its position $\mathbf{r}$ (with Cartesian coordinates x, y and z), defining, respectively the *velocity space* and the *physical space*, as reported in Figure 2.2. A molecule is here dot-shaped and it is defined in accordance to its velocity vector. The velocity distribution function $f(\mathbf{c})$ is identified by 2.9:

$$dN = Nf(\mathbf{c})du\ dv\ dw \tag{2.9}$$

where dN represents the number of molecules in the sample with velocity components in the range u to $u + du$, v to $v + dv$ and w to $w + dw$. It is possible to indicate with $d\mathbf{c} = du\ dv\ dw$ the volume element in velocity space. 2.9 can be rewritten according to 2.10:

$$dN = Nf(\mathbf{c})d\mathbf{c} \tag{2.10}$$

$f(\mathbf{c})$ is always a positive function bounded in the velocity space and going to zero when c tends to infinity.

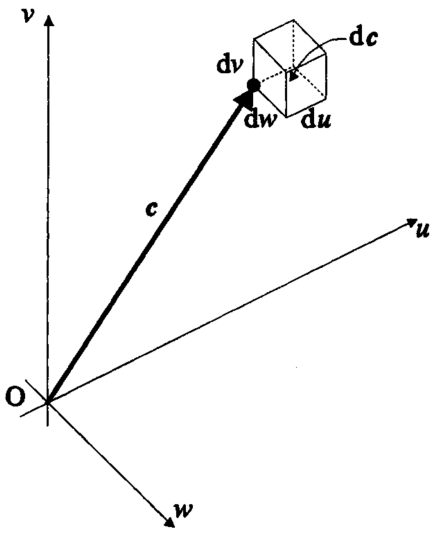

Figure 2.2: Typical molecule and element in velocity space, reproduced from [47].

Due to the fact that each molecule represents a point in the velocity space, the integration of the distribution function into the all domain provides the *normalization condition* (also called 0^{th}-order moment) (2.11):

$$\int_{-\infty}^{+\infty}\int_{-\infty}^{+\infty}\int_{-\infty}^{+\infty} f(\mathbf{c})du\ dv\ dw = \int_{-\infty}^{+\infty} f(\mathbf{c})d\mathbf{c} = 1 \tag{2.11}$$

At this point, it is necessary to establish the relationship between the distribution function and the average value of any molecular quantity Q, with the aim of providing a link between the macroscopic properties and the distribution function. According to the definition of *mean value* (or average value or 1^{st}-order moment) (2.12):

$$\overline{Q} = \frac{1}{N}\int_N Q\ dN = \frac{1}{N}\int_{-\infty}^{+\infty} Q\ f(\mathbf{c})Nd\mathbf{c} = \int_{-\infty}^{+\infty} Q\ f(\mathbf{c})d\mathbf{c} \tag{2.12}$$

In general, the macroscopic flow properties are functions of position and time.

The distribution function previously presented has to take into account also the position vector in velocity space $\mathbf{r}$ and the time coordinate t. As a consequence, $d\mathbf{r}$ represents the volume element in physical space, while the *phase space* given by the product $d\mathbf{c}d\mathbf{r}$ is defined as a multi-dimensional space, formed by the combination of physical and velocity space [47]. The *single particle distribution function in phase space* $\mathscr{F}(\mathbf{c},\mathbf{r},t)$ is defined according to (2.13):

$$dN = \mathscr{F}(\mathbf{c},\mathbf{r},t)\ d\mathbf{c}d\mathbf{r} \tag{2.13}$$

where dN is the number of molecules in the phase space element $d\mathbf{c}d\mathbf{r}$ that, in Cartesian coordinates, can be expanded into $dudvdwdxdydz$. dN is the number

of molecules with velocity components within u to $u + du$, v to $v + dv$ and w to $w + dw$ and space components within x to $x + dx$, y to $y + dy$ and z to $z + dz$. Instead of the fraction of molecules in the phase space element, $\mathscr{F}$ represents the number of these molecules. Since it is not normalized, when integrated into the whole phase space volume, it provides the total number of molecules in the system N.
The most general distribution function is the one for all the N molecules in the system. It means that at any instant the complete system of monoatomic molecules can be figured as a point in $6N$ dimensional phase space. The additional issue appears when considering the ensemble of more than one system [47].

By definition, a very small fraction of the volume of a dilute gas contains a molecule. Therefore, a two particle distribution function $\mathcal{F}^{(2)}(\mathbf{c}_1, \mathbf{r}_1, \mathbf{c}_2, \mathbf{r}_2, t)$ is enough to describe the binary collisions and it satisfies the principle of *molecular chaos* (2.14):

$$\mathcal{F}^{(2)}(\mathbf{c}_1, \mathbf{r}_1, \mathbf{c}_2, \mathbf{r}_2, t) = \mathcal{F}^{(1)}(\mathbf{c}_1, \mathbf{r}_1, t)\mathcal{F}^{(2)}(\mathbf{c}_2, \mathbf{r}_2, t) \tag{2.14}$$

The higher order distribution functions are involved in the study of dense gases.
In general, the dimensions of the phase space are determined by the least number of scalar variables that are needed to specify the position, velocity, orientation and internal state of a molecule. However, when dealing with a gas mixture, each species require a separate distribution function.
For sake of simplicity, the most important approaches to the kinetic theory treat gases like a single species of monoatomic molecules.

2.2.2 The Boltzmann equation

The velocity distribution functions provide a statistical description of a gas on the molecular level. Through a rigorous process, it is possible to move from the statistic approach to analytical solutions of problems in molecular gas dynamics.

The Liouville equation represents the fundamental statistical mechanics equation and it states the conservation of the N particle distribution function in $6N$ dimensional phase space [47]. This model establishes also the limits of validity of the *Boltzmann equation* that, for a simple dilute gas, can be formulated as 2.15:

$$\frac{\partial}{\partial t}(nf) + \mathbf{c} \cdot \frac{\partial}{\partial \mathbf{r}}(nf) + \mathbf{F} \cdot \frac{\partial}{\partial \mathbf{c}}(nf) = \int_{-\infty}^{+\infty} \int_{0}^{4\pi} n^2 (f^* f_1^* - f f_1) c_r \sigma \, d\Omega \, d\mathbf{c}_1 \tag{2.15}$$

On the other hand, for a gas mixture formed by a total of s separate species, a proper distribution function is needed for each species. In this case, the Boltzmann equation becomes a set of s simultaneous equations.
Focusing on a particular species p and indicating with q another generic one, the

Boltzmann equation can be written according to 2.16:

$$\begin{aligned} &\frac{\partial}{\partial t}(n_p f_p) + \mathbf{c}_p \cdot \frac{\partial}{\partial \mathbf{r}}(n_p f_p) + \mathbf{F} \cdot \frac{\partial}{\partial \mathbf{c}}(n_p f_p) \\ &= \sum_{q=1}^{s} \int_{-\infty}^{+\infty} \int_{0}^{4\pi} n_p n_q (f_p^* f_{1q}^* - f_p f_{1q}) c_{r,pq} \sigma_{pq} \, d\Omega \, d\mathbf{c}_{1q} \end{aligned} \tag{2.16}$$

As it can be noticed, the distribution function is extended for all the phase space dimensions, in order to take into account the internal degrees of freedom. Being the collision cross-sections of asymmetric molecules functions of the molecular orientation, these terms change with time as the molecules rotate between collisions. On the right-hand side of the Boltzmann equation appears the *collision term*. The main issue of the Boltzmann equation belongs in the nf product inside the partial derivatives, but, luckily enough, it is the only dependent variable of the equation. In the NS equations are involved the velocity components and, for establishing the equation of state, two of the thermodynamic properties are considered as dependent variables.

In the Boltzmann equations it is not possible to obtain analytical solutions when dealing with complex geometries or large phase disturbances. The computational meshes in phase space for numerical solutions present the issue related to the number of dimensions and the definition of bounds of velocity space [47].

2.2.3 Momenta of Boltzmann equation and derivation of conservation equations

The molecular quantity Q previously introduced can be either a constant or a function of molecular velocity.
Multiplying the Boltzmann equation by Q and integrating over the all velocity space, it is obtained a *moment of the Boltzmann equation*.
Performing the calculation, it is possible to end up with a monoatomic gas version of the conservation equations of continuum gas dynamics, the so called *transfer equation* or *equation of change* (2.17):

$$\frac{\partial}{\partial t}(n\overline{Q}) + \nabla \cdot (n\overline{\mathbf{c}Q}) - n\mathbf{F} \cdot \frac{\overline{\partial Q}}{\partial \mathbf{c}} = \Delta[Q] \tag{2.17}$$

When the quantity Q is either the mass m, the momentum $m\mathbf{c}$ or the kinetic energy $^1/_2\, mc^2$ of a molecule, these variables are said *collisional invariants*.
The collision integral goes to zero in the three equations for the collisional invariants and the average terms in the first member of 2.17 can be rewritten as macroscopic gas properties, leading to the *three conservation equations* of gas dynamics. Rearranging a little bit the previous expressions, one obtains:

1. the *conservation of mass* (2.18) for $Q = m$:

$$\frac{\partial \rho}{\partial t} + \nabla \cdot (\rho \mathbf{c}_0) = 0 \tag{2.18}$$

Introducing the concept of *substantial derivative* (2.19):

$$\frac{D}{Dt} \equiv \frac{\partial}{\partial t} + \mathbf{c}_0 \cdot \nabla \equiv \frac{\partial}{\partial t} + u\frac{\partial}{\partial x} + v\frac{\partial}{\partial y} + w\frac{\partial}{\partial z} \tag{2.19}$$

2.18 can be rearranged into a more general form (2.20):

$$\frac{D\rho}{Dt} = -\rho \nabla \cdot \mathbf{c}_0 \tag{2.20}$$

2. the vectorial *conservation of momentum* or *equation of motion* (2.21) for $Q = m\mathbf{c}$:

$$\frac{\partial}{\partial t}(\rho \overline{\mathbf{c}}) + \nabla \cdot (\rho \overline{\mathbf{c}\mathbf{c}}) - \rho \mathbf{F} = 0 \tag{2.21}$$

Manipulating 2.21 leads to a more general form (2.22), taking into account the pressure gradient and the viscous stress tensor:

$$\rho \frac{D\mathbf{c}_0}{Dt} = -\nabla p + \nabla \cdot \boldsymbol{\tau} + \rho \mathbf{F} \tag{2.22}$$

3. the *conservation of energy* (2.23) for $Q = {}^1/_2\ mc^2$:

$$\frac{\partial}{\partial t}({}^1/_2\ \rho \overline{c^2}) + \nabla \cdot ({}^1/_2\ \rho \overline{\mathbf{c}c^2}) - \rho \mathbf{c}_0 \cdot \mathbf{F} = 0 \tag{2.23}$$

Introducing the macroscopic quantities in 2.23, a more common expression showing the pressure, the *viscous dissipation term* Φ and the heat flux contribution $\mathbf{q}$ is found (2.24):

$$\rho \frac{De}{Dt} = -p \nabla \cdot \mathbf{c}_0 + \Phi - \nabla \cdot \mathbf{q} \tag{2.24}$$

Due to the vectorial nature of 2.21, the equations of conservation of mass, momentum and energy count for five equations (with dependent variables the three velocity components and two out of three thermodynamic properties, p, ρ and T). The viscous stress tensor $\boldsymbol{\tau}$ is a symmetric matrix and, remembering that its track leads to the pressure, it produces five dependent variables. The heat flux vector $\mathbf{q}$ represents three additional dependent variables. It is clear that the conservation equations do not constitute a complete set, because they contain a total of thirteen dependent variables.

A complete set arises in *inviscid* situations (both $\boldsymbol{\tau}$ and $\mathbf{q}$ move to zero), leading to the so called *Euler equations* [47].

For a monoatomic gas, the viscous stress tensor and the heat flux can be expressed according to 2.25 and 2.26:

$$\tau_{ij} = \mu\left(\frac{\partial u_i}{\partial x_j} + \frac{\partial u_j}{\partial x_i}\right) - \frac{2}{3}\delta_{ij}\mu\frac{\partial u_k}{\partial x_k} \tag{2.25}$$

$$q_i = -K\frac{\partial T}{\partial x_i} \tag{2.26}$$

Substituting these expressions inside the conservation equations produces a determinate set, representing for the monoatomic gas the NS equations of continuum gas dynamics.

In order to increase the validity of the NS equations, for e.g., it is possible to adopt an higher-order continuum equations, the *Burnett equations*. This proposal extends the validity of the continuum model also for more flows than the ones usually considered by the NS equations. The Burnett equations have the advantage of estimating in a more precise way the local Kn number [47].

2.3 Application of numerical method for transition regime flows

The Boltzmann equation is an accepted mathematical model at the molecular level, on which most of the analytical methods are built. On the other hand, a great number of numerical methods are essentially based on the direct simulation of the physics of the flow. However, one issue is due to the absence of a proper rigorous definition.
The increase of precision by inclusion of additional effects makes the programs harder to menage, introducing the need of performing more simulations for code verification before the "production runs" are carried out.

2.3.1 Direct Boltzmann CFD method

The first idea when dealing with the Boltzmann equation is to apply the conventional CFD methods.
The velocity distribution function is the only dependent variable for a simple gas and it can be estimated numerically by Finite Differences (FD) or Finite Volumes (FV) approach through a network of points or elements in the phase space.

One of the issue is the placing of the finite bounds for the domain, because only a limited fraction of them should belong from outside. The criticality of the situation arises when treating hypersonic or high-temperature flows, since in a few

moments a certain amount of molecules with high velocity respect to the bulk of the gas may have particular effects on the macroscopic flow properties [47].
Coupled simultaneous equations must be solved for each of the molecular species in a gas mixture.
Moreover, physical effects like chemical reactions and thermal radiation are difficult to withstand for the Boltzmann formulation (e.g., definition of the inverse collisions).
As a consequence, the direct solutions of the Boltzmann equation is limited to simple flow geometries, monoatomic gases and low Ma numbers.
The summation procedure, consisting in the replacement of the integrals with summation in the discrete approximations, reduces the computational cost proper of the collision term. In the early simulations, this method was represented by a Monte Carlo sampling technique. In order to guarantee the satisfaction of conservation laws, the least squares procedure was implemented for monitoring the error.
Noticeable results from the application of the Boltzmann CFD approach came when dealing with normal shock waves.

2.3.2 Deterministic simulation methods

Direct simulation methods model the real gas by introducing a large number of simulated molecules in a calculator.
The position coordinates, the velocity components and the internal state of each of the simulated molecules are stored and modified by time in a computer. The Lagrangian approach for the molecules studies the collisions and the boundary interactions in simulated physical space.
A certain degree of simplification when defining the boundary conditions is provided by the observation of the development of a steady flow through a physical real unsteady flow [47].

The first attempt of physical simulation method was the *molecular dynamics* (*MD*) *method*. Despite the procedure is described on probabilistic terms, the setting of the initial configuration for the molecules, the analysis of the evolution of the molecular motion (e.g., collision and boundary interactions) is deterministic.
The major drawback of this method is due to the fact that, for an established molecular size, flow geometry and gas density, the number of the simulated molecules is not a free parameter.

The number of molecules within one cubic mean free path provides a good estimation of the number of molecules of a typical flow. The Boltzmann equation is used in analysis of dilute gases. This phenomenon requires that the density should not be greater than double times the standard density.
Furthermore, many 2D MD simulations involve cylindrical molecules (instead of spherical ones), showing, as expected, non physical macroscopic properties.

2.3.3 Probabilistic simulation methods

In 1962 was presented the first probabilistic simulation method, the *test particle Monte Carlo method*.
In the transition regime, not only the molecule-surface interactions, but also the typical intermolecular collisions have to be taken into account. Starting from a given representation of the complete flow field, it is possible to choose an appropriate distribution function to be collected at precise locations in the phase space. According to the distribution, a huge number of "test particle trajectories" are simulated. They are assumed as the "target" gas for the estimation of typical intermolecular collisions [47].
A possible alternative would be to introduce a time variable and using a Lagrangian approach for each of the simulated molecules within a computer.
Differently from the MD method (the best choice for dense gas flows), the *Direct Simulation Monte Carlo* (*DSMC*) *method* can be typically adopted for dilute gas flows.
Many variants of the DSMC method have been introduced over the years respect to the original simulation. The main feature of all of these methods is certainly the uncoupling, over small time "steps" (compared to the mean collision time), of the molecular motion and the intermolecular collisions.

According to the classical kinetic theory methods (including the Boltzmann equation), here the main limitations are related to the assumption of dealing with dilute gases and the principle of molecular chaos. As a consequence, the DSMC method is not so suitable for those situations where there are significant long-range interactions (e.g., dense gases or highly ionized plasma).

In order to make easier the choice of the molecules for collisions and for the sampling of the macroscopic flow properties, the physical space network is implemented. Instead of the distribution function, in the DSMC method is analyzed the behavior of the individual molecules for the definition of the microscopic boundary conditions.

For reducing the computational effort, although the simulated molecules are of the correct physical size, they are in less amount respect to the real case, because each of them represents a fixed number F_N of real molecules. In this way, the properties can be specified through a distribution of values rather than of a single one for each simulated molecule [47].

As a rule of thumb, the computational time is directly proportional to the number of simulated molecules, while the computational efficiency of the DSMC method is significantly higher than that of the MD method. Until the electric field is a result of theoretical considerations or calculations external to the DSMC calculations, the method remains applicable for weakly ionized gases. Due to the presence of statistical fluctuations in the electron and ion number densities, the

field cannot be considered as an output of the simulations. The problem can be circumvented when the charge neutrality arises for very small Debye distances. Otherwise, an approximated theory for ambipolar diffusion can be implemented for fields in a shock front.

2.3.4 Discretization methods

The *lattice gas* cellular automata have an higher computational efficiency if compared to the DSMC method, but it is not so realistic from a physical viewpoint. The physical space is here discretized into a regular array of points (or nodes), whose information is contained in a word of approximately one byte. Operations on the individual bits of these words model the interactions between the nodes and they are performed in such a way the continuity and the momentum equations are satisfied similarly to real fluids. Nevertheless, it is difficult to determine the temperature and satisfying in the meanwhile the energy equation [47].
The main drawback is due to the fact that in the lattice gas model both the vacant and the occupied nodes are added to the storage memory.

The *discrete ordinate* or *discrete velocity method* takes advantage from the discretization of the velocity space, allowing the substitution of the Boltzmann equation with a set of non-linear hyperbolic differential equations.

2.4 Main issues associated to direct simulations

The original version of the Boltzmann equation was presented in 1872, but it was possible only in 1960s to perform direct simulations of gas flows putting aside the mathematical models that, on the other hand, do not completely accept the theory and the final outputs of simulation methods.
Although some attempts of providing a direct numerical solution of the Boltzmann equation were done, direct simulations remain nowadays more versatile.

Both the Boltzmann formulation and the DSMC method accept the assumptions of molecular chaos and dilute gas, but only the second one does not show dependence of inverse collisions. It means that the DSMC method can be applied to complex phenomena (e.g., ternary chemical reactions) that, instead, are not treatable by Boltzmann theory [47].

Because of the substantial absence of an accepted mathematical model at the particle level for dense gases and liquids, the deterministic MD method shows major consensus than the DSMC method. For the latter, concepts like the existence, uniqueness and convergence are significantly meaningless.
Technical features, like the need of sub-cells are not so practicable for analytical models, while the collisional steps in those cases where there are just one or two molecules in a cell produce important issues to menage with [47].

2.4.1 The choice of normalized or dimensional variables

It is preferable to obtain experimental outputs in a dimensionless form, although the basic physical data are always dimensional.
The original DSMC method dealt with unrealistic hard sphere molecular model and so, the data needed to be expressed in dimensionless form to be compared with experimental values. The specified mean free path came from the definition of a "cross section" variable proportional to the number of simulated molecules.

Nowadays, molecular models are sufficiently realistic for the simulation results to be directly compared with the measured values. If dimensionless outputs are needed, the normalization is finally applied to them.

2.4.2 The choice of statistical scatter and random walks

An high degree of statistical scatter is associated to the DSMC method, in many cases greater than the one associated to the real gas and so, a cumulative sample is recommended. The outputs usually present a time average for a steady flow or an ensemble average for an unsteady flow.

The DSMC method perfectly represents the equilibrium fluctuations and, for non-equilibrium situations, the maximum value of the density-velocity static correlation functions shows a linear proportionality with the temperature gradient, according with theory and light scattering experiments [47].

In the DSMC method there is not a proper concept of "convergence", like the one that, on the other hand, occurs by using the conventional CFD methods. When the sample quantity is close to the correct value, it means a gradual reduction in statistical scatter, usually indicated as a deleterious phenomenon.

If the molecular quantities are conserved on the average in any of the simulation procedures, random walks can increase. *Weighting factors* are needed for trace species, since they can be represented through very small samples if the number of simulated molecules was the same for each species.
Furthermore, in each collision momentum and energy are only conserved on average and each deviation represents a random walk in that quantity. When the position coordinates or the velocity components are rounded-off for storing as discrete values, random walks can arise. In order to avoid it, the discrete ordinate methods limit the collisions to a discrete and pre-determined number that exactly conserve those values [47].

2.4.3 The choice of computational approximations

The most important approximation from a computational viewpoint in the DSMC method are related to the ratio of the number of simulated molecules respect to number of the real ones, the uncoupling between the molecular motion and

collisions over a certain time step, and the finite cells and sub-cells sizes in physical space [47].

It is hard to find an exact value at which the fluctuations change their nature or become unstable. Sometimes, the number of simulated molecules may be not sufficient and therefore, the important part of the distribution remains not properly populated.

When both the time step and the cell size are tending to zero, the DSMC simulation becomes more accurate. However, there is not a corresponding Courant condition for stability as occurring in the continuum CFD analysis.

Originally, the DSMC method considered the molecules in a cell as representative sample of the ones present in the location of the cell in real situations. When adopting potential collision pairs, the relative position of the molecules within the cells were neglected.

According with many CFD methods, the vorticity is defined by the velocity gradients between the cells. On the other hand, the DSMC method considers the vorticity in a cell an improvement on most CFD methods. The linear dimension of the cell should be small when compared with the scale length of the macroscopic flow gradients in the direction in which the dimension is measured.
As a rule of thumb, $\delta \sim \frac{1}{3}\lambda$ and $\Delta t << \tau$

2.5 The statistics behind DSMC simulations

The results of this thesis that will be presented in 4.1 and 6.1 seem to concern only one simulation, without references to statistical averaging as occurs, on the other hand, in a generic Monte Carlo method. As already said in this chapter, the DSMC is intrinsically a statistical method, because it is founded on probabilistic simulations of collisions between particles. In this section, some clarifications are provided, focusing on the need of repeating the simulation more than once, with the aim of estimating the average behavior of particles inside the system.

In a single execution of a DSMC simulation, microscopic properties proper of particles inside each simulation cell during a certain time interval are averaged, in order to compute the corresponding macroscopic properties (e.g., velocity, temperature, pressure, density, etc.). The objective is to reach the stationary state of the analyzed system, calculating a time averaging at each time step.

In the DSMC simulations some minimal changes are appreciable in the outputs because of the intrinsic probabilistic nature behind the collisions and because of the generation of particles. These discrepancies may be limited by increasing the number of simulated particles from one side and by considering longer time intervals for testing (with a consequent improved time averaging) on the other one.
By the way, if the aim is to obtain a better estimation of macroscopic properties

with a fixed target of statistical precision (e.g., in order to asses the uncertainty of the outputs), it is possible to adopt the following strategies, depending on the established target of accuracy and on the available computational resources:

1. **Perform more simulations**: consisting on changing the initial conditions (but keeping the same physical setup), performing more independent simulations and, finally, averaging the such obtained outputs. The advantage of this procedure is to flatten the statistical fluctuations, offering to the user a confidence interval for the outputs.

2. **Longer simulations or more particles involved**: consisting on taking into account larger time intervals or increasing the number of particles to improve the statistical precision behind a single execution.

The classification provided above is quite general. Therefore, some distinctions between stationary and transient simulations must be reported.

2.5.1 Stationary simulations

This condition is not so relevant for the purpose of this thesis. Anyway, it is described in this section for an exhaustive description of the functioning of the DSMC method. In this case, the objective is to move the system to a stationary state. In other words, at that moment, the user does not observe any appreciable change in the properties of the system as time goes on. At each DSMC simulation, the flux properties are averaged over a longer time interval, until the steady-state condition is reached. However, if the purpose is to get an accurate estimation of macroscopic properties with such defined statistical uncertainties, the following options are acceptable:

1. **Perform more simulations**: more independent simulations are carried out in order to reduce the effects of occasional fluctuations.

2. **Longer simulations**: enlarging the simulated time in order to collect more data, with an associated improvement of the quality of the averaging.

2.5.2 Transient simulations

This context is more familiar for the purpose of this thesis, being involved a transient accident scenario. In this condition, the system evolves during time and, therefore, the dynamic behavior of the system is more important than a single steady value. Particular care must be devoted to the improving techniques mentioned in 2.5:

1. **Time statistic**: the time evolution of the system is tracked during the simulation. Because of the unsteady flux properties during the simulated time,

the time averaging described previously is no more useful, because each time step represents a different point of interest.

2. **Perform more simulations**: when treating phenomena that can be either extremely quick or localized in time, performing different independent simulations with different initial conditions may be still good in order to obtain a better estimation of the statistical precision during a transient analysis.

3. **More particles involved**: it should be useful to reduce the statistical noise during each time step, offering a more accurate evolution of the system.

The DSMC simulation of a LOCA in the HCPB blanket analyzed in this thesis takes a very long time to move from one iteration to the following one, being involved a high number of particles close to the inlet region. As a consequence, a massive computational effort is required. All the improving techniques above mentioned are here very difficult to be applied, being limited the computational resources available to the user. Nevertheless, OpenFOAM software is particularly versatile on averaging the microscopic properties of particles and sending in output the corresponding macroscopic ones with a good estimation of the confidence level. For this reason, none of the previous improving proposals was adopted, leaving to the software the task of performing a precise statistical estimation at each time step.

Chapter 3

Modeling approach

3.1 Accident scenario

The accidental transient considered in this thesis is a Loss-Of-Coolant Accident inside the EU DEMO reactor Vacuum Vessel (VV). It is typically a consequence of a plasma transient event (e.g., Edge Localized Modes - ELMs, Vertical Displacement Events - VDEs, runaway electrons - RE, or disruptions), causing a quick rising of Plasma-Facing Surface (PFS) temperature until EUROFER-97 structure may fail. Once the FW breaks, a significant portion of cooling channels will remain uncovered, leading to the coolant release inside the plasma chamber [3].
According to the HCPB configuration, the released coolant would be helium at 8 MPa and $300 - 520\ ^{\circ}C$. Due to the large pressure difference with respect to the plasma chamber environment (normally in high-vacuum conditions and pressurized when the coolant expands), a high underexpanded jet will be developed (as previously described in 1.6.2) with important effects on the VV walls.

The Vacuum Vessel Pressure Suppression System (VVPSS) of the EU DEMO (schematized in Figure 3.1) is designed to avoid over-pressurization. For instance, it may consists of a low-pressure environment separated from the VV by means of one or more Burst Disks (BDs) that actuate passively when the pressure reaches 1.5 bar (granting the communication between VV and VVPSS). It is coupled with one or more active "bleed valves" that start working in case of small leakages [1].

The transient analyzed in this document starts at the time of the break occurrence ($t = 0\ s$) and stops when steady-state conditions are reached inside the VV.

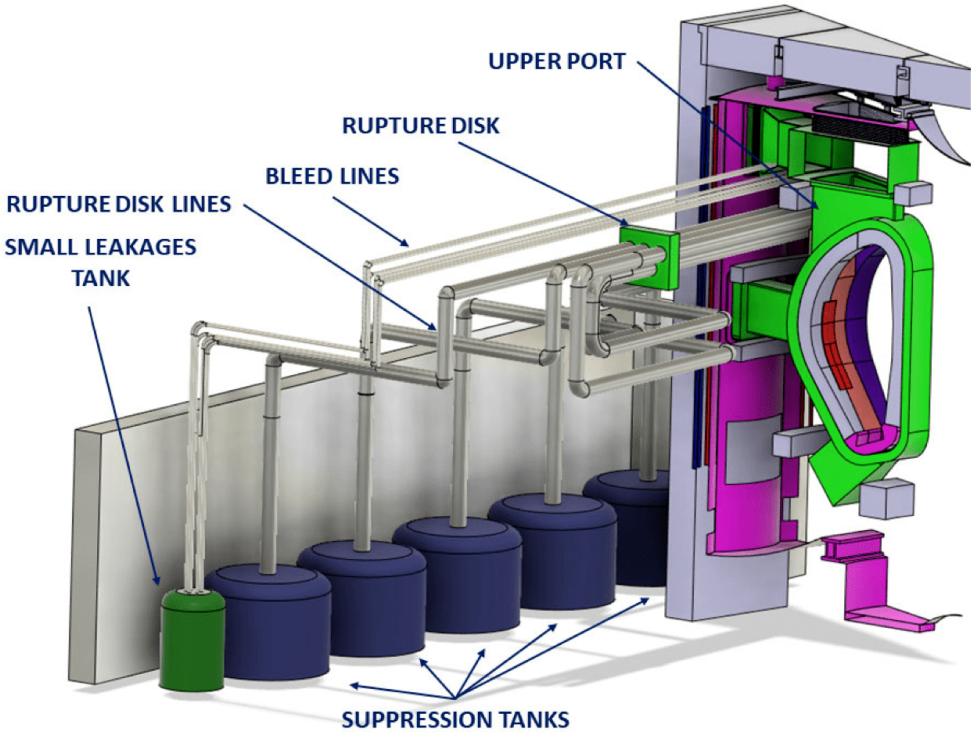

Figure 3.1: VVPSS CAD of the EU DEMO reactor, reproduced from [48].

3.2 SALOME Platform

SALOME is an open-source software adopted for pre- and post-processing in numerical simulations, able to perform industrial and physical analysis [49]. The platform is extensible and can integrate users' computational codes or modules in a very simple way. Among all its features, it includes a powerful open-source parametric CAD modeller, a mesh generator, a computational code supervisor and many data analysis and processing tools [50] (e.g., ParaVis, a module designed for scientific visualization, based on the free software ParaView [49]). Physical solvers are not included in SALOME, but this platform offers an IT environment suitable for its integration.

SHAPER is a parametric and variational CAD modeler. The graphical interface is versatile for drawing and technical modelling of complex computational domains. It allows an interactive application of dimensions and constraints to a sketch. The parametric aspect ensures that the final shapes are automatically updated when a CAD element parameter is modified [50].
SALOME is the CAD modeler adopted for this thesis.

3.3 Domain description

Ideally, a rigorous 3D analysis would require the entire free volume available in the VV to be taken into account in the definition of a computational domain. However, having in mind the idea of limiting as much as possible the computational effort, some simplifications are introduced:

(a) The simulation outputs will not be affected by the flow in the gaps between different Breeding Blanket segments. It means that the fluid domain occupies the entire plasma chamber, leading to a left-right symmetry that allows to consider only one half of the original domain.

(b) In principle, the up-down symmetry is wrong because of the presence of the divertor. However, in order to further simplify the original domain, the up-down symmetry geometry is considered anyway.

(c) The flow entering in the VV is mainly oriented radially towards the center of the torus. As a consequence, the analysis would be reduced to a 2D radial-poloidal geometry in the upper half of one side of the torus.

The CAD domain together with the adopted boundary conditions are reported in Figure 3.2.
As reference LOCA scenario (the worst among those identified as Design Basis Accidents - DBAs), a rupture area of 1 m^2 is assumed for the FW on the outboard (OB) BB. The total flow area offered to the plasma chamber corresponds to the one of 262 ($\sim 0.0308\ m^2$) cooling channels in the HCPB BB [3]. This surface is lumped into an equivalent circular inlet on the OB side, allowing to estimate the equivalent diameter (D) for a circular inlet region (3.1):

$$\frac{D}{2} = \sqrt{\frac{0.0308}{\pi}} = 0.099\ m \tag{3.1}$$

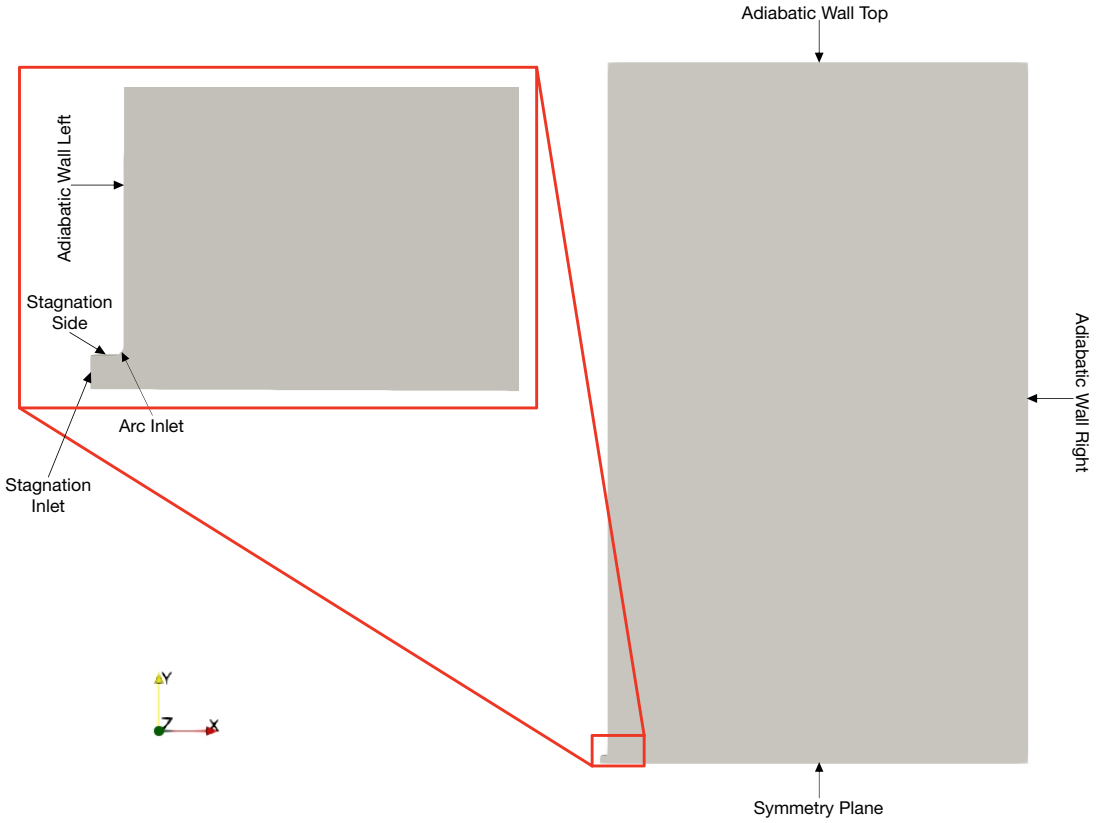

Figure 3.2: Computational domain and boundary conditions of the 2D case.

3.4 OpenFOAM

OpenFOAM (Open-source Field Operation And Manipulation) [4] is a multiphysics computational fluid dynamics software, able to model complex products operating under real-world conditions. It is chosen for a huge number of applications [51], such us:

- Combustion
- Molecular dynamics
- Tracing of lagrangian phase
- Direct Simulation of Monte Carlo (DSMC)
- electromagnetic simulations

Because of its good performances in the evaluation of the solution of the kinetic Boltzmann equation for medium into a wide range of values of Kn number, this successful simulation tool is the one chosen in this thesis.

3.5 Simulation setup

The setup of the 2D DSMC transient simulation is described step by step in this section.

3.5.1 Thermal-hydraulics boundary conditions

Looking at Figure 3.2, the boundary conditions can be classified as follows:

- **Stagnation Inlet**: This boundary condition derives from the assumption of resting helium inside the vessel (e.g., stagnation conditions). It is mandatory to define the total pressure, the total temperature and the supersonic static pressure that have to be adopted when the flow at the inlet becomes sonic or supersonic.
  The initial values of pressure and temperature (static values) together with the sound speed of helium at these conditions and the particle density close to the inlet (look at 3.5.3) are reported in Table 3.1, while the total quantities (p_t and T_t) are computed as in 3.2 and 3.3:

  $$\frac{p_t}{p_s} = \left[1 + \frac{\gamma - 1}{2}(Ma)^2\right]^{\frac{\gamma}{\gamma-1}} \tag{3.2}$$

  where γ is the ratio of the specific heat at constant pressure c_p and at constant volume c_v of helium, while Ma is the Mach number (ratio between the fluid speed at the Inlet and the sound speed in the helium). Due to the fact that the inlet section is the minimum one, sonic flow conditions occurs, leading to the expected $Ma = 1$. Of course, Ma number changes during the simulation and, therefore, it is re-computed at each solver iteration and updated in 3.2.

  $$\frac{T_t}{T_s} = 1 + \frac{\gamma - 1}{2}(Ma)^2 \tag{3.3}$$

  where T_s is static temperature (683.15 K).

- **Stagnation Side**, **Arc Inlet**, **Adiabatic Wall Left**, **Adiabatic Wall Top**, **Adiabatic Wall Right**: They adopt the classic setting for walls (e.g., no slip, smooth and adiabatic).

- **Symmetry Plane**: Taking into account the symmetry in the bottom part of the domain, the "Symmetry Plane" condition is selected for the lower boundary.

Fluid	$T_{in}[K]$	$p_{in}[kPa]$	$u_{in}[ms^{-1}]$	$n_{in}[m^{-3}]$
Helium	683.15	1	1537.9	10^{23}

Table 3.1: Initial conditions of the 2D case.

There are not outlet boundaries because the domain (excluding the inlet) is closed until the burst disks fail. However, this extreme situations is not considered in this simulation.

3.5.2 Initial conditions

It is very difficult to predict in advance the right value of the static pressure, because it is influenced by the chosen time scale of the phenomenon. For sake of simplicity, a constant inlet static pressure is adopted ($p_{in} = 1\ kPa$), leading to an initial pressure ratio (1.6.2) equal to 10^6 if compared to the high vacuum conditions in the plasma chamber ($p_{vacuum} = 1\ mPa$).
The transient analyzed takes a few tens of milliseconds to reach a steady-state condition, leading to a reasonable assumption of constant inlet pressure, especially if compared with the timescale spent by the Primary Heat Transfer System (PHTS), in the order of some seconds [1].

The high rarefaction of helium after a short distance from the inlet causes the need to discard the traditional CFD tool (proper of continuum) and switching to a statistical approach represented by the DSMC method (2).
The parameter that provides an estimation of the nature of the flow regime is the Kn number (2.1.1), a dimensionless quantity that can be written as 3.4:

$$Kn = \frac{\lambda}{L} = \frac{k_B T}{\sqrt{2}\pi\sigma^2 p L} \tag{3.4}$$

where λ is the molecular mean free path, L is the characteristic length (in this simulation it is represented by the distance between the inlet and the wall in front of it, $L = 3\ m$), $k_B = 1.3806 \cdot 10^{-23}\ J/K$ is the Boltzmann constant, $T = 683.15\ K$ is the temperature of the system, σ is the particle diameter (for the helium, $\sigma = 280 \cdot 10^{-12}\ m$) and p is the pressure of the system [1].
The previous expression gives for $p = 1\ kPa$ (constant inlet static pressure) and for $p = 1\ mPa$ (high vacuum conditions of the plasma chamber), respectively, $Kn = 9.0257 \cdot 10^{-6}$ and $Kn = 9.0257$.
Having in mind the classification provided in 2.1.1, a continuum region appears at the inlet and in the region closer to it, while a transition region develops further.

3.5.3 DSMC initialization

Before running the simulation in OpenFOAM, it is mandatory to initialise the equilibrium density of particles in the domain (3.5). In this case, as pressure is selected the one inside the VV ($p_{vacuum} = 1\ mPa$):

$$n_{eq} = \frac{p}{k_B T} = \frac{10^{-3}}{1.3806 \cdot 10^{-23}\ 683.15}\ m^{-3} = 10^{17}\ m^{-3} \tag{3.5}$$

The temperature of helium entering inside the domain is imposed equal to the static temperature ($T_s = 683.15\ K$) and the velocity field inside the vacuum chamber is imposed null.
Being the pressure at the inlet fixed to $p_{in} = 1\ kPa$, the initial number of particles inserted inside the domain is $N_{particles} = 599898$, while the particle density close to the inlet can be computed as in 3.5, leading to roughly $n_{in} = 10^{23}\ m^{-3}$.

3.5.4 DSMC properties

Once the DSMC simulation is initialised, it is needed to define the DSMC properties to be kept during the transient. In order to do that, a Matlab [52] script has been developed (detailed in A). Furthermore, this tool provides some mesh and time discretization parameters reliable for the problem under investigation. For sake of simplicity, all the helium properties of interest for the simulation are listed in 3.2:

Fluid	$\boldsymbol{m_{ref}[Kg]}$	$\boldsymbol{\sigma[m]}$	$\boldsymbol{iDoF[-]}$	$\boldsymbol{\omega[-]}$	$\boldsymbol{n_{in}[m^{-3}]}$
Helium	$6.65 \cdot 10^{-27}$	$280 \cdot 10^{-12}$	0	0.66	10^{23}

Table 3.2: Helium properties.

where m_{ref} is the molecular mass of helium, σ is the Van Der Waals diameter [53], $iDoF$ is the number of internal Degrees of Freedom, ω is the viscosity index [47] and n_{in} is the particle density close to the inlet, (reported in 3.5.3).
Some parameters proper of the kinetic theory are defined: the mean free path (3.6), the mean molecular speed (3.7) and the mean collision time (3.8). Clearly, these expressions provide different outputs depending on the equilibrium density (3.5) and, therefore, on the pressure ($p = p_s = 1\ kPa$ close to the inlet and $p = 1\ mPa$ as the gas expands).

$$\lambda = \frac{1}{\sqrt{2}\pi\sigma^2 n_{eq}} \tag{3.6}$$

$$c_{mean} = \sqrt{\frac{3k_B T}{m}} \tag{3.7}$$

where $m = PM \cdot m_{ref}$ (with $PM = 4.003 \cdot 10^{-3}\ kg$ representing the molecular weight of helium).

$$\tau = \frac{\lambda}{c_{mean}} \tag{3.8}$$

At this point, it is simple to estimate the Kn number as in 3.4.
After that, some DSMC parameters useful for the simulation can be set. Z.X. Sun at al., recommended in [54] to use a number of DSMC particles per cell equal to $NPC = 7$. Then, the characteristic grid length (3.9, defined as 1/3 of λ) and the time step (3.10, defined as one order of magnitude lower than the mean collision time) are computed:

$$l_{char} = \frac{\lambda}{3} \tag{3.9}$$

$$\Delta t = \frac{\tau}{10} \tag{3.10}$$

Having said that, it is useful to estimate the scaling factor (e.g., the number of physical particles per DSMC particle), as reported in 3.11:

$$f = \frac{(l_{char})^2 n_{eq}}{NPC} \tag{3.11}$$

It is highly recommended for f to not exceed $f_{suitable} = 10^8$ and it must definitely avoid the maximum allowable value equal to $f_{max} = 10^{12}$ [54]. For this reason, when $f > f_{max}$ it is needed to adjust f one or two times, as described in A.

3.6 cfMesh

cfMesh is a library for mesh generation implemented within the OpenFOAM framework and supporting hexa-dominant, tetrahedra, and polyhedra meshes in 2D and 3D. This tool can generate high-quality industrial meshes in such a small time [55]. The main idea behind this mesher is to minimize the number of algorithms that can be further extended and can be combined into various meshing workflows, tailored to the need of a specific problem [56].
Meshing process starts by creating a so-called mesh template from a given input geometry and the user-specified settings. The template is later on adjusted to match the input geometry. The procedure of fitting the template to the input geometry involves a certain tolerance to poor quality input data [55].
cfMesh is the mesher adopted for this thesis.

3.7 Applications and Dictionaries

3.7.1 Applications

In OpenFoam environment, applications cover the role of reading and writing a set of data files associated with a particular case. In this thesis, only one application is considered during the simulation:

(a) **dsmcFoam**
According to [4], this application is a DSMC solver for 3D, transient and multi-species flows. It includes some additional functions, able to compute at each time step some relevant flow fields, such as *rhoN*, *rhoM*, *dsmcRhoN*, *linearKE* and *internalE*. For this problem, the high rarefaction of helium diffusing inside the domain and the large values of the Kn number make this tool the best choice.

3.7.2 Dictionaries

In OpenFOAM environment, the dictionaries are adopted to specify data or the location where data entries are found by means of *keywords*. Any dictionary can host one or more sub-dictionaries, each one indicated with a specific *name* [4]. The fundamental dictionaries required to solve the problem are listed below:

1. **controlDict**
All the essential parameters for the creation of an OpenFOAM database are reported in this dictionary. The user must specify the time controls and the interval for the autosaves (*writeInterval*) [4].
Because of the unsteady nature of the phenomenon, it is mandatory to define a proper time-step (*deltaT*) size and, therefore, at which physical time update the calculation. In particular, the time step is chosen equal to 83 ns according to the results of the Matlab script in A, while the interval for the autosaves (*writeInterval*) is initially set equal to 5 μs.
Consistently with the application definition, the solver selected is *dsmcFoam*.

2. **meshDict**
Meshing process follows the settings indicated in this dictionary and consists of only two mandatory settings:

   - *surfaceFile*: a line of text where it is pointed the CAD of reference ("full_cad.stl" in this case).
   - *maxCellSize*: a line of text where it is defined the maximum cell size reached during meshing process [55]($2.17 \cdot 10^{-2}$ m in this simulation).

Because of the poor results obtained with a default mesh, in this simulation were activated two local refinement options:

- *minCellSize*: a line of text where specifying the automatic refinement of the mesh template ($2.17 \cdot 10^{-2}$ m in this case). It performs refinements in those regions where the cells are bigger than the estimated feature size. In this way it is minimized the computational effort when dealing with a CAD of high dimensions.
- *objectRefinement*: a line of text where it is declared which zones have to be refined inside the volume by means of a supporting object [55] (in this case a *sphere* of *cellSize* equal to $9.0257 \cdot 10^{-4}$ m and centered in the origin of the cartesian orthogonal system).

3. **blockMeshDict**
   This file represents the mesh generation utility built-in in OpenFOAM. It generates parametric meshes with grading and curved edges. The main idea behind this tool is to decompose the domain geometry into sets of up to 3D hexahedral blocks (with edges such as straight lines, arcs or splines). The user can specify the number of cells in each direction of the block [4].

4. **meshMetaDict**
   This file is automatically generated with blockMeshDict. Differently from the previous one, the boundaries of the flow domain have to be adjusted by hands and they are subdivided into *patch* (only for the inlet), *symmetryPlane* and *wall*.

5. **decomposeParDict**
   This tool is useful when performing the simulation in a cluster. It is required for parallel meshing using MPI. The *numberOfSubdomains* indicated by the user must be in accordance with the number of nodes used for the parallel run [55].

3.8 Mesh generation

The preliminary step when dealing with a gas flow is to estimate which level of gas flow description is better to approach the problem from a computational viewpoint. The helium entering in the Vessel shows a quick expansion and becomes highly rarefied. This fact means that the CFD approach based on the NS equations provides suitable results in a small region close to the inlet. After that, the Kn number (2.1) overcomes the upper bound of 0.1, meaning that it is needed to switch to a computational model more representative of the physics of the phenomenon: the DSMC method based on the kinetic Boltzmann equation, as described in 2.

The generation of a suitable mesh is a mandatory step in any CFD analysis, as it strongly influences the outputs of the simulation. This passage is still important in a DSMC method. The problem under investigation requires a mesh that has to be fine enough close to the inlet, where the continuum assumption (and so the CFD approach) is valid, and coarse enough further away, where the rarefaction (and therefore the DSMC method) is highly predominant. An uniform fine mesh for the entire domain is not recommended since it largely increases the computational cost with no meaning. The clever approach is definitely to discretize the domain with very fine cells near the inlet region, which become progressively bigger moving forward (look at Figure 3.3).

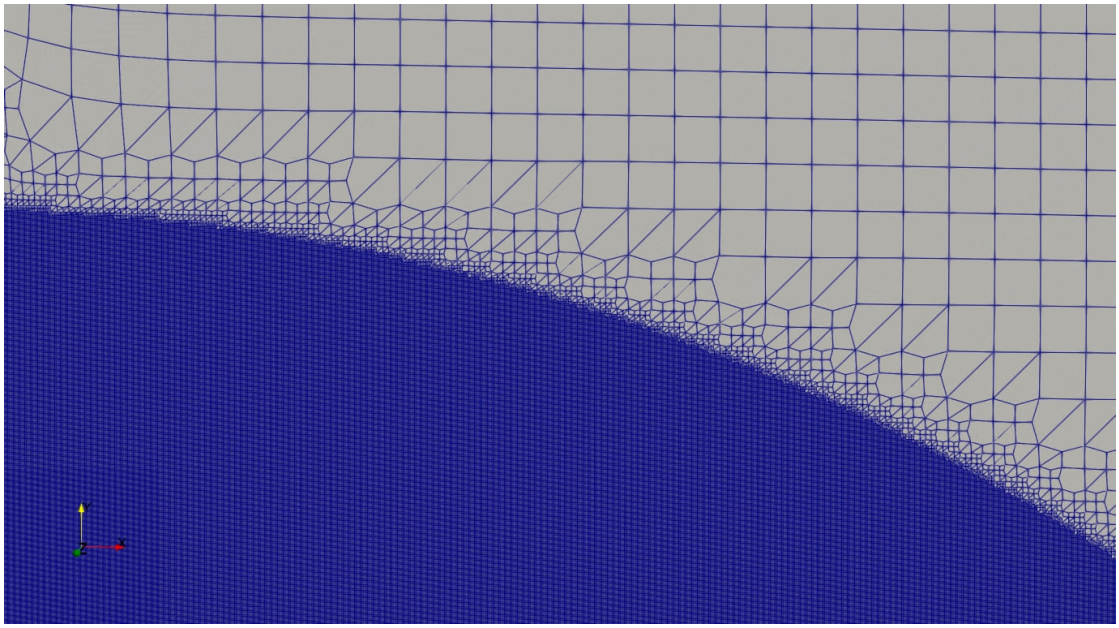

Figure 3.3: Transition of cells for the 2D model mesh.

Furthermore, the problem under investigation needs a very small time step (83 ns, according to A) to follow the shock front propagation, ending up with an enormous number of time steps required to carry out the simulation for the all transient.

3.8.1 Mesh refinement strategy

cfMesh tool *cartesian2DMesh* generates 2D meshes mainly formed by hexahedral cells, with polyhedra in the transition regions between the cells of different size. By default, it provides one boundary layer, which can be further refined if needed. The geometry is given in a form of a ribbon in the x-y plane and extruded in the z direction. Furthermore, this workflow can be run by means of MPI parallelisation,

which is intended for generation of large meshes, that do not fit into the memory of a single available computer [55].

In the OpenFOAM evironment, it is mandatory to indicate the reference CAD (*surfaceFile*), together with the minimum and maximum cell sizes ($2.17 \cdot 10^{-2}$ m in this case) and, eventually, a proper refinement (*objectRefinements*). For the latter, it is chosen to use a sphere centered in the origin of the cartesian axes and with unitary radius of cells of smaller dimensions ($9.0257 \cdot 10^{-4}$ m in this case). The final static mesh is reported in Figure 3.4.

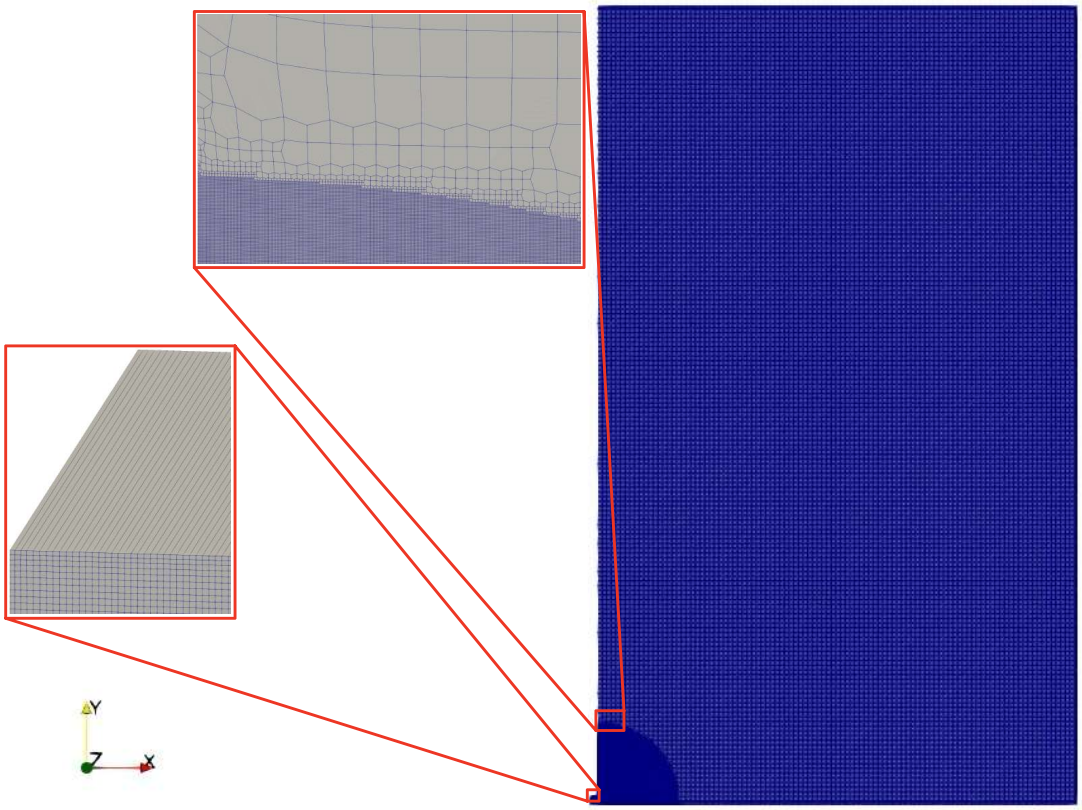

Figure 3.4: Static mesh adopted for the 2D model.

The obtained static refinement results into a mesh with 1858501 total cells. The selected cell size can be considered affordable for a 2D simulation, but it is practically unfeasible for a 3D simulation, because of the sharp increase in the number of additional cells due to the selected *obejectRefinement*.

3.9 ParaView

Among all the professional readers included in the official Ubuntu and Debian repositories, ParaView represents one of the most powerful open-source multiple-platform applications for interactive, scientific and technical visualization [57].
It is designed to facilitate remote visualization of datasets, generating Level of Detail (LoD) models to maintain interactive frame rates for large datasets. It is located on top of the Visualization ToolKit (VTK) libraries. ParaView is an application thought for data parallelism on shared-memory or distributed-memory multicomputers and clusters to analyze datasets in the order of terascale. Nevertheless, it can also be run as a single-computer application [58].
The data analysis can be performed interactively in 3D or programmatically by means of ParaView's batch processing technique. Once more, during visualization or elaboration this software allows to add a huge number of filters that can be applied in cascade for a specific dataset [57].
ParaView is the post-processing software adopted for this thesis.

Chapter 4

First phase of LOCA

4.1 Results

The simulation outputs for the first part of the transient at three different time steps are reported. This choice is based on the evolution of the Mach disk inside the VV. In particular, $t = 10\ \mu s$ (the time at which the jet is approaching the exit of the inlet region), $t = 100\ \mu s$ (starting of the jet expansion in the VV) and $t = 160\ \mu s$ (the time at which the jet overcomes the refinement region) are selected.

4.1.1 Flow field

The first instants of the jet evolution are shown in Figure 4.1. The green lines appearing over the jet front in Figure 4.1(a) are due to the temperature condition for the helium particles that were still present in the domain at $t = 0\ s$. The velocity of these particles corresponds to the mean molecular speed found in 3.7. As it can be appreciated, once the high pressure fluid overcomes the inlet region, the free expansion causes the development of a planar front (look at Figure 4.1(a)) which seems to be not sensible to the finite shape of the rupture. After that, the jet experiences the spreading (or diffracting) on the side, according to a spherical profile (look at Figure 4.1(b)). As already seen in 1.6.2 and 1.6.3, the preliminary phase of the jet is followed by the formation of a second shock, such as the Mach disk (look at Figure 4.1(c)). In this initial phase of accident scenario, the jet evolution is approximately the same of a free underexpanded jet startup, because the change of geometry has not be felt yet by the jet [1].
The average Mach number in the domain (look at Figure 4.2) is defined as a ratio of the velocity field and the sound speed of helium (4.1):

$$Ma = \frac{U_{Mean}}{c} = \frac{U_{Mean}}{\sqrt{\gamma\ R_m\ T}} = \frac{U_{Mean}}{\sqrt{\frac{5}{3}\ \frac{R}{PM}\ T}} = \frac{U_{Mean}}{\sqrt{\frac{5}{3}\ \frac{8.314}{4.003 \cdot 10^{-3}}\ T}} \tag{4.1}$$

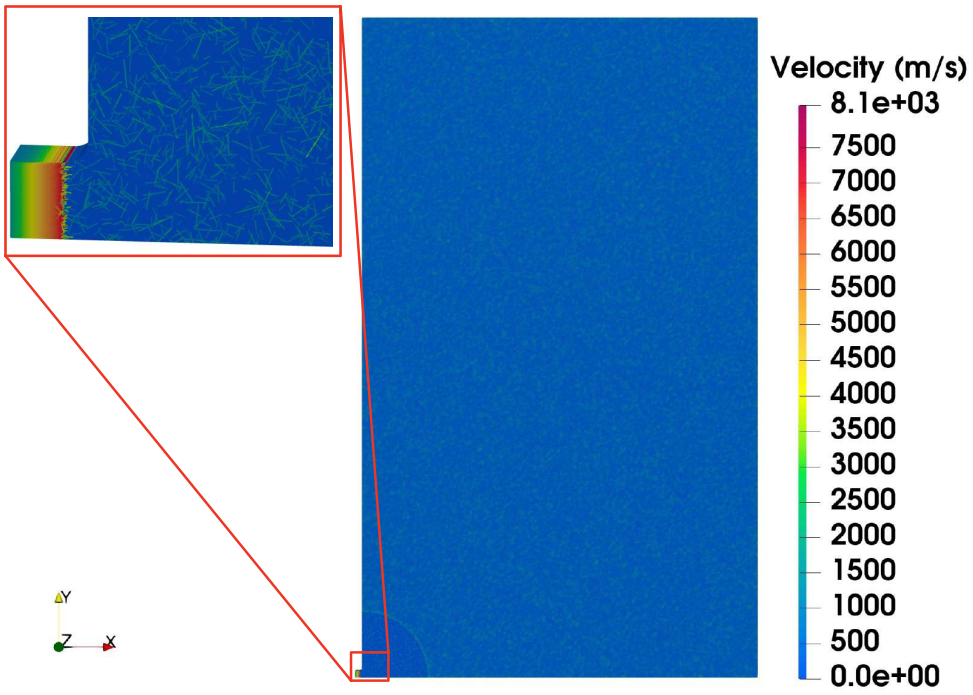

(a) $t = 10\ \mu s$

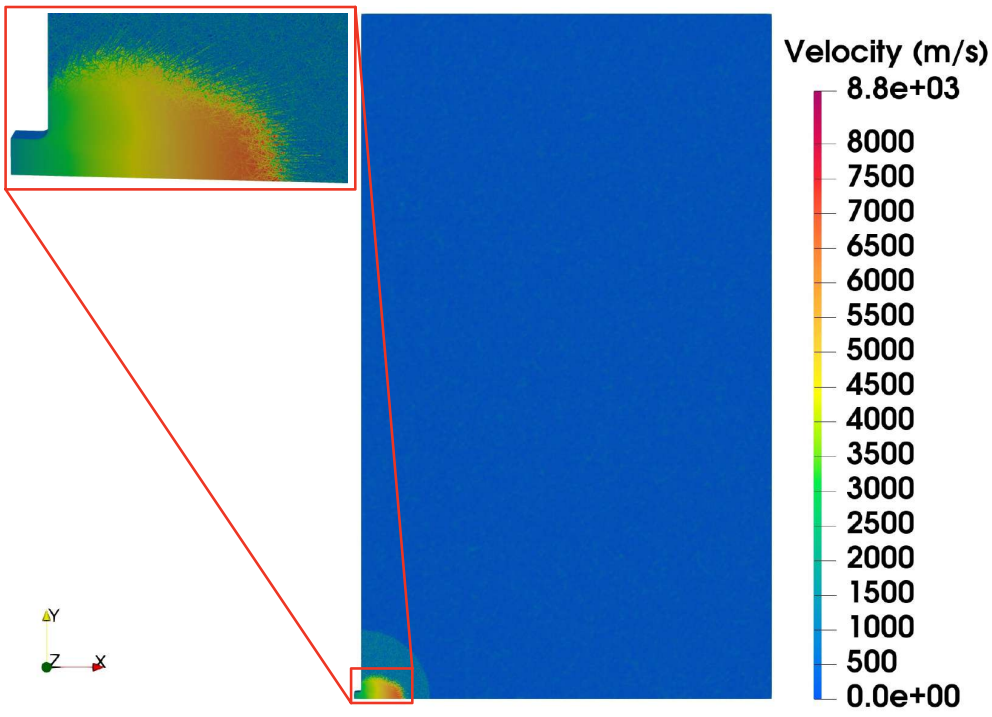

(b) $t = 100\ \mu s$

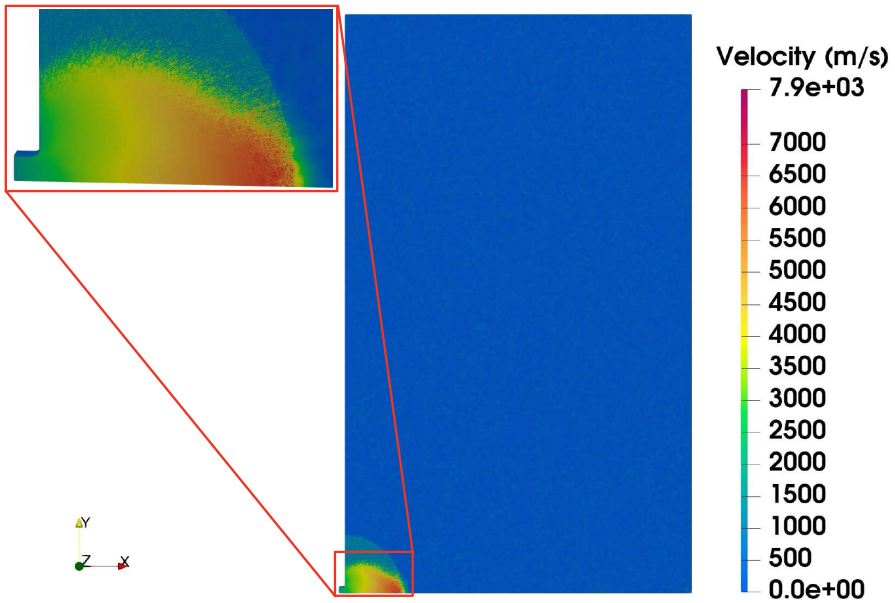

(c) $t = 160\ \mu s$

Figure 4.1: Evolution of the flow field during the jet startup on the vertical plane.

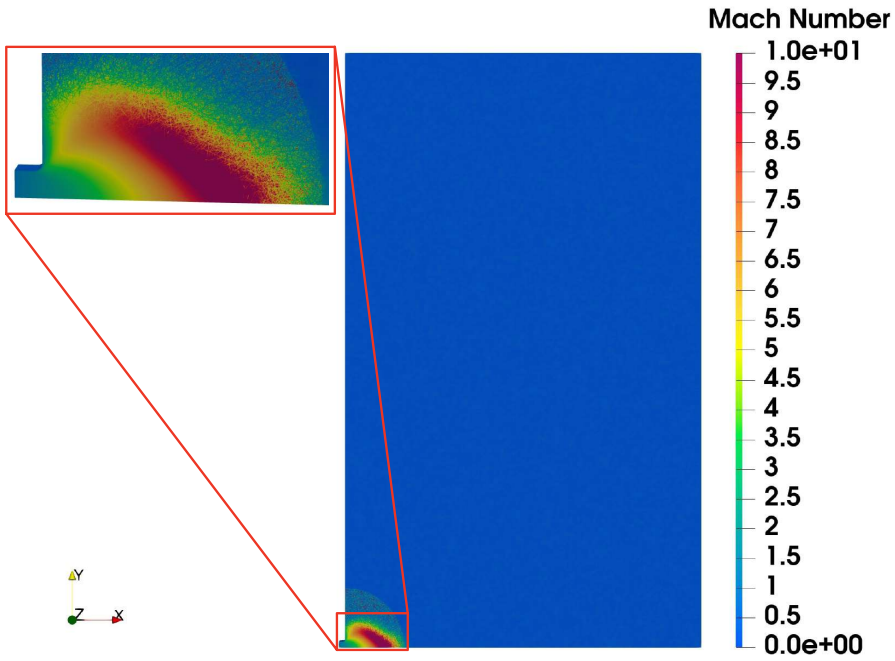

Figure 4.2: Mach number distribution on the vertical plane at $t = 160\ \mu s$.

4.1.2 Pressure field

The pressure distribution at $t = 160\ \mu s$ is reported in Figure 4.3, where one can appreciate the strong expansion of the jet, moving from $p_s = 1\ kPa$ (the constant inlet static pressure) to $p_{vacuum} = 1\ mPa$ (the vacuum pressure inside the VV). The jet results mostly to be at very low pressure, because of the high speed values in those regions. The internal energy is predominant at the inlet, while it becomes mainly kinetic in the neighbouring of the shock front [1].

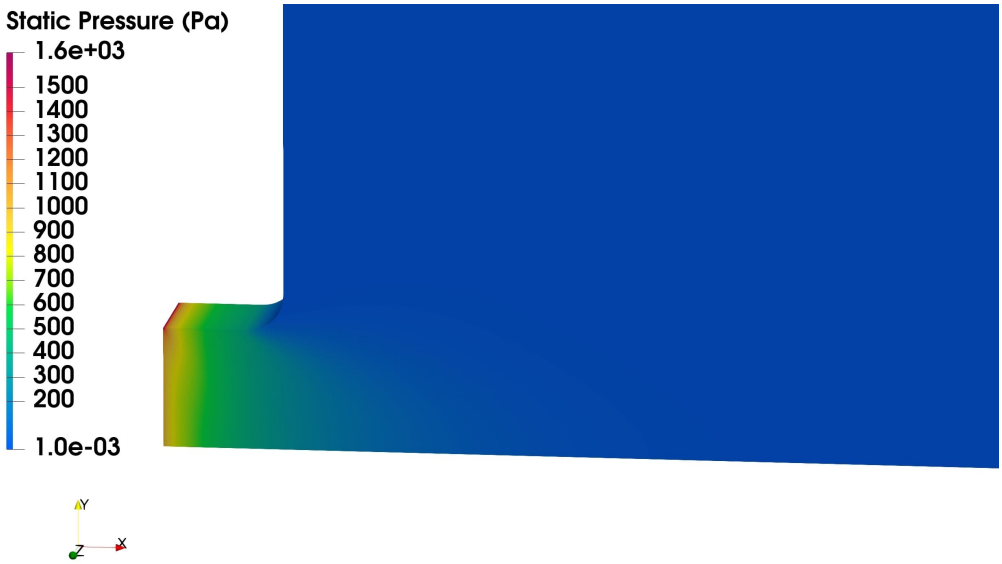

Figure 4.3: Zoom of the static pressure distribution on the vertical plane close to the inlet region at $t = 160\ \mu s$.

4.1.3 Temperature field

The temperature distribution of He at $t = 160\ \mu s$ ms is reported in Figure 4.4. It moves from very high values close to inlet down to very low ones much further away (where the jet is highly expanded).The lowest temperature is registered in correspondence of the discontinuity between the Mach disk and the leading edge (the so called Minimum Temperature Distance - MTD), where the velocity peak occurs. Both temperature and pressure show a similar trend because, as the jet expands, an energy conversion occurs from internal (high pressures, high values) near the inlet to kinetic (high speed) approaching the jet front.
The temperature profile along the jet axis (Figure 4.5) ramps from the inlet, peaking in correspondence of the disk front and progressively reducing in the forward region. Combining 3.2 and 3.3 provides the isentropic relationship reported in 4.2:

$$\frac{p_t}{p_s} = \left(\frac{T_t}{T_s}\right)^{\frac{\gamma}{\gamma-1}} \tag{4.2}$$

which is valid in the jet region, due to the substantial absence of viscous effects [1].

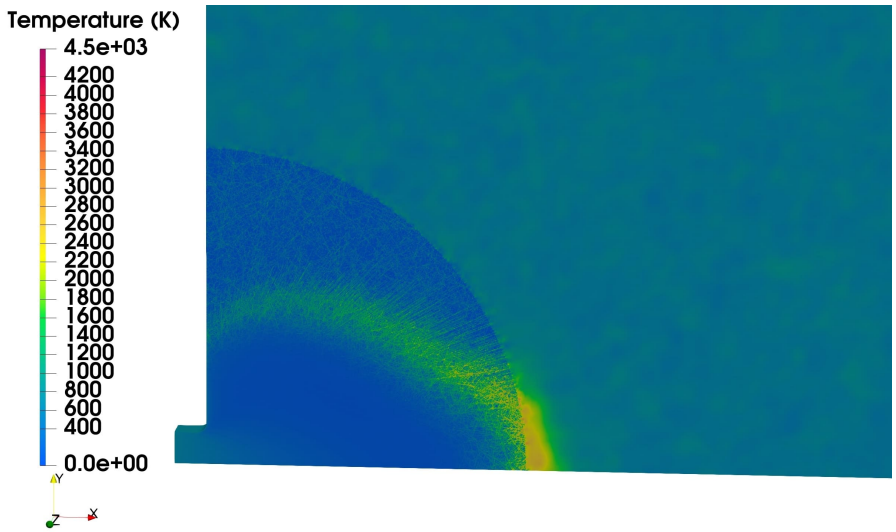

Figure 4.4: Zoom of the temperature distribution on the vertical plane close to the inlet region at $t = 160\ \mu s$.

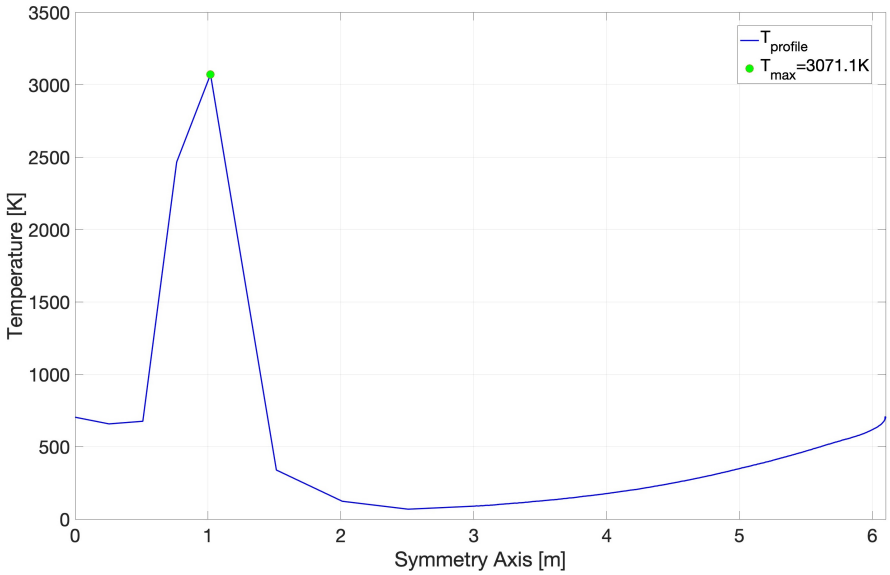

Figure 4.5: Temperature profile along the jet axis at $t = 160\ \mu s$.

Chapter 5

Dynamic mesh refinement

5.1 Kn mapping and domain restriction

5.1.1 Kn mapping

The original CAD described in 3.3 is the one adopted for solving the transient up to 160 μs, time step at which the front of propagation of the Mach disk approximately overcomes the refinement region. At this time, the total number of molecules inside the domain is in the order of $2.481 \cdot 10^{20}$, producing a huge computational effort and, therefore, a significant time spent for moving from one iteration to the following. The main issue is related to the neighbouring inlet region, where the helium molecules are closer one to each other, leading to the validity of the CFD approach based on the NS equations (and so, a high number of small cells is required). Further away, the gas rarefaction is significant, causing the need to switch to a DSMC approach (2) based on the solution of the Boltzmann equation, as described in 3.8. On the other hand, the cells in this part of domain should be larger and in reduced amount respect to the previous region.

A possible solution would be to restrict the study, focusing on the pure DSMC region. In other words, it means to move the domain of interest in the region right after the front of the Mach disk and up to the adiabatic wall in front of it. Due to the fact that the transient requires lots of time steps to completely fill the VV, it seems more interesting to focus only on the downer region of the domain. For this reason, the CAD for the second part of the transient is cut once more and, therefore, the height of the new domain is reduced up to 1/3 of the original one.
In order to to that, it is first needed to identify exactly where the Kn number value (2.1.1) transits from the continuum regime (for $Kn < 0.1$) to the transition one (for $Kn > 0.1$).
As already said in 3.9, ParaView is an open-source post-processing software able to adopt numerous filters that can be applied in cascade for a specific dataset.

By means of this tool, the Kn number map is obtained as in Figure 5.1.

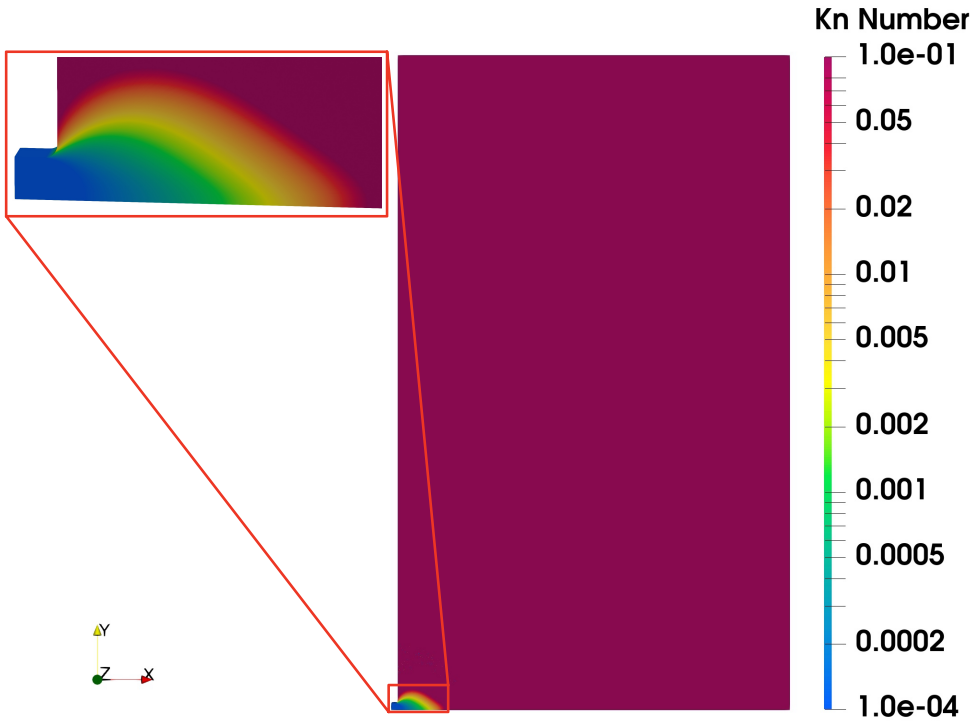

Figure 5.1: Mapping of Kn number on the vertical plane at $t = 160\ \mu s$.

5.1.2 Domain restriction

Once the DSMC region inside the domain is found, it is chosen to draw a cutting ellipse delimiting the pure DSMC surface of interest from the CFD one, as represented in Figure 5.2. This decision is coherent with the front profile of the Mach disk. As a matter of fact, up to this moment the CFD region and the front shape are almost coincident and they are completely contained inside the disk of refinement described in 3.8.1 (look at Figure 5.3).

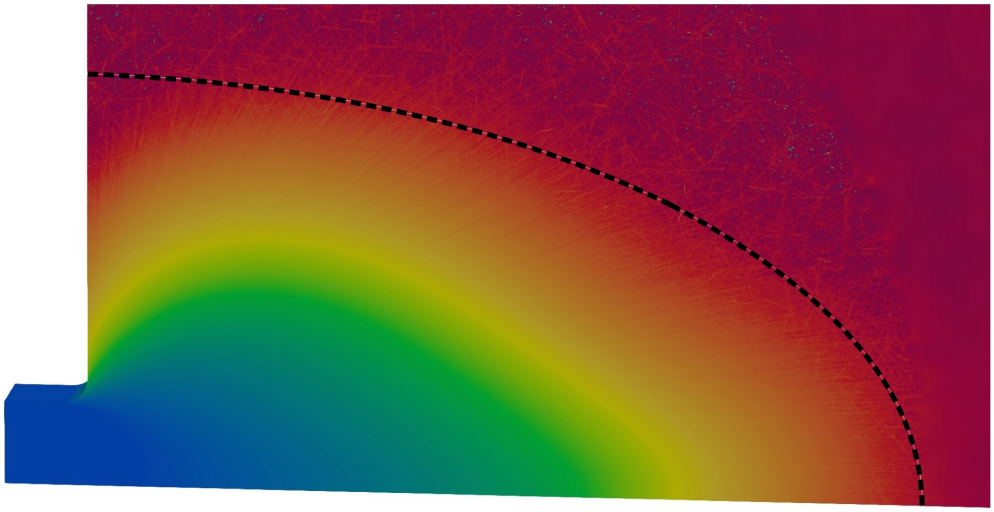

Figure 5.2: Splitting of CFD region from DSMC region at $t = 160\ \mu s$.

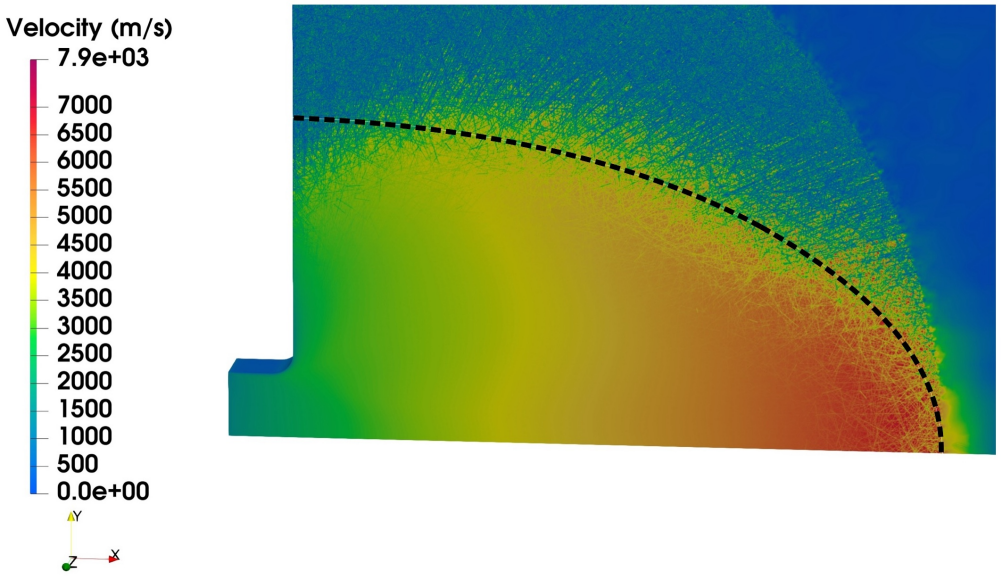

Figure 5.3: Front profile of the Mach disk at $t = 160\ \mu s$.

The new CAD domain with attached boundary conditions is shown in Figure 5.4.

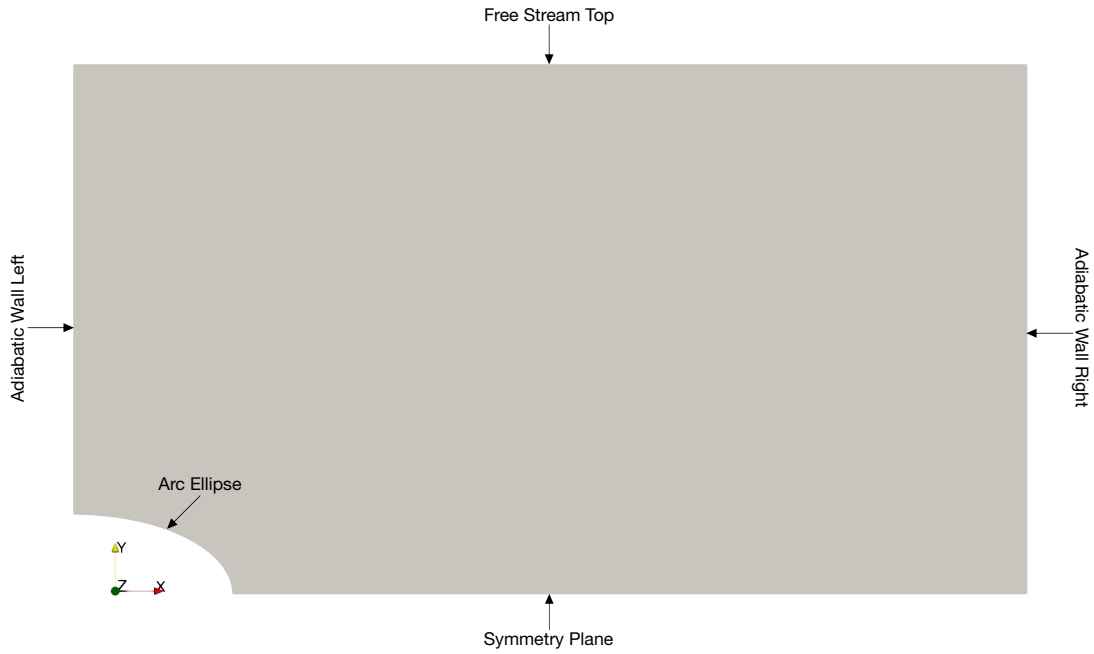

Figure 5.4: Computational domain and boundary conditions of the 2D simulation starting at $t = 160\ \mu s$.

5.2 Simulation setup

The second part 2D transient DSMC simulation is described in this section.

5.2.1 Thermal-hydraulics boundary conditions

Looking at Figure 5.4, the boundary conditions can be characterized as follows:

- **Arc Ellipse**: It represents the new inlet for the domain and it is obtained by interception of the original CAD with the cutting ellipse. Differently from before, the total pressure, the total temperature and the supersonic static pressure are not imposed a priori, but they are a direct output of the first part of the transient.
- **Adiabatic Wall Left**, **Adiabatic Wall Right**: They adopt the classic setting for walls (e.g., no slip, smooth and adiabatic). These boundaries are

shorter than the ones of the original simulation, consequence of the decision of focusing on its downer part.

- **Symmetry Plane**: Taking into account the symmetry in the bottom part of the domain, the "Symmetry Plane" condition is selected for the lower boundary. Also in this case, the length of the boundary is reduced respect to the initial part of the transient because of the cutting plane.

- **Free Stream Top**: This condition is new respect to the original domain. It is mandatory to modify the "wall" condition on the top of the original domain, because the new one is no more closed on the upper part. A good compromise taking into account the physics of the problem in that area is the *freestream* option. It is a hybrid condition coming from the *inletOutlet* condition, but differently from it, the operation modality changes from fixed (free stream) value and zero gradient depending on the flux sign [4].

5.2.2 Initial conditions

It is very difficult to predict in advance the right value of the static pressure at a specific point of the transient. For this reason, this condition is not imposed by hands, but it is a direct output of the first part of the transient.

5.2.3 DSMC Initialization and DSMC properties

It is required to initialise again the equilibrium density of particles in the domain, since the simulation starts at a specific time step where the initial conditions inside the VV are already perturbed and because of the geometry change. By means of 3.5, this value is estimated into approximately $n_{eq} = 1.1663 \cdot 10^{18}\ m^{-3}$.
The initial number of particles inserted inside the domain is $N_{particles} = 195413$, while the particle density close to the inlet of the domain is $n_{in} = 10^{17}\ m^{-3}$. The latter is smaller than the original domain because the inlet is moved forward at a point where the gas is partially expanded.
On the other hand, the helium properties of interest for the simulation listed in 3.2 are still the same.

5.3 Applications and Dictionaries

5.3.1 Applications

The only application implemented for the second part of the transient remains still *dsmcFoam*.

5.3.2 Dictionaries

A new dictionary is add to the ones described in 3.7.2:

- **mapFieldsDict**
  The *mapFields* tool is adopted for mapping one or more fields proper of a given geometry (source) onto the corresponding field for another one (target). It is not needed to satisfy any similarity between the geometries to which the fields relate [4]. If either or both of the source ad target cases are decomposed for running in parallel, it is required to declare a *-parallelSource* and a *-parallelTarget*: the first one specifies that the source case is decomposed for parallel calculation, while the latter specifies that the destination case is decomposed for parallel calculation [59].
  When the geometry similarity is not verified, the fields are *inconsistent* (the geometry and the boundary conditions are not the same between source and target), meaning that it is mandatory to define a *mapFieldsDict* dictionary inside the *system* directory of the target case [4].
  The dictionary syntax contains two lists: *patchMap* and *cuttingPatches*:

  1. **patchMap**
     It lists the mapping of data between pairs of target and source patches geometrically coincident in the two cases. In this particular mapping none of the boundaries of the source and the target remain still the same, because they are either new boundaries (*Arc Ellipse* and *Free Stream Top*) or they are cut respect to the original domain (*Adiabatic Wall Left*, *Adiabatic Wall Right* and *Symmetry Plane*). Each line shows firstly the target patch and right after the source patch (empty for this first mapping).
  2. **cuttingPatches**
     It lists the target patches that have to be mapped from the original internal field (source) now cut by patches (in this specific mapping are indicated the new boundaries *Arc Ellipse* and the *Free Stream Top*). For the cases where the target patch partially cuts the source internal field, those values inside the internal field are mapped, while the ones outside remain unchanged [4].

  The map field data mapped from *mapFields* are the ones within the time directory indicated in *startTime* (in this simulation it is the *latestTime* since it is chosen to start the second part of the transient from the last autosave of the first one) [4].

5.4 Mesh generation

Due to the fact that the new domain under investigation starts beyond the continuum region, the high rarefaction of helium leads to the adoption of a coarser mesh than the original simulation, with the advantage of strongly reducing the computational effort. As before, an uniform fine mesh for the entire domain is not a clever choice. The space discretization involves initially very fine cells near the new elliptic inlet region, which become progressively bigger moving forward.
The required time step in order to follow the shock front propagation is still 83 ns, but the computational time is reduced because of the large cells dimension.

5.4.1 Mesh refinement strategy

Once it is defined the new reference CAD (*surfaceFile*, "new_cad.stl"), the mapping tool described in 5.3.2 was adopted each time the pressure and temperature values change in such a way the actual cell size of the simulation is no more in accordance with the one proposed by 3.5.4.
This choice is not user-friendly, but it has the advantage of tracking the evolution of the Mach disk by using small cells only where needed, leaving a significant part of the domain with a very coarse mesh.

Differently from the first part of the transient, for successive simulations SALOME Platform mesher was taken into account, because of its better performances when choosing an object of refinement user-defined. The adopted 2D tetrahedral meshing tool is NETGEN 1D-2D algorithm, a powerful instrument with a wide spectrum of settings (e.g., maximum and minimum size, growth rate, fitness, etc.) that have to be adjusted in order to reach the best result for a mesh in a specific numerical simulation [50]. In particular, it was enforced the quadrilateral predominance, coherently with the previous *cartesian2DMesh* in cfMesh. The maximum and minimum cell sizes were imposed equal (in order to have an uniform mesh outside the refinement region), while the local sizes were assigned only on the faces of the refinement objects properly designed for the occurrence.

Having in mind the idea of emulating the shape of the velocity front, the most genuine proposal would be to implement elliptic sector areas of finer cells, keeping the regions behind and forward with coarser meshes. The process is not automated, leaving the user the job of adjusting by hands the cell sizes and the position and dimension of the elliptic sector areas. The results look like an AMR (Automatic Mesh Refinement) proper of other CFD tools, but being user-controlled, the correct expression would be *Dynamic Mesh Refinement*.
The first mesh adopted and some of the following are reported in Figure 5.5. As it can be appreciated, the refinement region grows larger during time, since the gas expands inside the domain and the front becomes more dispersed.

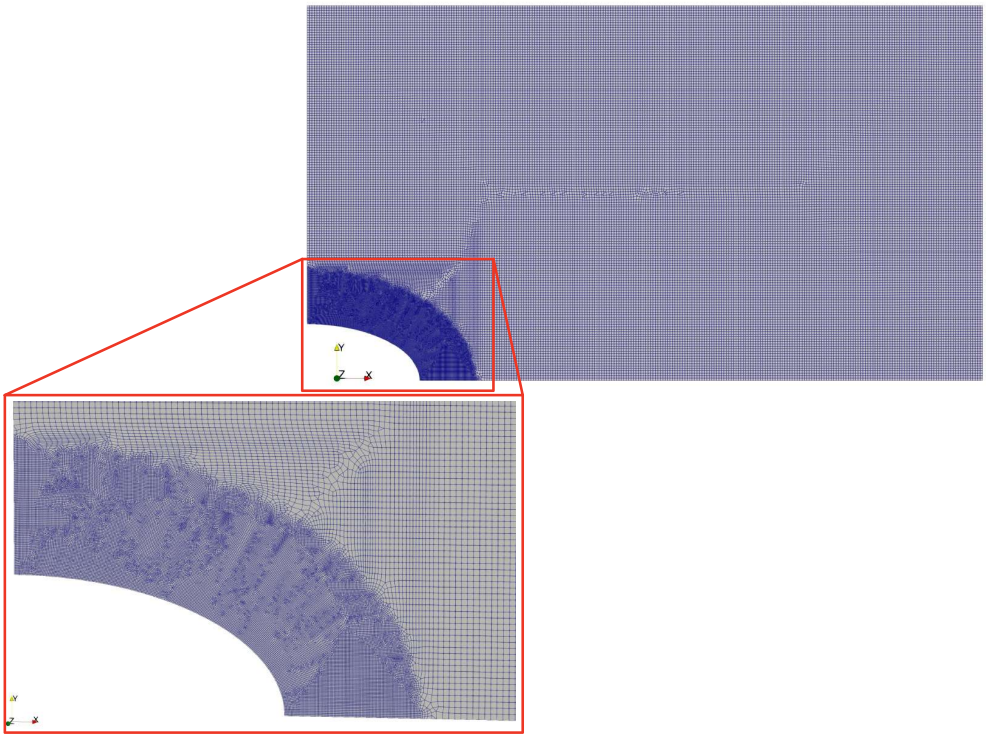

(a) $t = 160\ \mu s$

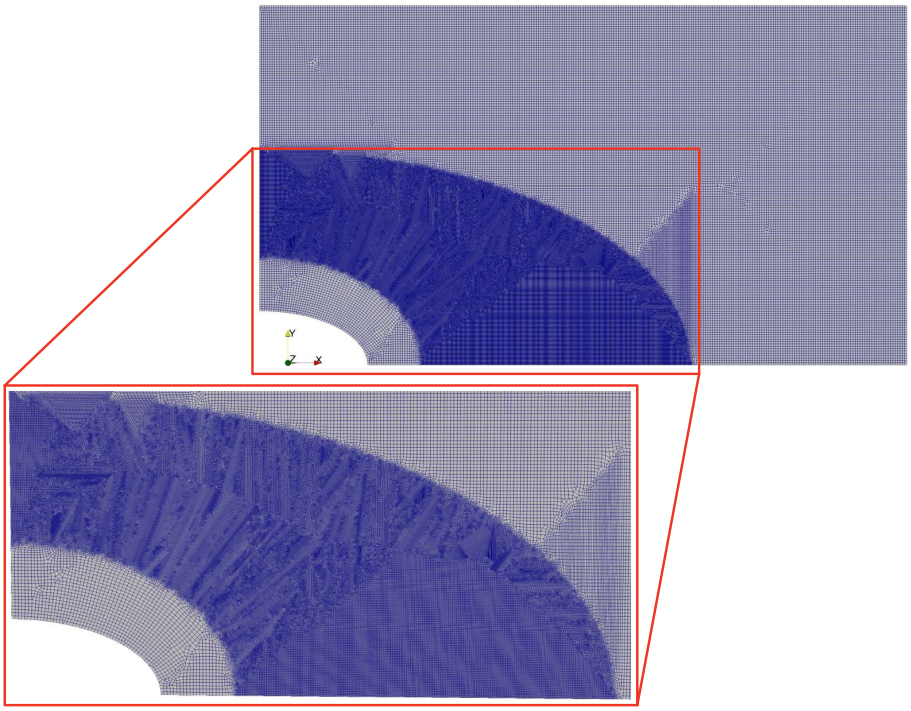

(b) $t = 440\ \mu s$

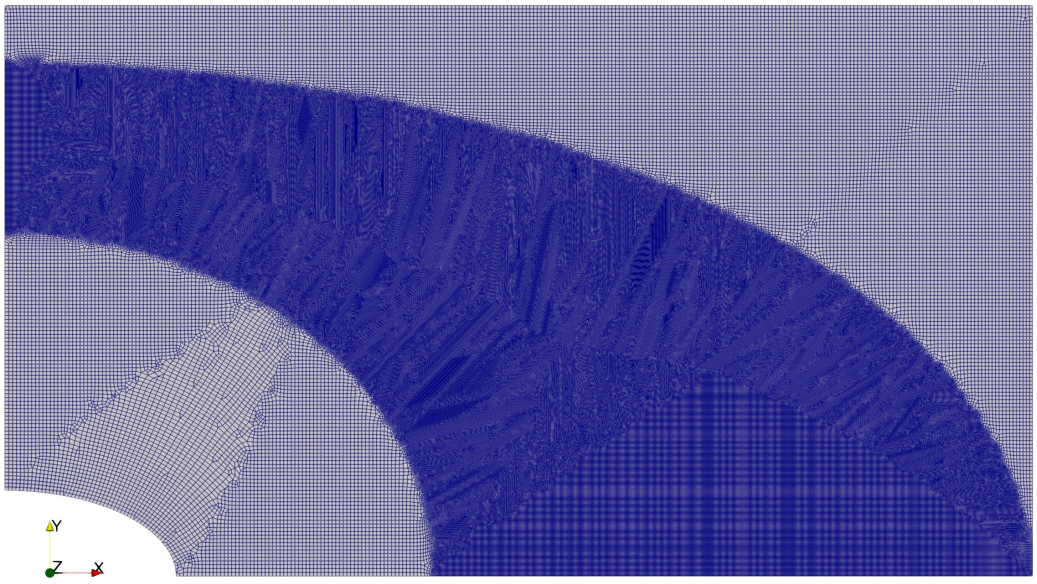

(c) $t = 760\ \mu s$

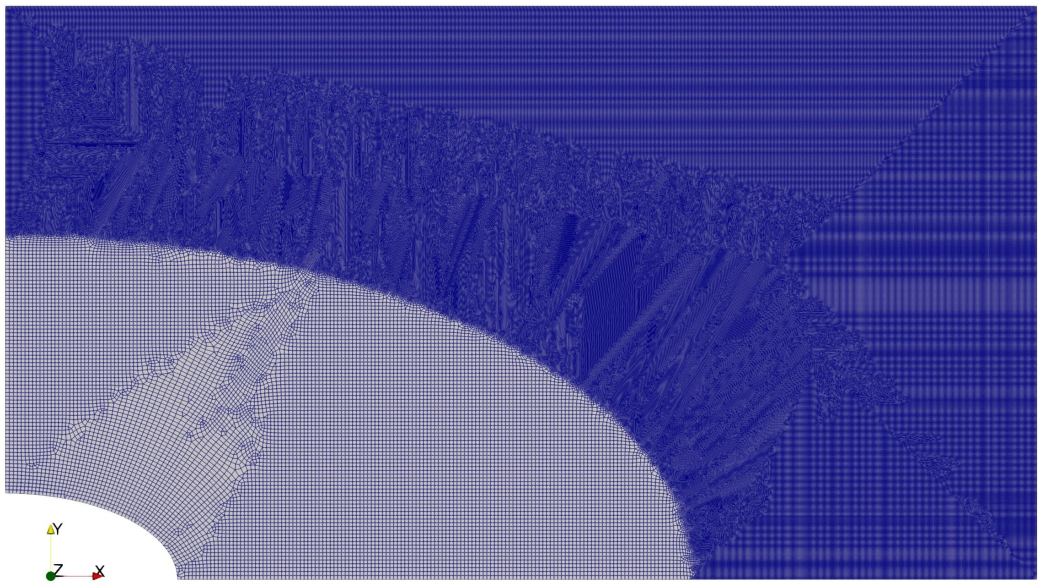

(d) $t = 1\ ms$

Figure 5.5: Dynamic mesh adopted for the second part of the transient.

Chapter 6

Second phase of LOCA

6.1 Results

The second part of the transient starts at $t = 160\ \mu s$, just after the first mapping from the original domain to the reduced one and it is carried out for several ms. The leading shock firstly impacts the right wall of the VV at approximately $t_{contact} = 1\ ms$ (look at Figure 6.1(d)) and causes a sharp pressure peak on this surface (see Figure 6.3). Then, the particles reflected back encounter the Mach disk that was generating and propagating behind.
The domain continues to fill with helium up to $t_{full} = 10\ ms$, when it is saturated. Moving forward, the solution variation which was more evident from one time step the following is now flatter. The time evolution is appreciable up to $t = 20\ ms$. After that time step the solution does not change anymore, leading to a steady-state condition and allowing to declare $t_{end} = 20\ ms$ the end of the simulation.
The solution outputs at six different time instants ($t = 160\ \mu s$, $t = 560\ \mu s$, $t = 760\ \mu s$, $t = 1\ ms$, $t = 10\ ms$ and $t = 20\ ms$) are reported in this section.

6.1.1 Flow field

The outputs for the second part of the jet evolution are reported in Figure 6.1, starting from the first mapping of the solution (Figure 6.1(a)). As it can be observed, the Mach disk front takes a few instants to reach the wall in front of it (look at Figure 6.1(d)). After that, the particle reflection deforms the Mach disk that tries to adapt to the geometry of the VV inboard surface, despite is not able to touch it because of the wall boundary condition (clearly visible at Figure 6.1(e)). Afterwards, the solution characteristic time interval switches from μs to ms, since the evolution of the transient is no more appreciable in short time intervals, but it takes more time.
Once more, the increase of the average pressure in the domain leads to a reduction

of the pressure ratio [1]. This phenomenon can be explained taking into account the position of the new elliptic inlet respect to the flow entrance in the original domain. Being this inlet shifted right after the CFD region, the pressure in this new CAD would be smaller, causing a reduction of the gap with the core of the domain (appreciable in Figure 6.3).

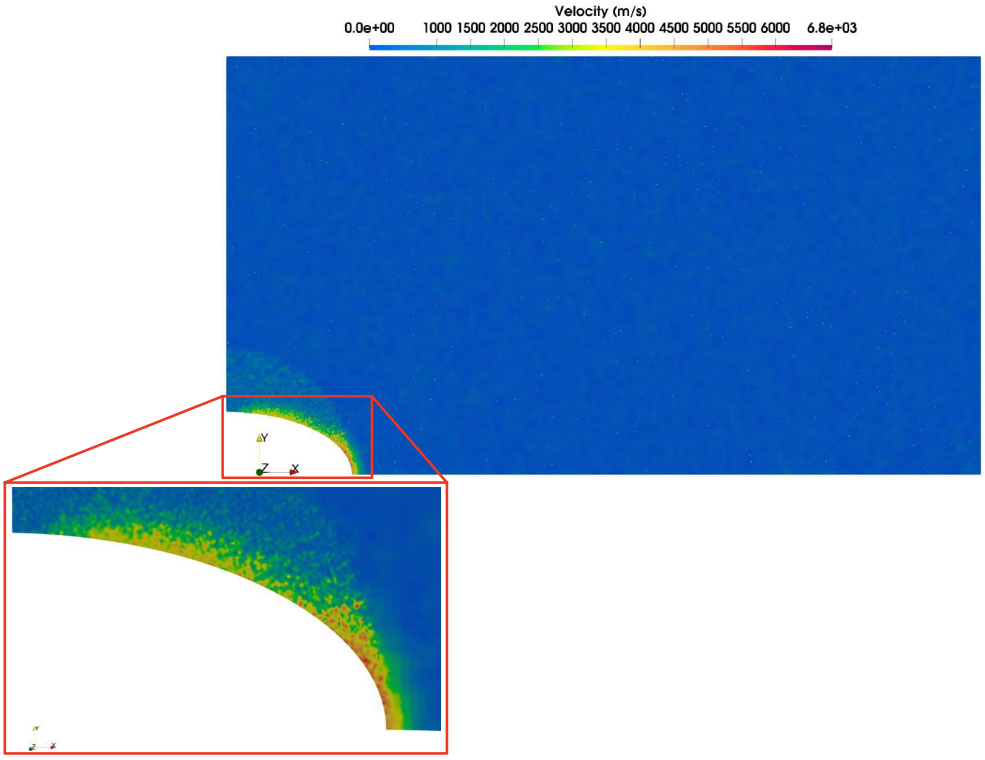

(a) $t = 160\ \mu s$

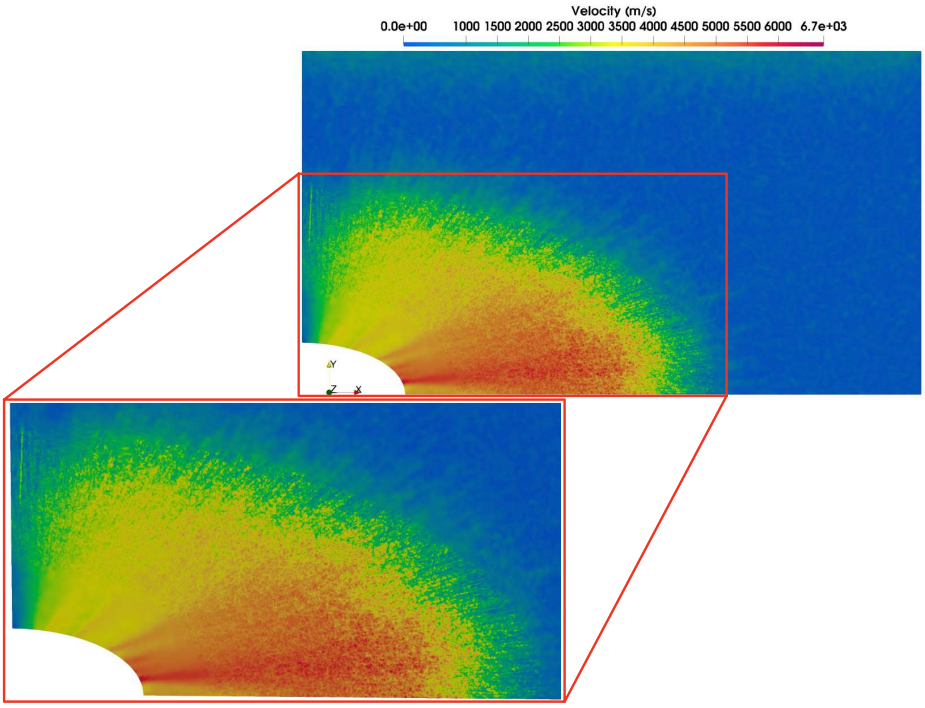

(b) $t = 560\ \mu s$

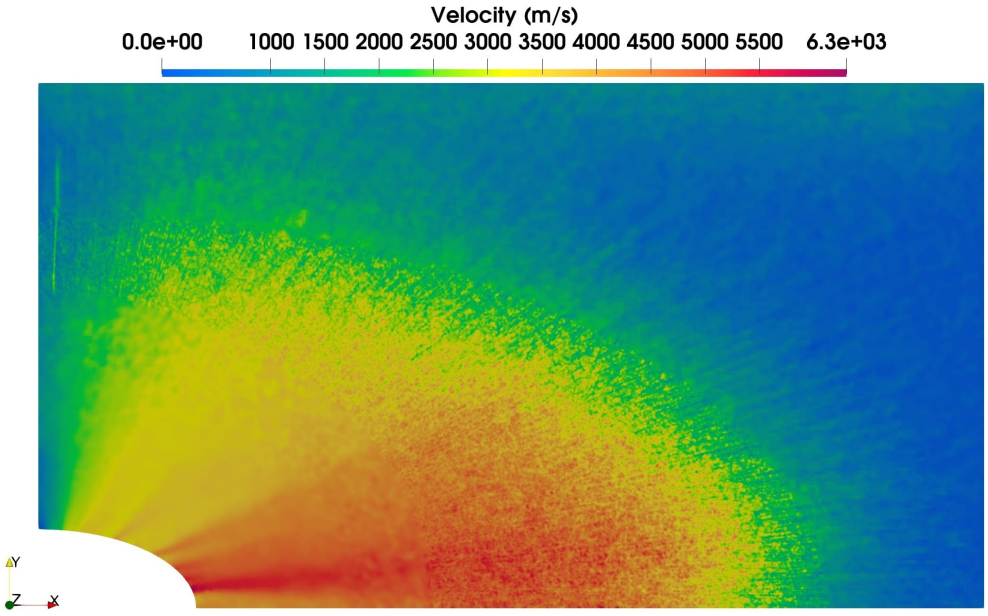

(c) $t = 760\ \mu s$

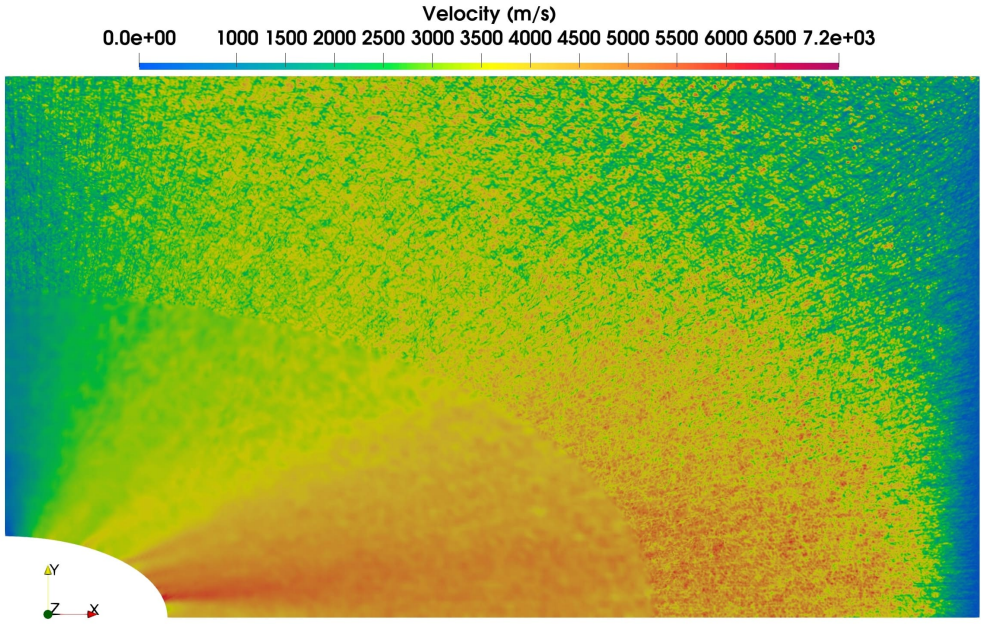

(d) $t = 1\ ms$

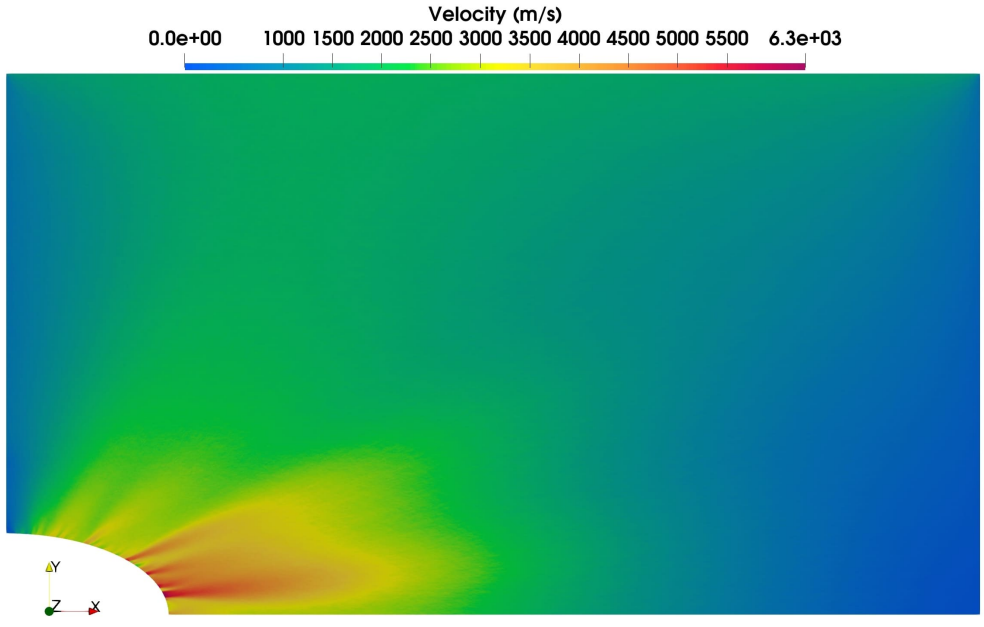

(e) $t = 10\ ms$

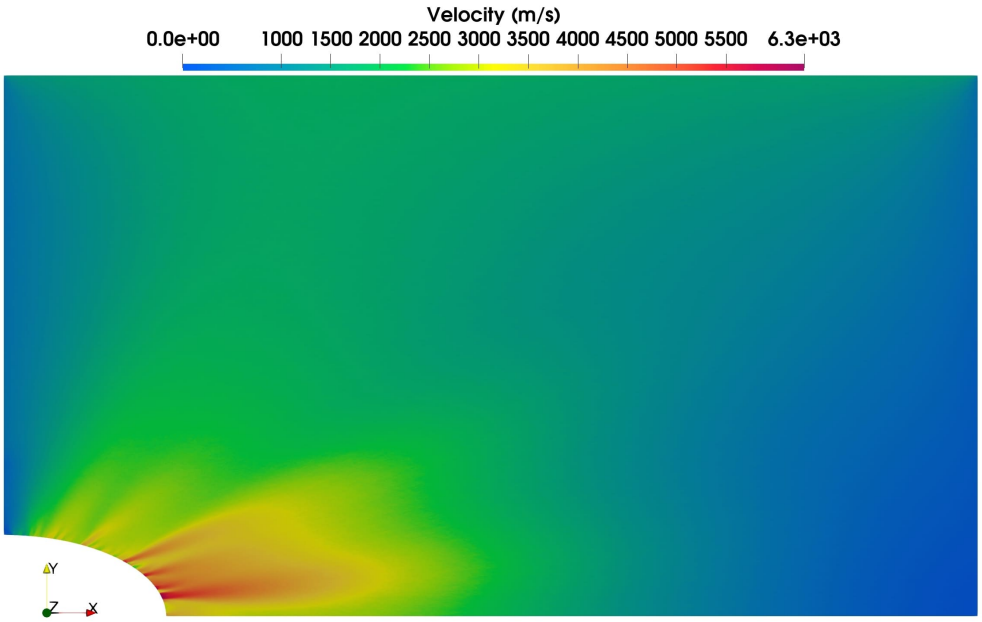

(f) $t = 20\ ms$

Figure 6.1: Evolution of the flow field on the vertical plane.

The average Mach number in the domain (Figure 6.2) is computed as in 4.1.

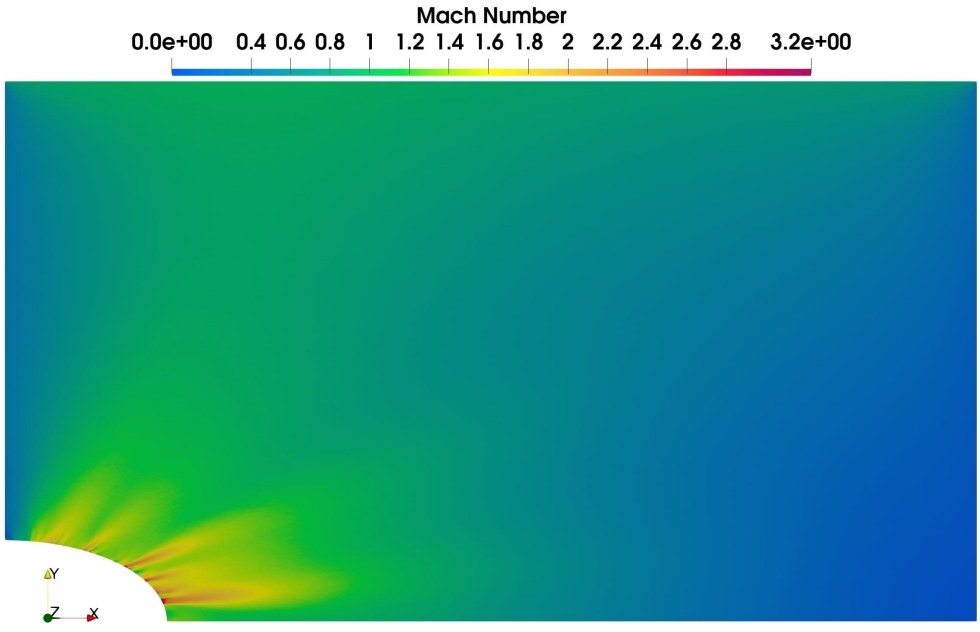

Figure 6.2: Mach number distribution on the vertical plane at $t = 20\ ms$.

6.1.2 Pressure field

The pressure distribution at $t_{end} = 20\ ms$ is reported in Figure 6.3. The jet expansion from the elliptic section leads to smaller peaks than the original simulation, because the new inlet is shifted right after the CFD region. The pressure ranges from $p = 67\ mPa$ (the constant inlet static pressure derived from mapping) down to $p = 1.7\ mPa$ (the pressure inside the VV, completely filled by the helium flow). As before, a very low jet pressure appears as a consequence of the high speed values in those regions. The internal energy is predominant at the elliptic inlet, while it becomes more kinetic in the proximity of the shock front (Figure 6.1(d)) [1]. Afterwards, the energy switches again to kinetic close to the wall.
When the pressure waves transit to a given region, the pressure changes a lot. The weakest points are represented by the walls of the outboard portion of the VV, where are placed some important reactor components (e.g., the interface with the plasma heating devices, including the gyrotron diamond windows) [1]. It is also needed to pay attention to the wall facing the jet front, where the pressure increases a lot because of the particle reflection, as already mentioned in 6.1.1.

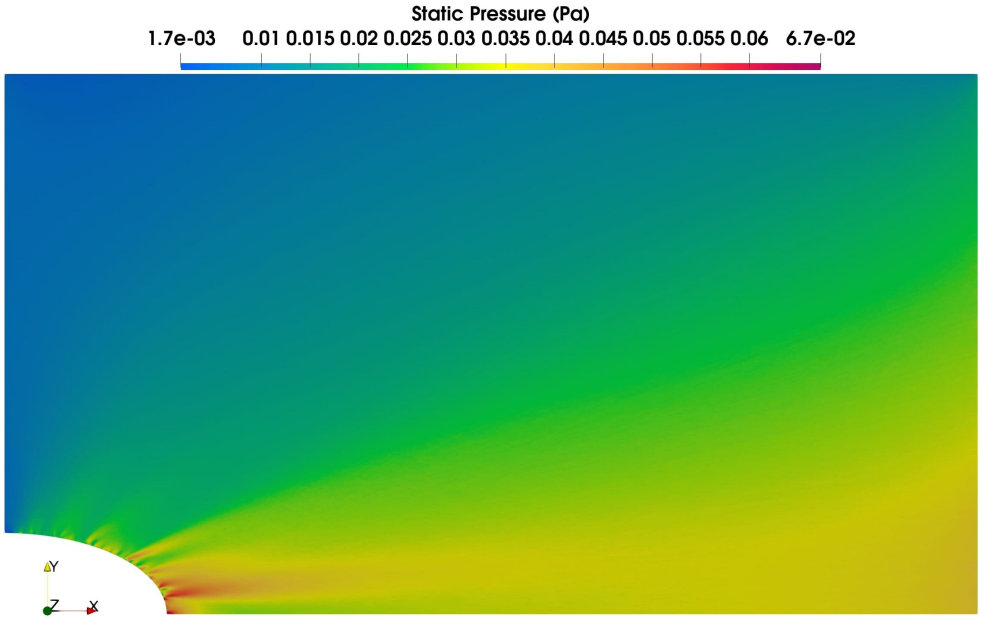

Figure 6.3: Static pressure distribution on the vertical plane at $t = 20\ ms$.

6.1.3 Temperature field

The temperature distribution of He at $t = 20\ ms$ is reported in Figure 6.4. As it is clearly visible, the maximum values are registered in the core of the domain, mainly

in correspondence of the Mach disk front. The lowest temperature is reached in the lowest part of the left boundary, coherently with the propagation of the flow field, mostly directed to the right and to the top part of the model.
Temperature and pressure profiles are slightly different respect to the first part of the transient. Due to the fact that the domain walls are adiabatic, a high temperature region appears in the middle of the domain, while the neighbouring parts remain significantly colder (at approximately ambient temperature). This phenomenon confirms the predominant kinetic energy in the proximity of the shock front, as already mentioned in 6.1.2.
Nevertheless, the temperature outputs for the second part of the transient are not coherent with the expectations. The temperature should be hotter in proximity of the front of the Mach disk, while it has to be colder in the region below. The wrong behavior appearing in Figure 6.4 may be justified on the inefficiency of the domain restrictions for the second part of the simulation. As a matter of fact, the expected temperature distribution is partly appreciable in the first instants of the transient evolution (Figure 4.4), where it was taken into account the entire domain for the accidental scenario.

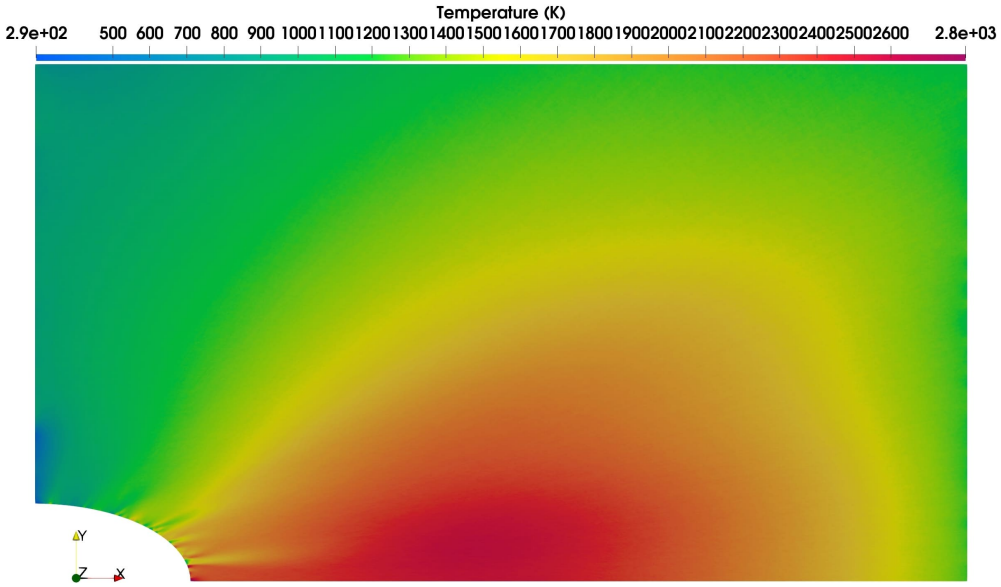

Figure 6.4: Temperature distribution on the vertical plane at $t = 20\ ms$.

6.1.4 Kn field

Once the velocity, pressure and temperature fields have been critically analyzed, it is important to focus on the Kn field, in order to establish if the domain is still in

the DSMC range of Kn number or whether the transient has evolved is such a way the CFD approach would be valid partially or totally in some places.
The evolution of the Kn map (look at Figure 6.5) shows that, as the transient evolves, the pressure of He inside the domain (and so the particle density) increases, causing a reduction of the Kn values of 2 orders of magnitude (see Figure 6.5(f)). Nevertheless, the Kn range does not fall below the CFD lower bound $Kn < 0.1$. This phenomenon can be explained taking into account the fact that the pressure in the original inlet was in the order of $p_{in} = 1\ kPa$, so that the pressurization of the VV does not occur in a dramatic way.

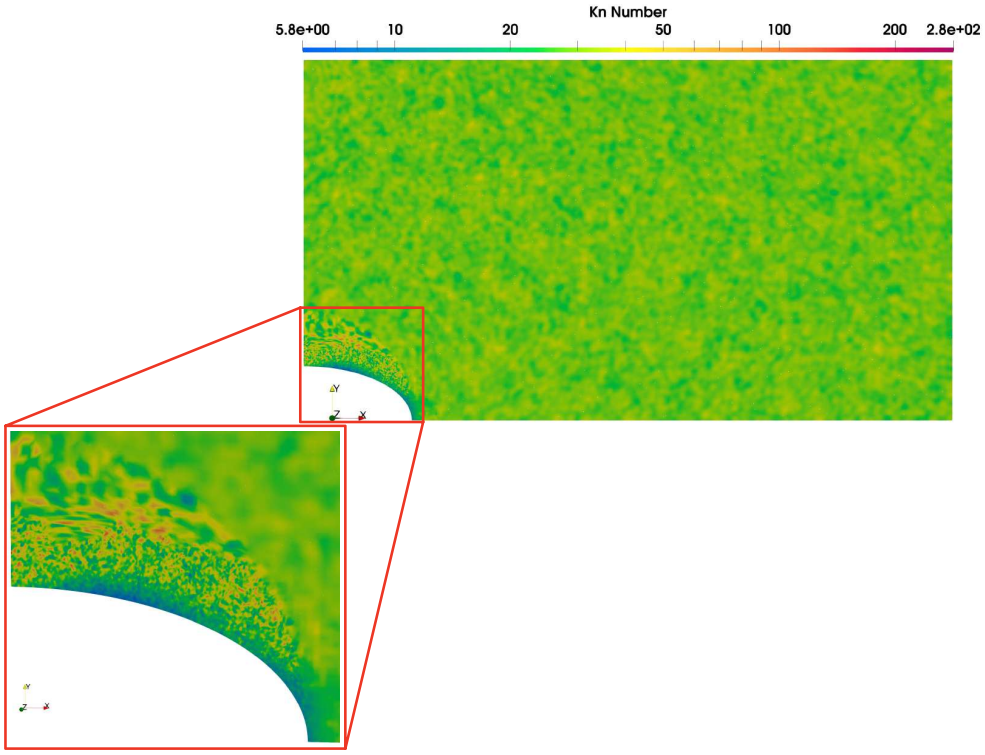

(a) $t = 160\ \mu s$

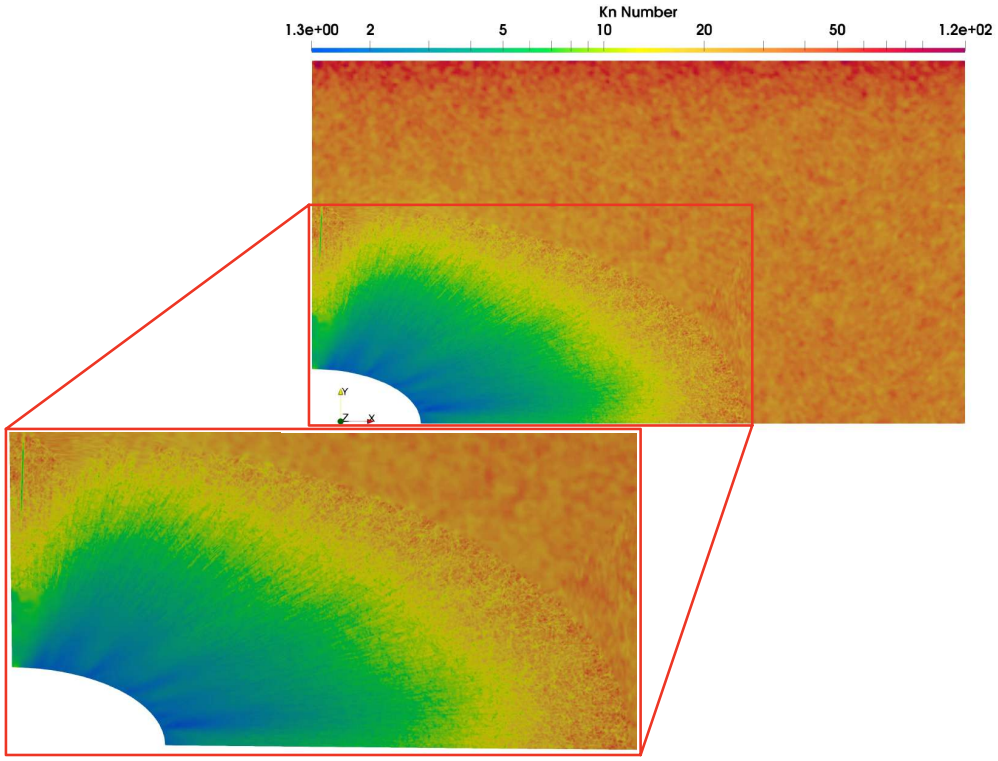

(b) $t = 560\ \mu s$

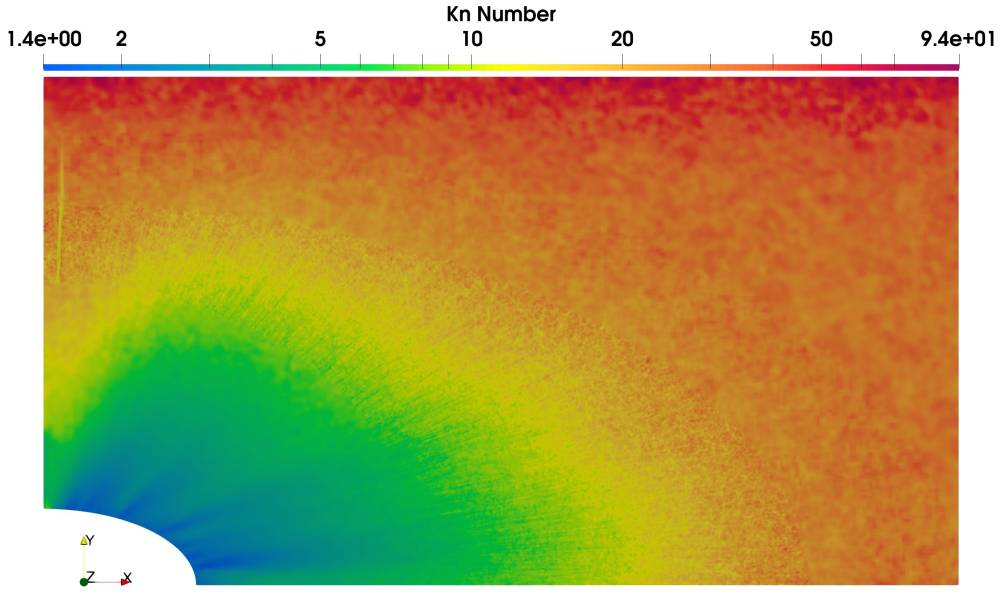

(c) $t = 760\ \mu s$

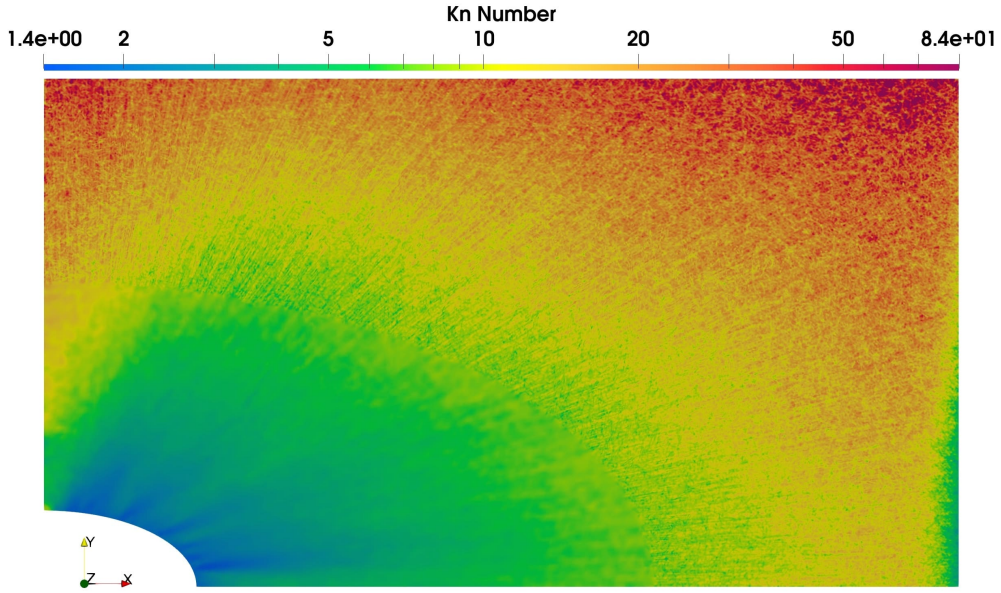

(d) $t = 1\ ms$

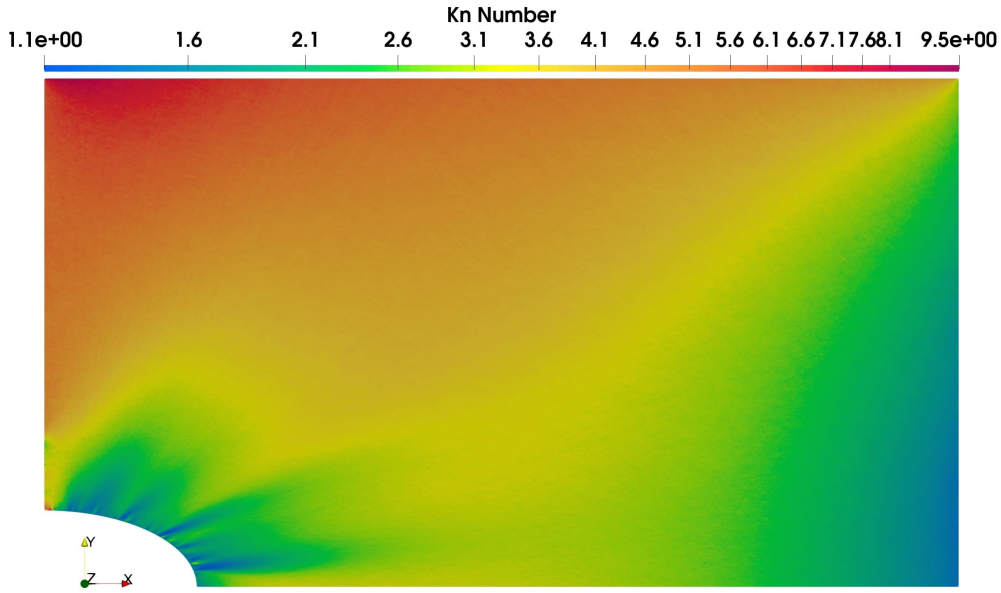

(e) $t = 10\ ms$

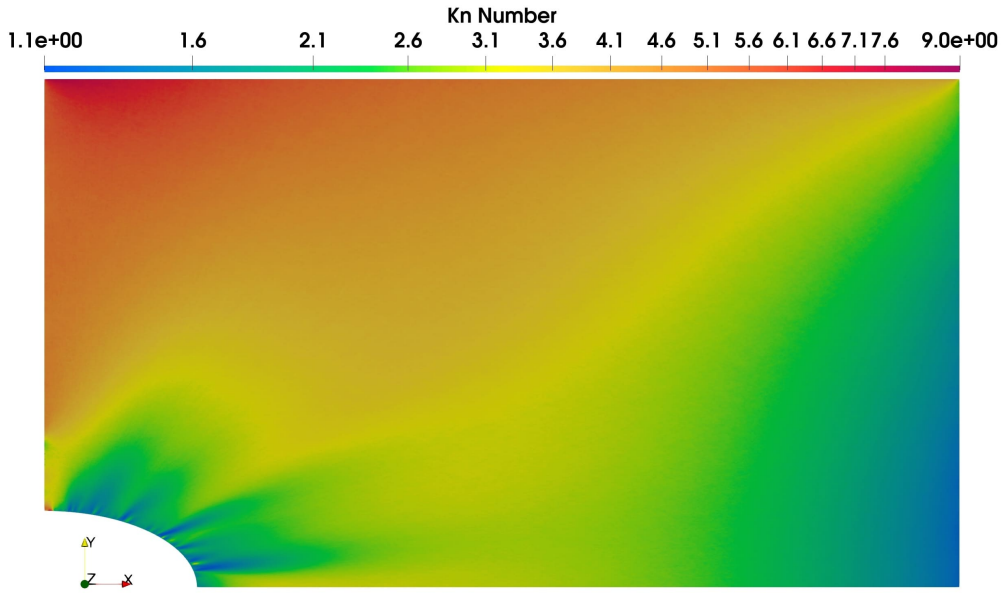

(f) $t = 20\ ms$

Figure 6.5: Evolution of the Kn field on the vertical plane.

Chapter 7

Comparison with CFD analysis of a LOCA from a HCPB blanket in the EU DEMO VV

In this thesis a DSMC analysis of a LOCA from the HCPB blanket in the EU DEMO VV has been carried out. In order to declare whether the results are physically acceptable, it should be interesting to look at other similar computational models (e.g., CFD approaches for the problem under investigation).

In particular, the plots are compared with the proposal of A. Zappatore et al. in [1], studying an in-VV LOCA. Despite in that paper was performed a CFD analysis for a 3D LOCA transient for a HCPB blanket design, the difficulty into recovering in literature similar models making use of DSMC method makes this choice the best compromise. This chapter has the aim of critically analyzing the main differences between the two simulations in order to establish which one causes the most severe consequences.

One of the most significant differences are the physical properties of the employed coolant, because in [1] the authors adopted pressurized He at operating conditions of $p_{in} = 8\ MPa$ and inlet temperature of $T_{in} = 683.15\ K$. In principle, in the DSMC simulation of this thesis it was tried to implement higher pressures. However, being the pressure linked to the grid side, the implementation of gases with a small degree of rarefaction leads to the need of generating a very fine mesh (look at 3.5.4). This fact increases strongly the computational effort, causing the need of spending a very long time for moving from one time step to the following.

In the DSMC simulation (look at Figure 7.2), the jet shows a predominant axial direction of propagation, because of the much higher velocity respect to the CFD proposal (see Figure 7.1), causing the need of dissipating less energy.

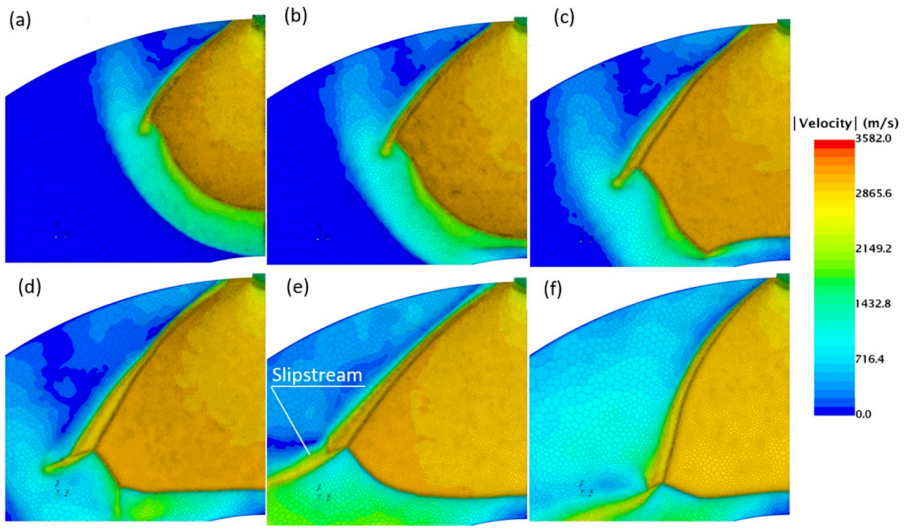

Figure 7.1: Evolution of the flow field before and right after the first impact with the inboard wall on the equatorial plane (symmetry plane) at (a) $t = 2.2\ ms$, (b) $t = 2.6\ ms$, (c) $t = 3.2\ ms$, (d) $t = 4.0\ ms$, (e) $t = 7.0\ ms$ and (f) $t = 9.8\ ms$. Courtesy of [1]

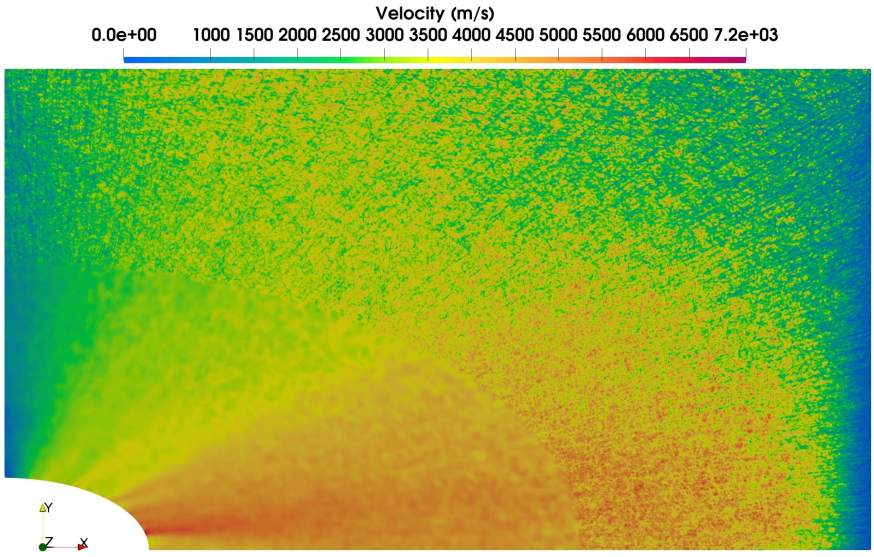

Figure 7.2: Flow field on the vertical plane at $t = 1\ ms$.

Furthermore, in the DSMC simulation the leading edge spends approximately $t_{contact} = 1\ ms$ to reach the facing wall, while in the CFD approach were spent less than 2.5 ms. The wall impact differs in the two cases: in the simulation of A. Zappatore et al. the helium jet with high energy content leads to a pressure rising from 10 kPa to 350 kPa, while in the problem of this thesis the pressure increases up to approximately 35 mPa.
As already said in 6.1.1, the impact of the He flow with the right wall of the domain produces a reflected wave that, in both transients it has not a such high energy content able to compress the Mach disk. As a matter of fact, the wave cannot reach the outboard wall.

From the point of view of the temperature field, the CFD and the DSMC transients show an almost similar behavior. The temperature does not change along the entering pipe. Then, it falls along the front of the Mach disk. However, at the end of the DSMC simulation, the core temperature of the Mach disk shows very astonish temperatures respect to the ambient one of the CFD model. Once more, the temperature ranges are quite different: in the CFD proposal, the temperature belongs in the interval between 30 K and 1500 K, while in the DSMC case the scale is strongly shifted upward, from 290 K to 2800 K.

For what concerns the time scales involved, different behaviors are registered. In the CFD transient were taken approximately 20 ms by the leading shock to reach the BDs, producing an almost immediate pressure increase up to 250 kPa. Moreover, the upper bound of 150 kPa (able to cause the opening of the BDs) is reached in 53 ms, as a consequence of the increase of the average pressure in the VV. On the other hand, the DSMC transient spends roughly $t_{full} = 10\ ms$ to completely fill the domain, while it needs up to $t_{end} = 20\ ms$ to reach a steady-state condition at an average pressure in the order of mPa.

Chapter 8

Conclusions

In this thesis, a 2D DSMC model of an in-VV LOCA developing from a break in the HCPB blanket of the EU DEMO reactor has been analyzed. The most important goal was to verify how much time is required for completely filling the VV and if the average Kn number on the domain remains still in the DSMC range or whether it falls locally in the CFD interval. Some considerations about the thermo-mechanical behavior of the reactor walls were provided.

The such defined model is able to track the evolution of the He flow when it enters in the plasma chamber as well as the derived shock waves. Differently from a lumped model, it is capable to predict in advance the behavior of localized quantities (e.g., the pressure peaks in the domain).
By means of the mapping tool in OpenFOAM [4], it was possible to make a well use of the dynamic mesh refinement, in order to reduce as much as possible the computational effort. Thanks to this choice, small cells were used only where needed (the front of the Mach disk), leaving an important part of the domain with a coarser mesh.

As the transient proceeds, the He jet reaches the facing wall (the region where the BDs are placed) and hits this surface at $t_{contact} = 1\ ms$. The consequences are not so dramatic, because of the huge amount of energy lost by the pressure waves in the travel up to the right wall boundary. The simulation takes approximately $t_{end} = 20\ ms$ to reach a steady-state condition at a pressure peak in the order of mPa, much lower than the design limits and so, it does not represent a critical issue from the thermo-mechanical viewpoint. The such small pressures reached are not able to push the map of the Kn number to the CFD range in all of the domain, except for those regions close to the inlet, where the particle density is higher.

Despite the mapping procedure adopted in the second part of the transient was a useful tool for reducing the computational effort when switching from a bigger to a smaller CAD, some issues appear in the final outputs. In particular, the temperature field seems to be not so much coherent with the expectations, because

of a colder region in proximity of the front of the Mach disk and a hotter region developed below. On the other hand, the flow field shows a more physical behavior, with the characteristic evolution of the Mach disk. This phenomenon suggests that some properties are not correctly preserved when mapping the temperature field. If a high amount of computational resources were available to the user, a possible solution would be to keep the entire domain for all the accident evolution. However, the drawback would be of spending much more time to move from one iteration to the following one, because of the progressive rising amount of particles inserted in the domain. This condition leads to a larger CFD region in the neighbouring of the inlet to be solved at each time step as the simulation proceeds, with a not negligible computational effort.

In the end of this thesis, a comparison with a CFD analysis of an in-VV LOCA originating from a break in the HCPB blanket of the EU DEMO has been carried out. It was demonstrated that the CFD transient is slower than the the DSMC proposal and the hypersonic velocities involved are much higher in the latter.

Appendix A

DSMC setup

```
%% User defined parameters
TT = 683.15; % [K], temperature of Helium at Inlet
LL = 3;      % [m], characteristic length of the system
             % (distance between the Inlet and the Wall
             % in front of it)
MAXF = 1E12; % Maximum allowable value for the scaling
             % factor (i.e. number of physical molecules
             % for each computational molecule)

%% Constants
kb = 1.3806E-23;     % [J/K]
ref_mass = 6.65E-27; % [kg]

%% Properties of He
% Van Der Waals radius and diameter
% (ref: www.periodictable.com)
r_vdw = 140E-12;  % [m]
d_vdw = 2*r_vdw;  % [m]

% Atomic mass
PM = 4.002602*1e-3; %[a.m.u]
mass = PM*ref_mass;

pp = 1e3; % [Pa]

% Equilibrium density
```

```
n_eq=pp/kb/TT;

%% Kinetic theory parameters
% Mean free path (kinetic definition using dvdw)
mfp = 1/sqrt(2)/pi/(d_vdw^2)/n_eq;

% Mean molecular speed
c_mean=sqrt(3*kb*TT/mass);

% Mean collision time
tau=mfp/c_mean;

% Knudsen number
Kn=mfp/LL;

% Determine the regime
if Kn<0.001
    regime="Continuum";
elseif Kn>=0.001 && Kn<0.1
    regime="Slip";
elseif Kn>=0.1 && Kn<10
    regime="Transition";
elseif Kn>=10
    regime="Free molecular";
end

%% DSMC parameters
NPC = 7;              % Number of DSMC particles per cell
                      % (recommendation by Z. X. Sun et
                      % al., Computers and Fluids, 2011)
lengthchar = mfp/3; % Set characteristic grid length as
                      % 1/3 of mfp
deltaT = tau/10;      % Set deltaT as 1/10 of mean
                      % collision time

% Note: it can be proved that the two definitions are
% consistent if a maximum CFL number of 0.3 is allowed

% Scaling factor
% (i.e. # of physical particles per DSMC particle)
f = (lengthchar^2)*n_eq/NPC;
```

```
% Following recommendations, do not exceed 1E8
% But keep track of the adjustment
adj = "NOT adjusted";

if f>MAXF
    % First act on NPC
    NPC = 50;

    % Recompute f
    f_noadj = f;
    f = (lengthchar^2)*n_eq/NPC;
    f_firstadj = f;
    adj = "adjusted once";
end

% Following recommendations, do not exceed 1E8,
% this time act on grid size
if f>MAXF
    f_firstadj = f;
    f = MAXF;

    % Modify cell length to obtain a good f
    lengthchar_firstadj = lengthchar;
    lengthchar = sqrt(f*NPC/n_eq);
    adj = "adjusted twice";
end
```

Appendix B

HPC@POLITO

HPC (High Performance Computers) project at Politecnico di Torino is an Academic Computing Center. It provides computing resources and technical support for academic research activities and students [60]. It consists of three integrated clusters: CASPER (Cluster Appliance for Scientific Parallel Execution and Rendering), HACTAR and LEGION. For this thesis, the last twos were adopted for generating the mesh (as described in 3.8) and performing the simulation of accident (as reported in 3.5). Their features are reported in Figure B.1 and in Figure B.2:

Architettura	Cluster Linux Infiniband-QDR MIMD Distributed Shared-Memory
Interconnessione nodi	Infiniband QDR 40 Gb/s
Rete di servizio	Ethernet 1 Gb/s
Modello CPU	2x Xeon E5-2680 v3 2.50 GHz (turbo 3.3 GHz) 12 cores
Nodo GPU	2x Tesla K40 - 12 GB - 2880 cuda cores
Performance	20.1 TFLOPS (giugno 2018)
Core computazionali	696
Numbero di nodi	29
Memoria RAM totale	3.7 TB DDR4 REGISTERED ECC
OS	CentOS 7.6 - OpenHPC 1.3.8.1
Scheduler	SLURM 18.08

Figure B.1: HACTAR technical features, reproduced from [60].

Architettura	Cluster Linux Infiniband-EDR MIMD Distributed Shared-Memory
Interconnessione nodi	Infiniband EDR 100 Gb/s
Rete di servizio	Ethernet 1 Gb/s
Modello CPU	2x Intel Xeon Scalable Processors Gold 6130 2.10 GHz 16 cores
Nodo GPU	24x nVidia Tesla V100 SXM2 - 32 GB - 5120 cuda cores
Performance	90 TFLOPS (luglio 2020)
Core computazionali	1824
Numbero di nodi	57
Memoria RAM totale	22 TB DDR4 REGISTERED ECC
OS	CentOS 7.6 - OpenHPC 1.3.8.1
Scheduler	SLURM 18.08

Figure B.2: LEGION technical features, reproduced from [60].

LEGION is an InfiniBand cluster composed of 57 computational nodes, each one containing 32 core Intel Scalable Processors Gold and 384 GB of RAM. All the nodes are interconnected from an InfiniBand EDR web and an Ethernet connection. All the users can access by an appropriate login node [60].

HACTAR is an InfiniBand cluster made of 29 computational nodes, each one equipped with 24 core Intel XEON v3 and 128 GB of RAM. All the nodes are interconnected from an InfiniBand QDR web annd an Ethernet connection. Also in this case, the users can access by an appropriate login node [60].

Bibliography

[1] A. Zappatore, A. Froio, G.A. Spagnuolo, and R.Zanino. «3D transient CFD simulation of an in-vessel loss-of-coolant accident in the EU DEMO fusion reactor». In: (Sept. 2020). DOI: 10.1088/1741-4326/abac6b. URL: https://iopscience.iop.org/article/10.1088/1741-4326/abac6b/meta (cit. on pp. i, 22, 42, 47, 55, 58, 59, 70, 74, 80, 81).

[2] A. Zappatore, A. Froio, R. Zanino, G.A. Spagnuolo, S. Ciattaglia, C. Bachmann, and G. Federici. «Design and analysis of the VVPSS tank and connection to the VV incl. upper port». In: (July 2020) (cit. on p. i).

[3] M. Sprò. «3D transient CFD simulation of an in-vessel loss-of-coolant accident in the EU DEMO WCLL breeding blanket». Master thesis. July 2023. URL: http://webthesis.biblio.polito.it/id/eprint/27382 (cit. on pp. i, 9, 19, 20, 22, 23, 42, 44).

[4] C. Greenshields. *OpenFOAM v11 User Guide*. London, UK: The OpenFOAM Foundation, 2023. URL: https://doc.cfd.direct/openfoam/user-guide-v11 (cit. on pp. i, 45, 50, 51, 64, 65, 83).

[5] D. Moiraf. «The use of Plasma Mirror for Relativistic Electron Generation Relevant to Fast Ignition in Inertial Confinement Fusion». PhD thesis. July 2020. URL: https://www.researchgate.net/publication/347530668_The_use_of_Plasma_Mirror_for_Relativistic_Electron_Generation_Relevant_to_Fast_Ignition_in_Inertial_Confinement_Fusion (cit. on p. 2).

[6] Consorzio RFX.org. *La fisica del Tokamak – la centrale a fusione*. URL: https://www.igi.cnr.it/ricerca/magnetic-confinement-research-in-padova/la-fisica-del-tokamak-la-centrale-a-fusione/ (cit. on p. 2).

[7] Energy Encyclopedia.com. *Lawson criterion*. URL: https://www.energyencyclopedia.com/en/nuclear-fusion/thermonuclear-fusion/lawson-criterion (cit. on p. 3).

[8] warwick.ac.uk. *Physics of fusion power - Lecture 2: Lawson criterion / some plasma physics*. URL: https://warwick.ac.uk/fac/sci/physics/research/cfsa/people/pastmembers/peeters/teaching/lecture2.pdf (cit. on p. 3).

[9] B. Harack. *Derivation of Lawson Criterion for D-T*. Vision of Earth.org. URL: https://www.visionofearth.org/wp-content/uploads/2010/11/LawsonCriterion.pdf (cit. on p. 3).

[10] R. Zanino. «Nuclear fusion reactor engineering». In: (Mar. 2023). URL: www.nemo.polito.it (cit. on pp. 3, 4).

[11] wikipedia.org. *Tokamak*. URL: https://it.wikipedia.org/wiki/Tokamak (cit. on p. 5).

[12] iter.org. *What is a Tokamak?* URL: https://www.iter.org/mach/Tokamak (cit. on p. 5).

[13] EUROfusion.org. *Scheme of the magnetic fields inside a Tokamak*. URL: https://euro-fusion.org (cit. on p. 6).

[14] iter.org. *VACUUM VESSEL*. URL: https://www.iter.org/mach/VacuumVessel (cit. on p. 6).

[15] Energy Encyclopedia.com. *Vacuum chamber*. URL: https://www.energyencyclopedia.com/en/nuclear-fusion/tokamaks/vacuum-chamber (cit. on p. 7).

[16] A. Froio, A. Bertinetti, A. Del Nervo, and L. Savoldi. «Hybrid 1D + 2D Modelling for the Assessment of the Heat Transfer in the EU DEMO Water-Cooled Lithium-Lead Manifolds». In: *Energies* 13 (July 2020). DOI: 10.3390/en13143525. URL: https://www.researchgate.net/publication/342798643_Hybrid_1D_2D_Modelling_for_the_Assessment_of_the_Heat_Transfer_in_the_EU_DEMO_Water-Cooled_Lithium-Lead_Manifolds (cit. on p. 7).

[17] EUROfusion.org. *What is a lithium blanket and how does it work?* URL: https://euro-fusion.org/faq/what-is-a-lithium-blanket-and-how-does-it-work/ (cit. on p. 7).

[18] Colin. *Fusion Reactor: Blanket*. Fusion Energy. URL: https://medium.com/fusion-energy/reactor-component-blanket-48dd47e309b5 (cit. on p. 8).

[19] iter.org. *Tritium Breeding*. URL: https://www.iter.org/mach/TritiumBreeding (cit. on p. 8).

[20] A. Froio. «CHALLENGE B: Extracting the power deposited in the blanket by the neutrons, while breeding the tritium fuel (and shielding)». In: (Mar. 2023). URL: www.nemo.polito.it (cit. on pp. 9, 11, 12).

[21] W.R. Meier. «Tritium Breeding Blanket for a Commercial Fusion Power Plant -A System Engineering Assessment». In: (Apr. 2014). DOI: https://doi.org/10.2172/1305833. URL: https://www.osti.gov/servlets/purl/1305833 (cit. on p. 9).

[22] G. Zhou, F.A. Hernández, P. Pereslavtsev, B. Kiss, A. Retheesh, L. Maqueda, and J.H. Park. «The European DEMO HCPB Breeding Blanket: Design Status at the Conclusion of Pre-Concept Design Phase». In: (June 2023). DOI: 10.20944/preprints202304.1098.v2. URL: https://www.preprints.org/manuscript/202304.1098/v2 (cit. on pp. 10, 13).

[23] G. Zhou and F.A. Hernández. «DEMO Breeding Blanket Concepts in EUROfusion - Work Package Breeding Blanket (WPBB)». In: (Oct. 2021). URL: https://www.google.it/url?sa=t&rct=j&q=&esrc=s&source=web&cd=&ved=2ahUKEwi18820mPKBAxX6hP0HHTYpA7QQFnoECBMQAQ&url=https%3A%2F%2Fpublikationen.bibliothek.kit.edu%2F1000139517%2F130933090&usg=AOvVaw19I0cY4JwtyWpHTGSTgoxW&opi=89978449 (cit. on pp. 10, 13–15).

[24] wikipedia.org. *DEMO*. URL: https://it.wikipedia.org/wiki/DEMO (cit. on p. 15).

[25] R. Arnoux. «ITER... and then what?» In: (May 2014). URL: https://www.iter.org/mag/3/22 (cit. on p. 16).

[26] AIN.org. «DEMO: parte la progettazione ingegneristica». In: (July 2022). URL: https://www.associazioneitalianaanucleare.it/demo-parte-la-progettazione-ingegneristica/ (cit. on pp. 16, 17).

[27] wikipedia.org. *DEMOnstration Power Plant*. URL: https://en.wikipedia.org/wiki/DEMOnstration_Power_Plant (cit. on p. 16).

[28] IAEA.org. *Demonstration Fusion Plants*. URL: https://www.iaea.org/bulletin/demonstration-fusion-plants#:~:text=The%20aim%20of%20ITER%2C%20the,or%20DEMOs%2C%20will%20come%20in. (cit. on p. 17).

[29] EUROfusion.org. *DEMONSTRATION POWER PLANT DEMO*. URL: https://euro-fusion.org/programme/demo/ (cit. on p. 18).

[30] JÜLICH Forschungszentrum. *DEMO*. URL: https://www.fz-juelich.de/en/iek/iek-4/forschung/demo (cit. on p. 18).

[31] S. Zhang, Z. Wang, C. Chen, J. Jia, and Z. Chen. «Pressure wave behavior and its effects on structure under In-box LOCA in a helium-cooled lead lithium blanket of hydrogen fusion reactors». In: (Jan. 2021). DOI: https://doi.org/10.1016/j.ijhydene.2020.11.228. URL: https://www.sciencedirect.com/science/article/pii/S0360319920344797 (cit. on p. 18).

[32] M. Sprò, A. Froio, and A. Zappatore. «3D Transient CFD Simulation of an In-Vessel Loss-of-Coolant Accident in the EU DEMO WCLL Breeding Blanket». In: *Energies* (Apr. 2023). DOI: https://doi.org/10.3390/en16093637. URL: https://www.mdpi.com/1996-1073/16/9/3637 (cit. on p. 18).

[33] X.Z. Jin. «Preliminary accident analysis of ex-vessel LOCA for the European DEMO HCPB blanket concept». In: (May 2021). URL: https://scipub.euro-fusion.org/wp-content/uploads/eurofusion/WPSAECPR18_19912_submitted-4.pdf (cit. on p. 18).

[34] Z. Nannan. *Researchers Evaluate In-vessel Loss of Coolant Accident for Helium-cooled Blanket in Fusion Reactor*. URL: https://english.cas.cn/newsroom/research_news/phys/202210/t20221031_322411.shtml (cit. on p. 19).

[35] A. Froio, A. Bertinetti, S. Ciattaniglia, F. Cismondi, L. Savoldi, and R. Zanino. «Modelling an In-Vessel Loss of Coolant Accident in the EU DEMO WCLL Breeding Blanket with the GETTHEM Code». In: (Apr. 2018). DOI: https://doi.org/10.1016/j.fusengdes.2018.04.106. URL: https://www.sciencedirect.com/science/article/pii/S0920379618304009 (cit. on p. 19).

[36] M. D'Onorio, F. Giannetti, M.T. Porfiri, and G. Caruso. «Preliminary safety analysis of an in-vessel LOCA for the EU-DEMO WCLL blanket concept». In: (Feb. 2020). DOI: https://doi.org/10.1016/j.fusengdes.2020.111560. URL: https://www.sciencedirect.com/science/article/pii/S0920379620301083 (cit. on p. 19).

[37] M. Ahn, S. Cho, D.H. Kim, E. Lee, H. Kim, J. Suh, S. Yun, and N.Z. Cho. «Preliminary safety analysis of Korea Helium Cooled Solid Breeder Test Blanket Module». In: (June 2008). DOI: https://doi.org/10.1016/j.fusengdes.2008.06.059. URL: https://www.sciencedirect.com/science/article/pii/S0920379608001944 (cit. on p. 19).

[38] A. Froio, L. Barrucca, S. Ciattaniglia, F. Cismondi, L. Savoldi, and R. Zanino. «Analysis of the effects of primary heat transfer system isolation valves in case of in-vessel loss-of-coolant accidents in the EU DEMO». In: (Aug. 2020). DOI: https://doi.org/10.1016/j.fusengdes.2020.111926. URL: https://www.sciencedirect.com/science/article/pii/S0920379620304749 (cit. on p. 19).

[39] N. Nakamura, K. Tobita, Y. Someya, H. Utoh, Y. Sakamoto, and W. Gulden. «Thermohydraulic responses of a water-cooled tokamak fusion DEMO to loss-of-coolant accidents». In: (Oct. 2015). DOI: 10.1088/0029-5515/55/12/123008. URL: https://iopscience.iop.org/article/10.1088/0029-5515/55/12/123008 (cit. on p. 19).

[40] J.R. Stewart. «CFD modelling of underexpanded hydrogen jets exiting rectangular shaped openings». In: (May 2020). DOI: https://doi.org/10.1016/j.psep.2020.04.043. URL: https://www.sciencedirect.com/science/article/pii/S0957582019317276 (cit. on pp. 19, 21, 23).

[41] E. Franquet, V. Perrier, S. Gibout, and P. Bruel. «Free underexpanded jets in a quiescent medium: A review». In: (2015). DOI: https://doi.org/10.1016/j.paerosci.2015.06.006. URL: https://www.sciencedirect.com/science/article/pii/S0376042115000548 (cit. on pp. 20–22).

[42] P. Yan. «Numerical Simulation of Underexpanded Jets in the Non-ideal Flow Regime». Master thesis. Oct. 2021. URL: https://www.politesi.polimi.it/handle/10589/179177 (cit. on p. 20).

[43] A.H. Shapiro. *The Dynamics and Thermodynamics of Compressible Fluid Flows*. Vol. 1. New York: Wiley, 1953 (cit. on p. 20).

[44] R.D. Zucker and O. Biblarz. *Fundamentals of Gas Dynamics*. Wiley, 2019 (cit. on p. 20).

[45] Aerospaceweb.org. *Shock Diamonds and Mach Disks*. URL: https://aerospaceweb.org/question/propulsion/q0224.shtml (cit. on p. 21).

[46] N.Y. Bykov, Y.E. Gorbachev, and S.A. Fyodorov. «Highly underexpanded rarefied jet flows». In: (Aug. 2023). DOI: 10.3389/fmech.2023.1216927. URL: https://www.frontiersin.org/articles/10.3389/fmech.2023.1216927/full (cit. on p. 23).

[47] G.A. Bird. *Molecular Gas Dynamics and the Direct Simulation of Gas Flows*. Second. Midsomer Norton, Avon: Bookcraft (Bath) Ltd, 1995 (cit. on pp. 24–32, 34–39, 48).

[48] M. D'Onorio and G. Caruso. «Pressure suppression system influence on vacuum vessel thermal-hydraulics and on source term mobilization during a multiple First Wall – Blanket pipe break». In: (Mar. 2021). DOI: https://doi.org/10.1016/j.fusengdes.2020.112224. URL: https://iris.uniroma1.it/bitstream/11573/1481867/1/D%27Onorio_Pressure%20suppression_postprint_2021.pdf (cit. on p. 43).

[49] wikipedia.org. *SALOME*. URL: https://it.wikipedia.org/wiki/SALOME (cit. on p. 43).

[50] EURIWARE. *SALOME Platform v9.11.0*. 2023. URL: https://www.salome-platform.org/?page_id=23 (cit. on pp. 43, 66).

[51] wikipedia.org. *OpenFOAM*. URL: https://it.wikipedia.org/wiki/OpenFOAM (cit. on p. 45).

[52] The MathWorks Inc. *MATLAB version: 9.13.0 (R2022b)*. Natick, Massachusetts, United States, 2023. URL: https://www.mathworks.com (cit. on p. 48).

[53] periodictable.com. *Technical data for Helium*. URL: https://periodictable.com/Elements/002/data.html (cit. on p. 48).

[54] Z.X. Sun, Z. Tang, Y.L. He, and W.Q. Tao. «Proper cell dimension and number of particles per cell for DSMC». In: (Apr. 2011). DOI: http://dx.doi.org/10.1016/j.compfluid.2011.04.013. URL: https://www.researchgate.net/publication/251503052_Proper_Cell_Dimension_and_Number_of_Particles_Per_Cell_for_DSMC (cit. on p. 49).

[55] F. Juretić et al. *cfMesh v1.1 User Guide*. Zagreb, HR: Creative Fields, 2015. URL: https://cfmesh.com/wp-content/uploads/2015/09/User_Guide-cfMesh_v1.1.pdf (cit. on pp. 49–51, 53).

[56] M. Baburic. *cfMesh*. 71-75 Shelton Street, Covent Garden, London WC2H 9JQ, United Kingdom, 2023. URL: https://cfmesh.com/cfmesh/ (cit. on p. 49).

[57] R. Ferramosca. *PARAVIEW POTENTE SOFTWARE PROFESSIONALE PER LA VISUALIZZAZIONE SCIENTIFICA*. URL: https://www.lffl.org/2014/05/paraview-potente-software-professionale.html (cit. on p. 54).

[58] wikipedia.org. *ParaView*. URL: https://en.wikipedia.org/wiki/ParaView (cit. on p. 54).

[59] openfoamwiki.net. *MapFields*. URL: https://openfoamwiki.net/index.php/MapFields (cit. on p. 65).

[60] hpc.polito.it. *I sistemi di calcolo di HPC@POLITO*. URL: https://hpc.polito.it/sistemi_hpc.php (cit. on pp. 88, 89).